CENTER FOR CONNECTED AND AUTOMATED TRANSPORTATION

ICT-24-030
December 2024

Prediction of Pavement Damage under Truck Platoons Utilizing a Combined Finite Element and Artificial Intelligence Model

Aravind Ramakrishnan
Fangyu Liu
Angeli Jayme
Imad Al-Qadi

ILLINOIS CENTER FOR TRANSPORTATION

DISCLAIMER

Funding for this research was provided by the Center for Connected and Automated Transportation under Grant No. 69A3552348301 of the U.S. Department of Transportation, Office of the Assistant Secretary for Research and Technology (OST-R), University Transportation Centers Program. The contents of this report reflect the views of the authors, who are responsible for the facts and the accuracy of the information presented herein. This document is disseminated under the sponsorship of the Department of Transportation, University Transportation Centers Program, in the interest of information exchange. The U.S. Government assumes no liability for the contents or use thereof.

SUGGESTED APA FORMAT CITATION:

Ramakrishnan A., Liu F., Jayme A., & Al-Qadi. I.L. (2024). *Prediction of pavement damage under truck platoons utilizing a combined finite element and artificial intelligence models* (Report No. ICT-24-030). Illinois Center for Transportation. https://doi.org/10.36501/0197-9191/24-030

Contacts

For more information:

Imad L. Al-Qadi
University of Illinois at Urbana–Champaign
1207 Nathan Newmark Civil Engineering Laboratory
Urbana, IL 61801
Phone: (217) 265-0427
Email: alqadi@illinois.edu

CCAT
University of Michigan Transportation Research Institute
2901 Baxter Road
Ann Arbor, MI 48152
uumtri-ccat@umich.edu
Phone: (734) 763-2498
www.ccat.umtri.umich.edu

TECHNICAL REPORT DOCUMENTATION PAGE

1. Report No.	2. Government Accession No.	3. Recipient's Catalog No.
ICT-24-030	N/A	N/A

4. Title and Subtitle	5. Report Date
Prediction of Pavement Damage under Truck Platoons Utilizing a Combined Finite Element and Artificial Intelligence Model	December 2024
	6. Performing Organization Code N/A

7. Authors	8. Performing Organization Report No.
Aravind Ramakrishnan (https://orcid.org/0000-0003-3269-015X), Fangyu Liu (https://orcid.org/0000-0003-0844-563X), Angeli Jayme (https://orcid.org/0000-0003-3640-4317), Imad Al-Qadi (https://orcid.org/0000-0002-5824-103X)	ICT-24-030 UILU-ENG-2024-2030

9. Performing Organization Name and Address	10. Work Unit No.
Illinois Center for Transportation Department of Civil and Environmental Engineering University of Illinois Urbana-Champaign 205 North Mathews Avenue, MC-250 Urbana, IL 61801	N/A
	11. Contract or Grant No. Contract No. 69A3552348301

12. Sponsoring Agency Name and Address	13. Type of Report and Period Covered
Center for Connected and Automated Transportation University of Michigan Transportation Research Institute 2901 Baxter Road Ann Arbor, MI 48152	Final Report
	14. Sponsoring Agency Code

15. Supplementary Notes

Funding under Grant No. 69A3552348301 U.S. Department of Transportation, Office of the Assistant Secretary for Research and Technology (OST-R), University Transportation Centers Program. https://doi.org/10.36501/0197-9191/24-030

16. Abstract

For robust pavement design, accurate damage computation is essential, especially for loading scenarios such as truck platoons. Studies have developed a framework to compute pavement distresses as function of lateral position, spacing, and market-penetration level of truck platoons. The established framework uses a robust 3D pavement model, along with the AASHTOWare Mechanistic–Empirical Pavement Design Guidelines (MEPDG) transfer functions to compute pavement distresses. However, transfer functions include high variability and lack physical significance. Therefore, as an improvement to effectively predict permanent deformation, this study utilized a conventional Burger's model, incorporating a nonlinear power-law dashpot, in lieu of a transfer function. Key components, including stress increments and the Jacobian, were derived for implementation in ABAQUS as a user subroutine. Model parameters were determined through asphalt concrete (AC) flow number and dynamic modulus tests. Using a nonlinear power-law dashpot, the model accurately characterized rutting under varying conditions. The Burger's model was both verified and validated to check the accuracy of implementation and representative of the actual behavior, respectively. Initially developed in 1D domain, the validated Burger's model was integrated into the robust 3D finite element (FE) pavement model to predict permanent deformation. A new load-pass approach (LPA) enabled reduction in computational domain and cost, along with implementing transient loads more efficiently. The combined integration of the LPA and the Burger's model into the pavement model effectively captured the rutting progression per loading cycle. Moreover, a graph neural network (GNN) was established to extend the prediction power of the framework, while strategically limiting the FE numerical matrix. The FE model data was transformed into a graph structure, converting FE model components into corresponding graph nodes and edges. The GNN-based pavement simulator (GPS) was developed to model 3D pavement responses, integrating three key components: encoder, processor, and decoder. The GPS model employed two-layer multilayer perceptrons (MLP) for the encoder and decoder, while utilizing graph network (GN) technology for the processor. Validation occurred through two case studies—OneStep and Rollout—with results compared against FE model data as ground truth. Results demonstrated that the GPS model provides an accurate and computationally efficient alternative to traditional 3D pavement FE simulations.

17. Key Words	18. Distribution Statement
Rutting, Pavement Damage, Permanent Deformation, Pavement Performance Modeling, Asphalt Concrete, Burger's Model, Flow-Number Test, Connected and Autonomous Trucks, Truck Platoons, Rest Period, Load-Pass Approach, Pavement Model, Graph Neural Networks, Machine Learning.	No restrictions. This document is available through the National Technical Information Service, Springfield, VA 22161.

19. Security Classif. (of this report)	20. Security Classif. (of this page)	21. No. of Pages	22. Price
Unclassified	Unclassified	68	N/A

ACKNOWLEDGMENT, DISCLAIMER, MANUFACTURERS' NAMES

This project was conducted in cooperation with the Center for Connected and Automated Transportation and the Illinois Center for Transportation. The contents of this report reflect the view of the authors, who are responsible for the facts and the accuracy of the data presented herein. The contents do not necessarily reflect the official views or policies of CCAT or ICT. This report does not constitute a standard, specification, or regulation. Trademark or manufacturers' names appear in this report only because they are considered essential to the object of this document and do not constitute an endorsement of the product by CCAT or ICT.

EXECUTIVE SUMMARY

Quantifying pavement damage is crucial for roadway agencies aiming to develop effective maintenance and rehabilitation strategies, ultimately extending the service life of roadways. The objective of this study was to propose an innovative framework to assess pavement rutting caused by truck platoons. To achieve the set objective, the scope of the study included the development of (i) a simulation framework for repetitive loading to predict pavement rutting using mechanistic models, and (ii) an artificial intelligence (AI) model to utilize an extensive 3D finite element (FE) pavement-response database for predicting pavement responses under cyclic loading.

To model the permanent deformation of asphalt concrete (AC), a generalized nonlinear Burger's model was implemented. This model was integrated into an existing robust 3D FE pavement framework to predict AC rutting. A nonlinear power-law dashpot was employed to effectively characterize the deformation behavior. The model was numerically formulated using an incremental approach, allowing for the determination of material responses under various loading and boundary conditions. The Burger's model was successfully implemented in the commercial FE software ABAQUS and successfully validated with analytical solutions for a simple creep-loading scenario. The model parameters were derived from the results of repeated-load permanent deformation (RLPD) and dynamic modulus tests.

Moreover, to implement cyclic loading that induces accumulative permanent deformation, a load-pass approach (LPA) was developed in the pavement FE model. In lieu of the conventional moving-load approach that requires an extensive wheel path length, which has domain implications in the other two orthogonal directions, the LPA allows for cyclic loading/multi-axle passes without necessitating an infeasible model length and run time. The LPA implements a partial entrance, moving load of a full contact-imprint, partial exit, and full rest period. This novel approach emulates a viewing window as a truck-tire load passes, accounting for a transient moving load and a reduction of the geometric domain of the model, without adversely affecting accuracy. The rest period could be initiated after the load "leaves" the point of interest, which is held at mid-length of the model. Given the reduced wheel path length, no additional load steps are appended to account for the residual rest period. After the total rest period is completed, the next axle load is immediately introduced via partial entrance until the number of desired cycles is achieved. This process was applied, and a total of 24 cases were executed using the LPA with the Burger's model. An additional 12 cases, utilizing a conventional linear viscoelastic model, were conducted for comparison purposes. The rut-distribution trend was similar for all the cases irrespective of the inputs, illustrating the importance of the wheel path location. The results demonstrated that the proposed framework (i.e., integration of the Burger's model and the LPA) effectively captured rutting progression.

Last, a graph neural network (GNN) was established to extend the prediction power of the framework, while strategically limiting the FE numerical matrix. A GNN framework is proposed to model 3D AC-pavement responses. The FE model data was transformed into a graph structure, where the nodes and connections from the FE model were converted into corresponding graph nodes and edges. Node features encompassed node coordinates, pavement-layer type, temperature, material properties, 3D loading profiles, loading time, and previous pavement responses (displacement, stress,

and strain). Edge features utilized relative distance and relative pavement responses, while output features represented target pavement responses. The GNN-based pavement simulator (GPS) was developed to model 3D pavement responses, including three main components: encoder, processor, and decoder. The GPS model utilized two-layer multilayer perceptrons (MLP) for the encoder and decoder, while employing the graph network (GN) technology for the processor phase. The model was verified via two distinct case studies—OneStep and Rollout schemes—by comparing to FE model data as ground truth, with the latter closely approximating FE simulation conditions. Performance analyses revealed satisfactory accuracy between both scenarios; however, the Rollout case demonstrated higher errors, as compared to the OneStep case. The results indicated the GPS model offered an accurate, computationally efficient alternative to minimize the need for an extensive 3D pavement FE simulation matrix.

TABLE OF CONTENTS

LIST OF FIGURES

LIST OF TABLES

CHAPTER 1: INTRODUCTION

BACKGROUND

Platoon configuration could be defined using three parameters, namely, lateral position of trucks, spacing, and number of trucks. The primary factors that might influence the development of rut-depth and fatigue-distress accumulation include the reduced interval between truck passes and the absence of lateral movement between these trucks (Gungor and Al-Qadi 2022). Quantifying pavement damage due to platoons is of key interest to roadway agencies for developing maintenance and rehabilitation strategies and achieving pavement designed service life. Hence, a framework that could compute pavement distresses as a function of those parameters is essential. Okte and Al-Qadi (2022a) introduced a framework, known as the Expected Response Framework, to determine distress; it considered effect of wander and platoon-penetration level.

The framework was further modified to incorporate rest period (truck spacing) into pavement-distress calculations (Ramakrishnan et al. 2021). The effect of the rest period was incorporated using experimental results (Alrajhi et al. 2022), where repeated-load, permanent-deformation tests for various asphalt concrete (AC) parameters were considered. The experimental program included various binders, temperatures, loading levels, and rest periods. The permanent deformation was consistently observed to be greater with an increased rest period, irrespective of other testing parameters. Hence, special attention was needed to investigate counterintuitive results of the permanent-deformation tests.

In the framework, responses from the 3D finite element (FE) pavement model, coupled with AASHTO Mechanistic–Empirical Pavement Design Guide (MEPDG) transfer functions, were used to compute the distresses. However, transfer functions were deemed to be unreliable for two main reasons: variability associated with calibration factors (empirical) and lack of physical significance. Despite high accuracy of 3D FE pavement models, they are often computationally intensive, thus highlighting a need for a framework to compute pavement distresses accurately and efficiently in lieu of transfer functions.

Additionally, despite the 3D pavement model's robustness, the higher computational requirement and longer time make it impractical for road agencies to use the model for pavement design. Therefore, with recent advancements in artificial intelligence (AI), a solution for predicting pavement responses instantly is possible. Machine learning (ML) is an AI field devoted to comprehending and developing "learning" methods or methods that use data to enhance performance on a certain set of tasks (Mitchell 1997). Significant work has been performed on applying AI methods, especially ML, in civil engineering, including material-property prediction (Liu et al. 2020, 2021), material mix-design optimization (Liu et al. 2022b; Rivera-Pérez and Al-Qadi 2024), structural-strength prediction (Taghipour Anvari et al. 2023; Zhou et al. 2017), infrastructure-response modeling (Liu et al. 2023; Okte and Al-Qadi 2022b; Ye et al. 2022), infrastructure-damage detection (Liu et al. 2022a, 2024b, 2024a), seismic-damage assessment (Zhai et al. 2024), infrastructure-condition assessment (Majidifard et al. 2020; Zhu et al. 2021), structural-design optimization (Zhao et al. 2023b, 2023a), and construction-site management (Angah and Chen 2020; Chen et al. 2020).

Given the reported accuracy and efficiency, ML applications have increased in civil engineering, especially to predict infrastructure responses. For example, Ye et al. (2022) developed an FE based ML framework to predict structural fire responses, which combined the accuracy of FE methods and the efficiency of ML techniques to achieve real-time infrastructure-response prediction. Okte and Al-Qadi (2022b) applied artificial neural networks (ANN) to predict critical pavement responses based on a database of 850 3D pavement FE cases. The researchers used the Monte Carlo dropout approach to quantify model uncertainty. Similarly, Liu et al. (2023) and Zhou and Al-Qadi (2024) proposed a physics-informed long short-term memory (LSTM) network for structural-response modeling by incorporating physics constraints into LSTM models. They built an FE database for seismic responses to train models. The applications of ML in civil engineering suggest its high potential for predicting 3D pavement responses.

RESEARCH OBJECTIVE AND SCOPE

The objective of this study was to propose an innovative framework to assess pavement rutting induced by truck platoons. To achieve the set objective, the scope of the study included the following: (i) develop a simulation framework for repetitive loading to predict pavement responses, including rutting, utilizing mechanistic models; and (ii) develop a graph neural network to utilize an extensive 3D finite element (FE) pavement-response database for predicting pavement responses. The scope is further explained as follows:

i. Numerical simulation of repetitive loading on flexible pavement under truck platoons. This task comprised two subtasks: development of a mechanistic pavement-damage model to predict rut depth and implementation of the load-pass approach to invoke repetitive loading. This framework allowed simulation of repetitive loading and predict accumulating pavement responses, including rutting, using a mechanistic model.

ii. Graph neural network (GNN) development for predicting pavement responses. An expansive 3D pavement FE response database was generated utilizing the established 3D pavement FE model. The proposed GNN enabled rapid prediction of pavement responses, using the extensive 3D pavement FE response database, while strategically limiting the necessary FE simulations.

CHAPTER 2: PERMANENT-DEFORMATION MODEL

INTRODUCTION

Flexible-pavement permanent deformation, also known as rutting, is a serious distress in AC pavements. Rutting contributes to road roughness, risk of hydroplaning, and hazardous driving conditions. Rutting could result from external loads, tire pressure, the intrinsic behavior of the AC materials and supporting layers, and environmental influences. Rutting in flexible pavement is typically due to viscoplastic-strain accumulation in AC, which is caused by material densification and shear flow under higher temperatures and loads (Huang 2004; Mallick and El-Korchi 2022); settlements or compaction in the unbound granular layer (Ahmed and Erlingsson 2013; Deacon et al. 2002); and abrasion from studded tires (Lundberg et al. 2021). As presented in Figure 1 (Alamnie et al. 2022), the progression of permanent deformation in AC could be divided into three stages: densification (where deformation increased at a decreasing rate), strain hardening (where deformation increased at a steady rate), and flow (where deformation increased at an accelerating rate) (Zhou et al. 2004; Zhou and Scullion 2002). Traditionally, this behavior has been assessed through a triaxial creep-recovery test.

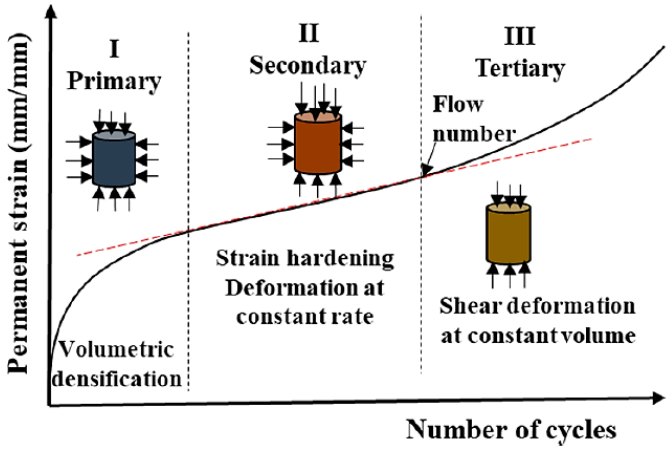

Figure 1. Illustration. Three stages of AC permanent deformation.

Source: Alamnie et al., 2022

When strains in AC are below 100 to 125με, the material behavior is deemed to be within the linear viscoelastic range without inducing any permanent deformation (Airey et al. 2003b; a). However, when AC has been subjected to loading and unloading, the resulting strain would consist of four components: elastic, plastic, viscoelastic, and viscoplastic. Elastic strain accounts for the fully recovered portion as soon as the load has been removed. Plastic strain, which occurs immediately upon load application, is permanent and cannot be recovered. In contrast, viscoelastic strain is recoverable, while viscoplastic strain is not, with both being time-dependent. Permanent strain, such as normalized rutting, is the cumulative effect of plastic, viscoelastic, and viscoplastic strains. Therefore, permanent strain includes two time-dependent components that are influenced by the loading duration and the rest period (Figure 2).

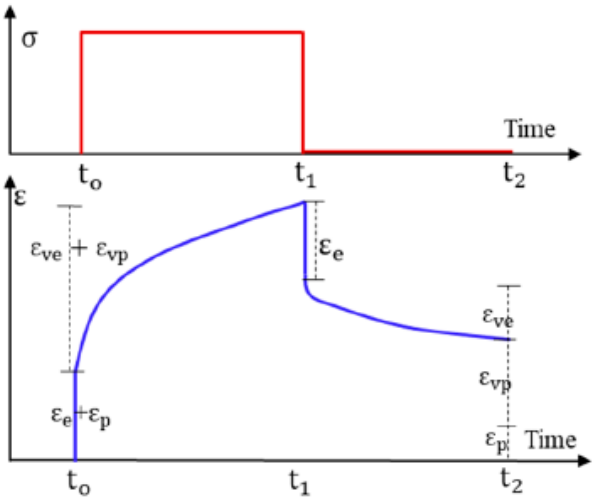

Figure 2. Illustration. Conventional creep-recovery strain components.

Source: Alamnie et al., 2022

Permanent deformation of AC could be modeled in various ways. Typically, analytical models have been employed for pavement design, either as mechanistic–empirical or empirical models, and calibrated using laboratory experiments and/or field-test data. The most widely used model is the rutting-transfer equation from AASHTOWare Mechanistic–Empirical Pavement Design (MEPD), which has only accounted for the primary (that occurred in unbound materials) and secondary (that occurred in AC) stages of rutting (i.e., considered volumetric changes only). To calculate AC rutting, the pavement layers were divided into sublayers; and vertical compressive strain was measured at the mid-depth of each sublayer. The main limitation of this analytical model has been the reliance on regression equations, calibrated with experimental or field data. Hence, its application is valid only within the scope of the data.

Use of mechanical analogs has been another method for modeling AC behavior. For example, linear viscoelastic behavior has been described via mechanical analogs using springs and dashpots, which represent elastic and viscous behaviors, respectively. Analog models have been also extensively used to characterize large deformations in polymers (Khan et al. 2006). The Prony series (a generalized Maxwell model in parallel with a spring) has been primarily used to characterize the linear viscoelastic behavior of AC. Various combinations of springs, dashpots, sliders (slip devices), and parabolic elements have been used to model the viscoelastic behavior of the material (Benedetto et al. 2007; Collop et al. 2003; Grzesikiewicz et al. 2013; Olard and Di Benedetto 2003; Zbiciak 2013). The advantage of analog models lies in their ability to visualize stresses and strains within the elements. Based on the arrangement of the model, a constitutive model could be derived analytically (through governing differential equations), making numerical implementation easier and thus providing an efficient method for material characterization.

In the literature, modified versions of the conventional Burger's model (a combination of the Maxwell and Kelvin–Voigt [KV] models in series) have been used frequently to simulate the viscoelastic–viscoplastic behavior of AC (Collop et al. 2003; Grzesikiewicz et al. 2013; Zbiciak 2013). Constitutive

relations for these models have been established and implemented numerically. Based on analog models, viscoelastic integrals could be defined for mechanisms such as permanent deformation and hardening–relaxation (Cao and Kim 2016; Subramanian et al. 2013). However, the complexity of current models in terms of numerical implementation and the need for extensive experimental data to obtain material parameters present significant challenges for real-life application. Therefore, this study proposes a new viscoelastic fluid model to characterize AC permanent-deformation behavior.

Detailed derivation and implementation of the nonlinear Burger's model is presented in the following section. The model enables characterization of AC rutting, with the model input parameters obtained from experimental results. It is worth noting that the model's prediction and scope were limited up to the secondary stage of permanent deformation. The following steps were followed:

- Permanent deformation was modeled using a nonlinear dashpot. The model was derived numerically and implemented in the commercial FE software ABAQUS.
- An analytical solution for a simple loading case was used to verify the Burger's model.
- Dynamic modulus and flow-number test results were utilized to obtain model parameters.
- A subset of experimental results was used to constitute the model parameters, which were then validated by predicting other scenarios from the tests (differing from the training subset).

GENERALIZED BURGER'S MODEL

The generalized Burger's model (GBM) comprised a spring, a dashpot, and several KV elements (spring and dashpot connected in parallel) connected in series, as presented in Figure 3.

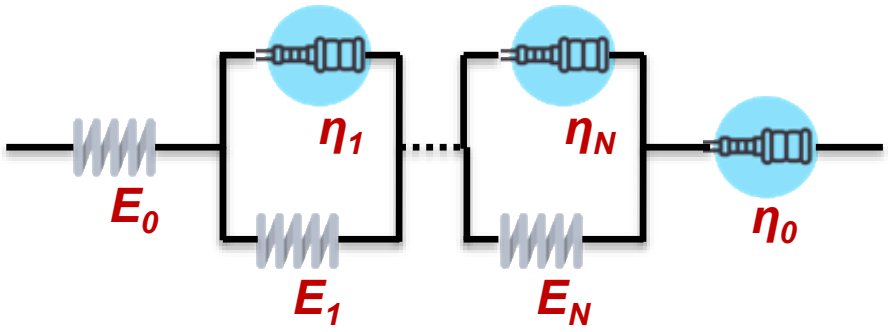

Figure 3. Illustration. Generalized Burger's model.

In the GBM model, the stiffness of a spring element (E_0), KV elements ($E_i, \eta_i\ i = 1,2,..N$), and viscosity of a dashpot element (η_0) simulated the elastic, viscoelastic, and permanent-deformation behavior of AC, respectively. For a given applied stress, the total strain in the model was the summation of individual strains of the elements in the model, where stress remained constant across each element. Mathematically, the total strain could be formulated as presented in Figure 4.

$$\epsilon(t) = \epsilon_e(t) + \sum_{i=1}^{N} \epsilon_{ve}^{i}(t) + \epsilon_p(t)$$

Figure 4. Equation. Total strain is the summation of elastic, viscoelastic, and plastic strain.

where $\epsilon(t)$ is total strain in the GBM model, $\epsilon_e(t)$ is elastic strain in the spring element, $\epsilon_{ve}^{i}(t)$ is viscoelastic strain in the i^{th} KV element, and $\epsilon_p(t)$ is irrecoverable strain in the dashpot element.

Elastic Strain

The spring element represented Hooke's law (i.e., stress is proportional to strain and the proportionality constant is the modulus). Mathematically, it could be expressed as presented in Figure 5.

$$\sigma(t) = E_0 \epsilon_e(t)$$

Figure 5. Equation. Constitutive equation of simple spring element.

Viscoelastic Strain

Linear viscoelastic behavior was represented via KV elements. Material parameters such as creep compliance and relaxation moduli have been commonly used to characterize this behavior. Creep compliance refers to the strain in the model under a constant unit stress, and the relaxation modulus refers to the stress in the model under a constant unit strain. In series models (i.e., model with elements connected in series) like the GBM, creep compliance is easily determined because strains are additive. In contrast, in parallel models like the generalized Maxwell model, the relaxation modulus is easily determined because stresses are additive. The creep compliance of KV elements is presented in Figure 6.

$$D(t) = \left[\sum_{i=1}^{N} \frac{1}{E_i}\left(1 - e^{-\frac{t}{\tau_i}}\right)\right]$$

Figure 6. Equation. Creep compliance for Kelvin-Voight elements.

where $D(t)$ is creep compliance, and $\tau_i = \frac{\eta_i}{E_i}$ is retardation time of i^{th} KV element.

For a linear viscoelastic material, if creep compliance is known, then the relaxation modulus could be obtained easily, and vice versa, using the following relationship presented in Figure 7.

$$t = \int_{-0}^{t} D(t-\tau)R(\tau)d\tau$$

Figure 7. Equation. Relationship between creep compliance and relaxation modulus.

where $R(t)$ is relaxation modulus.

Park and Kim (1999) numerically implemented Figure 7 to obtain the relaxation modulus from creep compliance, and vice versa. If material parameters of the relaxation modulus were known, then creep-compliance coefficients could be obtained by solving the equation in Figure 7 (Park and Schapery 1999). For linear viscoelastic material, stresses and strains have been related using either creep compliance or relaxation modulus, as formulated in Figure 8 and Figure 9, respectively.

$$\epsilon_{ve}(t) = \int_{-0}^{t} D(t-\tau)\dot{\sigma}(\tau)d\tau$$

Figure 8. Equation. Constitutive relation of linear viscoelastic material using creep compliance.

$$\sigma(t) = \int_{-0}^{t} R(t-\tau)\dot{\epsilon_{ve}}(\tau)d\tau$$

Figure 9. Equation. Constitutive relation of linear viscoelastic material using relaxation modulus.

Permanent Strain

For the dashpot element, the stresses are proportional to the strain rate and correlated through the viscosity of dashpot (η_0) (Figure 10).

$$\sigma(t) = \eta_0 \dot{\epsilon_p}(t)$$

Figure 10. Equation. Constitutive relation for a dashpot.

Figure 10 can also be written as presented in Figure 11.

$$\epsilon_p(t) = \int_{-0}^{t} \frac{\sigma(\tau)}{\eta(\tau)} d\tau$$

Figure 11. Equation. Plastic strain is a function of stress and viscosity of the dashpot.

The strain in the dashpot is irrecoverable, resulting in permanent deformation. The viscosity of the dashpot can be expressed as a function of time, stress, and temperature; or it can be considered a constant. If the viscosity is constant, then permanent strain will be linear, as a function of time for creep loading.

If $\eta(\tau) = \eta_0\ (constant)$ and $\sigma(\tau) = \sigma_0$, then Figure 11 can be solved as presented in Figure 12.

$$\epsilon_p(t) = \int_{-0}^{t} \frac{\sigma_0}{\eta_0} d\tau = \frac{\sigma_0 t}{\eta_0}$$

Figure 12. Equation. Integral function solved for plastic strain.

However, AC permanent deformation under creep loading is nonlinear (Figure 1). Hence, a dashpot of constant viscosity is inadequate to capture such behavior. Several studies have used a nonlinear

dashpot to capture the permanent deformation behavior of AC and polymers (Khan et al. 2006; Kucuk et al. 2013; Liang and Guan 2022; Pei et al. 2016; Zhang et al. 2016). In this study, the viscosity of the dashpot was characterized as follows (Figure 13):

$$\eta_0(t) = at^b$$

Figure 13. Equation. Nonlinear dashpot.

where a, b are material constants, and t is the time. The permanent deformation for creep loading is calculated via Figure 14.

$$\epsilon_p(t) = \int_{-0}^{t} \frac{\sigma_0}{at^b} d\tau = \frac{\sigma_0 t^{1-b}}{a(1-b)}$$

Figure 14. Equation. Permanent deformation for creep loading.

If $b < 1$, then permanent deformation would be similar to the actual behavior of AC.

NUMERICAL IMPLEMENTATION

The incremental formulation of the model was derived to obtain strains for any arbitrary loading. This formulation computed the change in strains for a small load increment. The formulation was particularly useful for writing the user material subroutine (UMAT) in ABAQUS (i.e., custom material constitutive relation), where it was used to characterize rutting in the AC. The incremental strain in the model at $(n+1)^{th}$ increment is presented in Figure 15.

$$\Delta\epsilon(t_{n+1}) = \Delta\epsilon_e(t_{n+1}) + \sum_{i=1}^{N} \Delta\epsilon_{ve}^{i}(t_{n+1}) + \Delta\epsilon_p(t_{n+1})$$

Figure 15. Equation. Incremental total strain is the summation of incremental elastic, viscoelastic, and plastic strains.

where $\Delta\epsilon(t_{n+1}) = \epsilon(t_{n+1}) - \epsilon(t_n)$, and $t_{n+1} = t_n + \Delta t$, Δt is the time increment.

Spring Element (Elastic Strain)

Incremental strain in the spring element could be derived as presented in Figure 16.

$$\Delta\sigma(t_{n+1}) = E_0 \Delta\epsilon_e(t_{n+1})$$

Figure 16. Equation. Incremental stress is related to incremental elastic strain for a simple spring.

Figure 16 could be rearranged as presented in Figure 17.

$$\Delta\epsilon_e(t_{n+1}) = \epsilon_e(t_{n+1}) - \epsilon_e(t_n) = \frac{\Delta\sigma}{E_0}$$

Figure 17. Equation. Rearranged form of Figure 16.

KV Elements (Viscoelastic Strain)

The viscoelastic strains are presented in Figure 18.

$$\epsilon_{ve}(t_{n+1}) = \int_{-0}^{t_{n+1}} \left[\sum_{i=1}^{N} \frac{1}{E_i}\left(1 - e^{-\frac{(t_{n+1}-\tau)}{\tau_i}}\right)\right] \dot{\sigma}(\tau)d\tau$$

Figure 18. Equation. Viscoelastic strain at $(n+1)^{th}$ time step.

The above integral could be separated as presented in Figure 19.

$$\epsilon_{ve}(t_{n+1}) = \int_{-0}^{t_{n+1}} \left[\sum_{i=1}^{N} \frac{1}{E_i}\right] \dot{\sigma}(\tau)d\tau \; - \int_{-0}^{t_{n+1}} \left[\sum_{i=1}^{N} \frac{e^{-\frac{(t_{n+1}-\tau)}{\tau_i}}}{E_i}\right] \dot{\sigma}(\tau)d\tau$$

Figure 19. Equation. Separation of Figure 18.

The first part of the Figure 19 could be solved as presented in Figure 20.

$$\int_{-0}^{t_{n+1}} \left[\sum_{i=1}^{N} \frac{1}{E_i}\right] \dot{\sigma}(\tau)d\tau = \left[\sum_{i=1}^{N} \frac{1}{E_i}\right] \sigma(t_{n+1})$$

Figure 20. Equation. Solved first part of Figure 19.

The second part of Figure 19 ($\theta_i(t_{n+1})$) could be further split, as presented in Figure 21.

$$\theta_i(t_{n+1}) = \int_{-0}^{t_{n+1}} \frac{e^{-\frac{(t_{n+1}-\tau)}{\tau_i}}}{E_i} \dot{\sigma}(\tau)d\tau = \int_{-0}^{t_n} \frac{e^{-\frac{(t_{n+1}-\tau)}{\tau_i}}}{E_i} \dot{\sigma}(\tau)d\tau + \int_{t_n}^{t_{n+1}} \frac{e^{-\frac{(t_{n+1}-\tau)}{\tau_i}}}{E_i} \dot{\sigma}(\tau)d\tau$$

Figure 21. Equation. Second part of Figure 19.

In Figure 21, the first part t_{n+1} could be substituted as $t_n + \Delta t$; and the equation becomes Figure 22.

$$\int_{-0}^{t_n} \frac{e^{-\frac{(t_{n+1}-\tau)}{\tau_i}}}{E_i} \dot{\sigma}(\tau)d\tau = \int_{-0}^{t_n} \frac{e^{-\frac{(t_n+\Delta t-\tau)}{\tau_i}}}{E_i} \dot{\sigma}(\tau)d\tau = \theta_i(t_n)e^{-\frac{\Delta t}{\tau_i}}$$

Figure 22. Equation. t_{n+1} was substituted as $t_n + \Delta t$ in Figure 21.

where

$$\theta_i(t_n) = \int_{-0}^{t_n} \frac{e^{-\frac{(t_n-\tau)}{\tau_i}}}{E_i} \dot{\sigma}(\tau) d\tau$$

Figure 23. Equation. $\boldsymbol{\theta_i(t_n)}$

In the second part of the Figure 21, the stress derivative could be approximated as $\dot{\sigma}(\tau) = \frac{\Delta\sigma}{\Delta\tau} = \frac{\sigma(t_{n+1})-\sigma(t_n)}{t_{n+1}-t_n}$. It is noteworthy that the provided approximation is valid for small time increments, when the stress in the time interval is linear. The equation could be rewritten as presented in Figure 24.

$$\int_{t_n}^{t_{n+1}} \frac{e^{-\frac{(t_{n+1}-\tau)}{\tau_i}}}{E_i} \dot{\sigma}(\tau) d\tau = \int_{t_n}^{t_{n+1}} \frac{e^{-\frac{(t_{n+1}-\tau)}{\tau_i}}}{E_i} \left(\frac{\Delta\sigma}{\Delta\tau}\right) d\tau$$

Figure 24. Equation. Approximate form of the second part of Figure 21.

Figure 24 could be solved directly, as presented in Figure 25.

$$\int_{t_n}^{t_{n+1}} \frac{e^{-\frac{(t_{n+1}-\tau)}{\tau_i}}}{E_i} \dot{\sigma}(\tau) d\tau = \frac{\Delta\sigma}{\Delta\tau} \frac{\tau_i}{E_i} \left(1 - e^{-\frac{\Delta t}{\tau_i}}\right)$$

Figure 25. Equation. Solved equation (Figure 24).

Therefore, Figure 21 becomes Figure 26.

$$\theta_i(t_{n+1}) = \theta_i(t_n) e^{-\frac{\Delta t}{\tau_i}} + \frac{\Delta\sigma}{\Delta\tau} \frac{\tau_i}{E_i} \left(1 - e^{-\frac{\Delta t}{\tau_i}}\right)$$

Figure 26. Equation. $\boldsymbol{\theta_i(t_{n+1})}$.

At every time increment, $\theta_i(t_n)$ needs to be stored to obtain $\theta_i(t_{n+1})$. The incremental viscoelastic strain is presented in Figure 27.

$$\Delta\epsilon_{ve}(t_{n+1}) = \sum_{i=1}^{N} \left[\frac{\Delta\sigma}{E_i}\left(1 - \frac{\tau_i}{\Delta\tau}\left(1 - e^{-\frac{\Delta t}{\tau_i}}\right)\right) + \theta_i(t_n)\left(1 - e^{-\frac{\Delta t}{\tau_i}}\right)\right]$$

Figure 27. Equation. Incremental viscoelastic strain ($\boldsymbol{\Delta\epsilon_{ve}(t_{n+1})}$).

Dashpot Element (Permanent Strain)

Similar to the treatment of Figure 21, Figure 11 could be written as presented in Figure 28.

$$\epsilon_p(t_{n+1}) = \int_{-0}^{t_{n+1}} \frac{\sigma(\tau)}{\eta_0(\tau)} d\tau = \int_{-0}^{t_n} \frac{\sigma(\tau)}{\eta_0(\tau)} d\tau + \int_{t_n}^{t_{n+1}} \frac{\sigma(\tau)}{\eta_0(\tau)} d\tau$$

Figure 28. Equation. $\epsilon_p(t_{n+1})$.

Figure 28 could be simplified as Figure 29.

$$\epsilon_p(t_{n+1}) = \epsilon_p(t_n) + \int_{t_n}^{t_{n+1}} \frac{\sigma(\tau)}{\eta_0(\tau)} d\tau$$

Figure 29. Equation. Simplified form of Figure 28.

In Figure 28, the $\int_{t_n}^{t_{n+1}} \frac{\sigma(\tau)}{\eta_0(\tau)} d\tau$ expression could be approximated as shown in Figure 30.

$$\int_{t_n}^{t_{n+1}} \frac{\sigma(\tau)}{\eta_0(\tau)} d\tau \approx \frac{\sigma\left(t_n + \frac{\Delta t}{2}\right)}{\eta_0\left(t_n + \frac{\Delta t}{2}\right)} \Delta t = \frac{\left(\sigma(t_n) + \frac{\Delta\sigma}{2}\right)\Delta t}{a\left(t_n + \frac{\Delta t}{2}\right)^b}$$

Figure 30. Equation. Approximation of $\int_{t_n}^{t_{n+1}} \frac{\sigma(\tau)}{\eta_0(\tau)} d\tau$.

This approximation is illustrated in Figure 31.

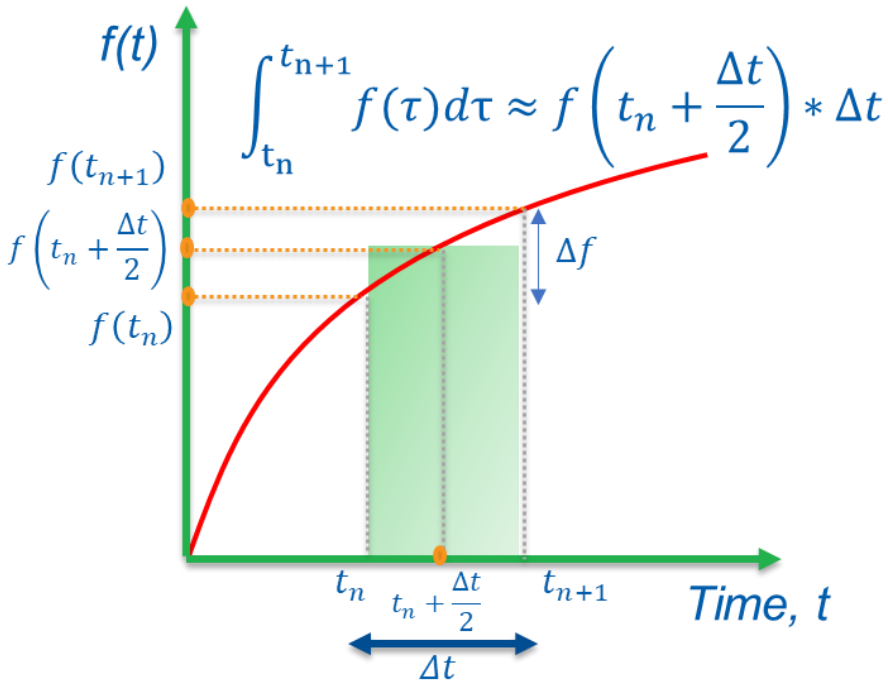

Figure 31. Illustration. Numerical approximation of an integral for a small interval.

Therefore, $\Delta\epsilon_p(t_{n+1})$ may be written as presented in Figure 32.

$$\Delta\epsilon_p(t_{n+1}) = \frac{\left(\sigma(t_n) + \frac{\Delta\sigma}{2}\right)\Delta t}{a\left(t_n + \frac{\Delta t}{2}\right)^b}$$

Figure 32. Equation. $\Delta\epsilon_p(t_{n+1})$.

The total increment strain becomes as presented in Figure 33.

$$\Delta\epsilon(t_{n+1}) = \frac{\Delta\sigma}{E_0} + \sum_{i=1}^{N}\left[\frac{\Delta\sigma}{E_i}\left(1 - \frac{\tau_i}{\Delta\tau}\left(1 - e^{-\frac{\Delta t}{\tau_i}}\right)\right) + \theta_i(t_n)\left(1 - e^{-\frac{\Delta t}{\tau_i}}\right)\right] + \frac{\left(\sigma(t_n) + \frac{\Delta\sigma}{2}\right)\Delta t}{a\left(t_n + \frac{\Delta t}{2}\right)^b}$$

Figure 33. Equation. $\Delta\epsilon(t_{n+1})$.

The ABAQUS software requires stress increments and the Jacobian to perform equilibrium iterations. Rearranging Figure 33 in terms of $\Delta\sigma$ gives Figure 34.

$$\Delta\sigma = \frac{\left(\Delta\epsilon - \sum_{i=1}^{N}\theta_i(t_n)\left(1 - e^{-\frac{\Delta t}{\tau_i}}\right) - \frac{\sigma(t_n)\Delta t}{a\left(t_n + \frac{\Delta t}{2}\right)^b}\right)}{\left[\frac{1}{E_0} + \sum_{i=1}^{N}\frac{1}{E_i}\left(1 - \frac{\tau_i}{\Delta\tau}\left(1 - e^{-\frac{\Delta t}{\tau_i}}\right)\right) + \frac{\Delta t}{2a\left(t_n + \frac{\Delta t}{2}\right)^b}\right]}$$

Figure 34. Equation. $\Delta\sigma$.

Mathematically, the Jacobian could be defined as the slope of stress increment over strain increment. Intuitively, it represents the change in stress state for a small change in strain increments.

$$J = \frac{\partial\Delta\sigma}{\partial\Delta\epsilon}$$

Figure 35. Equation. Jacobian.

Figure 35 could be differentiated with respect to the strain (Figure 36).

$$J = \frac{1}{\left[\frac{1}{E_0} + \sum_{i=1}^{N}\frac{1}{E_i}\left(1 - \frac{\tau_i}{\Delta\tau}\left(1 - e^{-\frac{\Delta t}{\tau_i}}\right)\right) + \frac{\Delta t}{2a\left(t_n + \frac{\Delta t}{2}\right)^b}\right]}$$

Figure 36. Equation. Jacobian of the Burger's model.

3D Formulation

Following the previous derivations, it is worth noting that the formulation shown in the previous section is only applicable for unidimensional problems (1D). Hence, a 3D formulation is required for appropriately modeling real-life complexities in pavements. For homogenous linear isotropic elastic material, Figure 5 could be reformulated in 3D as follows (Figure 37, Figure 38, Figure 39, and Figure 40).

$$\{\sigma(t)\} = [\mathbb{C}_e]\{\epsilon_e(t)\}$$

Figure 37. Equation. 3D constitutive relation for homogeneous linear isotropic elastic material.

where

$$[\mathbb{C}_e] = \frac{E_0}{(1+\nu)(1-2\nu)}\begin{bmatrix} 1-\nu & \nu & \nu & 0 & 0 & 0 \\ \nu & 1-\nu & \nu & 0 & 0 & 0 \\ \nu & \nu & 1-\nu & 0 & 0 & 0 \\ 0 & 0 & 0 & \frac{1-2\nu}{2} & 0 & 0 \\ 0 & 0 & 0 & 0 & \frac{1-2\nu}{2} & 0 \\ 0 & 0 & 0 & 0 & 0 & \frac{1-2\nu}{2} \end{bmatrix}$$

Figure 38. Equation.$[\mathbb{C}_e]$.

$$\{\sigma\} = \{\sigma_{11}, \sigma_{22}, \sigma_{33}, \sigma_{12}, \sigma_{13}, \sigma_{23}\}$$

Figure 39. Equation. Stress tensor in Voigt notation.

$$\{\epsilon\} = \{\epsilon_{11}, \epsilon_{22}, \epsilon_{33}, 2\epsilon_{12}, 2\epsilon_{13}, 2\epsilon_{23}\}$$

Figure 40. Equation. Strain tensor in Voigt notation.

where ν is Poisson's Ratio. Figure 37 can be rewritten as presented in Figure 41 along with Figure 42.

$$\{\epsilon_e(t)\} = [\mathbb{C}_e]^{-1}\{\sigma(t)\} = [\mathbb{R}_e]\{\sigma(t)\}$$

Figure 41. Equation. $\{\boldsymbol{\epsilon_e(t)}\}$

where

$$[\mathbb{R}_e] = \frac{1}{E_0}\begin{bmatrix} 1 & -\nu & -\nu & 0 & 0 & 0 \\ -\nu & 1 & -\nu & 0 & 0 & 0 \\ -\nu & -\nu & 1 & 0 & 0 & 0 \\ 0 & 0 & 0 & 2(1+\nu) & 0 & 0 \\ 0 & 0 & 0 & 0 & 2(1+\nu) & 0 \\ 0 & 0 & 0 & 0 & 0 & 2(1+\nu) \end{bmatrix}$$

Figure 42. Equation. $[\mathbb{R}_e]$.

For viscoelastic and dashpot elements, matrices $[\mathbb{C}]$, and $[\mathbb{R}]$ would be the same, except E_0 would be substituted with E_i, and η_0, respectively. Hence, Figure 34 and Figure 36 would become Figure 43 and Figure 44 along with Figure 45, respectively.

$$\{\Delta\sigma\} = \frac{\left([\mathbb{C}]\{\Delta\epsilon\} - \sum_{i=1}^{N}[\mathbb{C}]\{\theta_i(t_n)\}\left(1 - e^{-\frac{\Delta t}{\tau_i}}\right) - \frac{\{\sigma(t_n)\}\Delta t}{a\left(t_n + \frac{\Delta t}{2}\right)^b}\right)}{\left[\frac{1}{E_0} + \sum_{i=1}^{N}\frac{1}{E_i}\left(1 - \frac{\tau_i}{\Delta\tau}\left(1 - e^{-\frac{\Delta t}{\tau_i}}\right)\right) + \frac{\Delta t}{2a\left(t_n + \frac{\Delta t}{2}\right)^b}\right]}$$

Figure 43. Equation. $\{\boldsymbol{\Delta\sigma}\}$.

$$[J] = \frac{[\mathbb{C}]}{\left[\frac{1}{E_0} + \sum_{i=1}^{N}\frac{1}{E_i}\left(1 - \frac{\tau_i}{\Delta\tau}\left(1 - e^{-\frac{\Delta t}{\tau_i}}\right)\right) + \frac{\Delta t}{2a\left(t_n + \frac{\Delta t}{2}\right)^b}\right]}$$

Figure 44. Equation. $[\boldsymbol{J}]$**.**

where

$$[\mathbb{C}] = \frac{[\mathbb{C}_e]}{E_0}$$

Figure 45. Equation. $[\mathbb{C}]$**.**

Viscoelastic strain ($\Delta\epsilon_{ve}(t_{n+1})$) update (Figure 27) would become Figure 46 along with Figure 47.

$$\{\Delta\epsilon_{ve}(t_{n+1})\} = \sum_{i=1}^{N}\left[\frac{[\mathbb{R}]\{\Delta\sigma\}}{E_i}\left(1 - \frac{\tau_i}{\Delta\tau}\left(1 - e^{-\frac{\Delta t}{\tau_i}}\right)\right) + \{\theta_i(t_n)\}\left(1 - e^{-\frac{\Delta t}{\tau_i}}\right)\right]$$

Figure 46. Equation. $\{\boldsymbol{\Delta\epsilon_{ve}(t_{n+1})}\}$**.**

where,

$$[\mathbb{R}] = E_0[\mathbb{R}_e]$$

Figure 47. Equation. $[\mathbb{R}]$**.**

Finally, Figure 43, Figure 44, and Figure 46 could be implemented within the ABAQUS UMAT subroutine to characterize the permanent deformation of AC.

MODEL VERIFICATION

Any models, especially newly formulated ones, must undergo proper verification and validation, to ensure that the formulation has been implemented correctly in a code or subroutine. In numerical simulations, verification involves checking the implementation for errors by comparing it with an analytical solution of a well-established conceptual problem. For this case, the conceptual problem involved computing the strain of the model subjected to uniaxial constant pulse loading (Figure 48).

$$\begin{aligned} \sigma(t) &= \sigma_0, \qquad 0 \le t \le t_0 \\ &= 0, \qquad t > t_0 \end{aligned}$$

Figure 48. Equation. $\sigma(t)$ for creep loading.

Figure 5, Figure 8, and Figure 11 could be solved to compute elastic, viscoelastic, and permanent strains, respectively. The MATLAB integration function was used to solve these equations. For the computation, material parameters were chosen randomly, as the goal was to verify the implementation. The values of σ_0 and t_0 were taken as 0.55 and 5 sec, respectively. The analytical solution is presented in Figure 49.

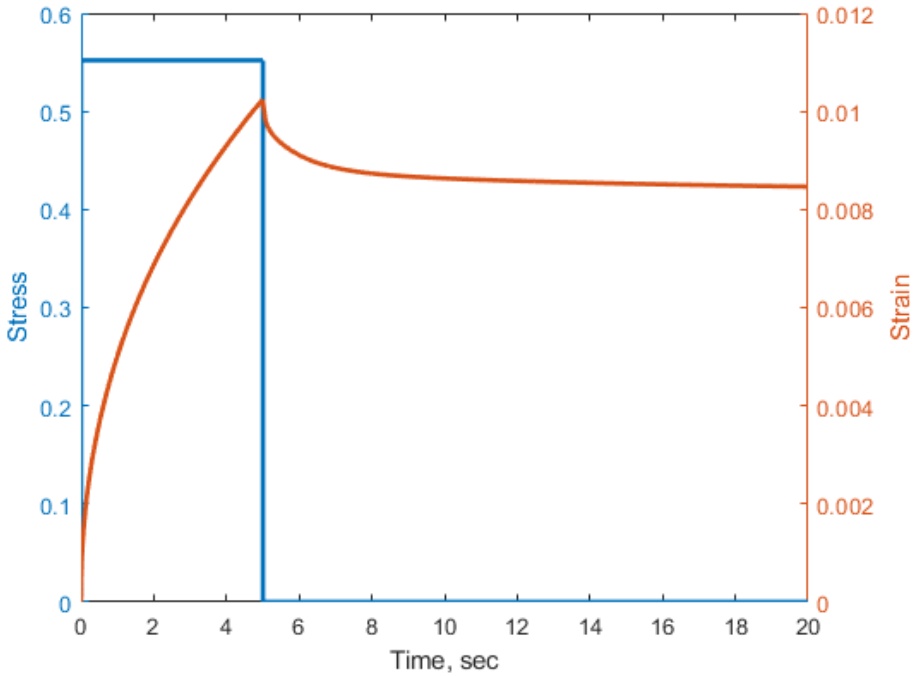

Figure 49. Graph. Analytical solution of model for creep loading.

To verify, the same problem was modeled in ABAQUS. Eight elements were used to model a cube; and boundary conditions were established to induce uniaxial and uniform stress conditions (Figure 50). All nodes on the bottom face were restrained in the vertical direction (Y-axis). Additionally, node 1 was restrained in the X- and Z-axes; and node 2 was restrained in the X-axis. The loading applied was similar to the stress depicted in Figure 49.

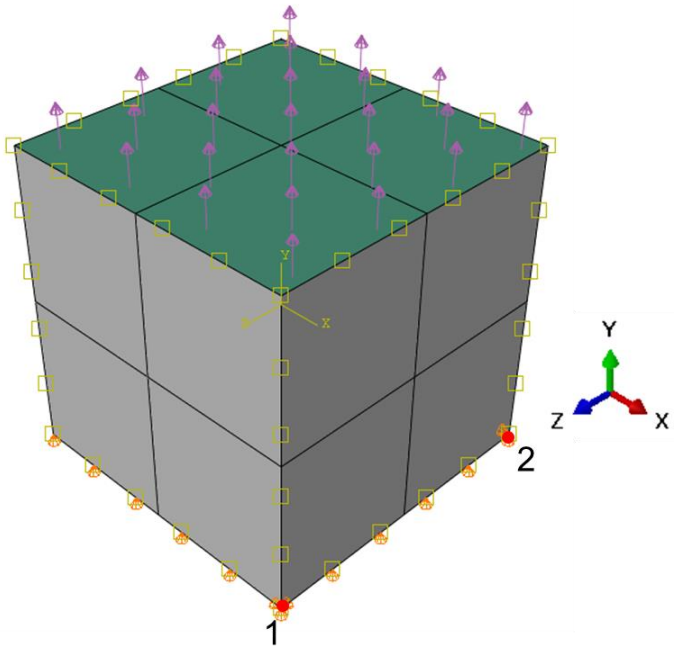

Figure 50. Illustration. Eight-element cube model in ABAQUS.

The strains obtained from the ABAQUS model and the analytical solution were exactly same, as illustrated in Figure 51. The strains presented in Figure 51 included the total strain ($\epsilon(t)$) and the permanent strain ($\epsilon_p(t)$). During the load application, permanent strain increased and remained constant after the load was removed, while total strain (which is greater than or equal to $\epsilon_p(t)$) increased with the load and eventually reached the same value as permanent strain sometime after the load application. Moreover, the elastic and viscoelastic strains were fully recovered.

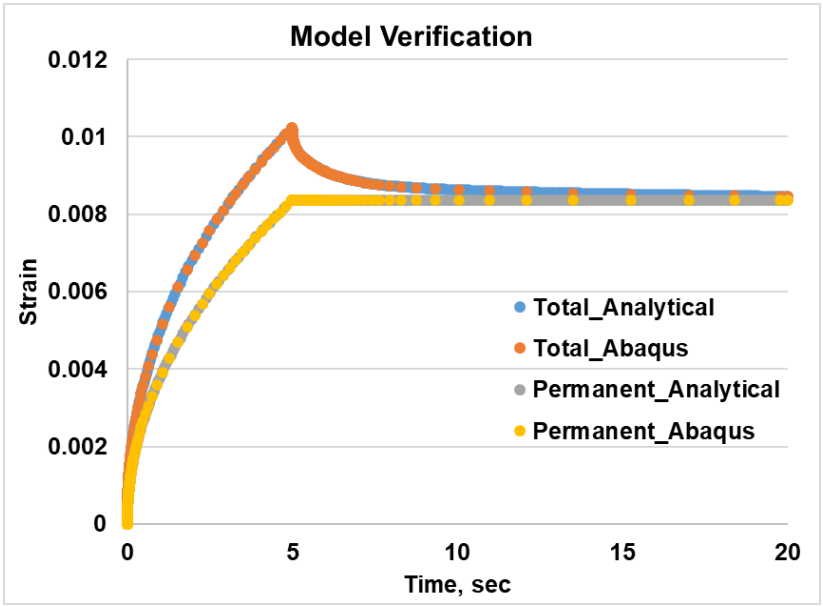

Figure 51. Graph. Analytical solution versus ABAQUS implementation.

MODEL-PARAMETER DETERMINATION

Experimental Program

Before validating the model, input parameters must be determined. For the dashpot element (η_0), two parameters (a, b) were needed to characterize permanent deformation. A common test used to characterize AC rutting behavior is the repeated-load permanent-deformation (RLPD) test, also known as the flow-number test (AASHTO T378). In the RLPD test, a cylindrical AC specimen was subjected to multiple cycles of haversine loading, with a rest period between cycles, either with or without confinement. Various truck spacings and speeds could be simulated by adjusting the rest period and loading time. RLPD tests were conducted without confinement by Alrajhi et al. (2022) to investigate the impact of the rest period on AC permanent-deformation behavior. The tests were performed on various AC mixes under different temperatures, loading conditions, and rest period levels (Figure 52). The RLPD results from the tests were utilized in this study to characterize the material behavior.

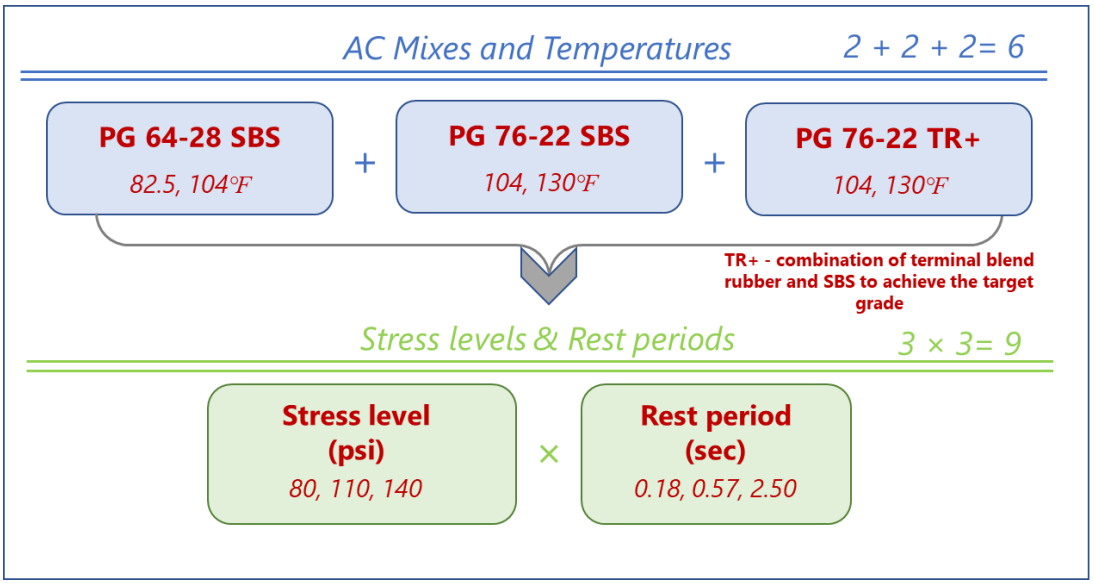

Figure 52. Illustration. RLPD test matrix conducted by Alrajhi et al. (2022).

In a previous project with the researchers, Alrajhi et al. (2022) conducted dynamic modulus tests for the AC mixes, presented in Figure 52, to characterize the linear viscoelastic behavior of AC. The tests measured material responses (strains) to haversine loading at various frequencies and temperatures. The strain responses were then shifted to a reference temperature to generate a master curve. This master curve could be fitted with a Prony series to obtain relaxation modulus coefficients. Typically, 10–15 KV elements were necessary to accurately characterize the material response over a broader frequency spectrum. Once the relaxation coefficients were determined, creep-compliance coefficients could be calculated using Figure 7 (Park and Schapery 1999). Therefore, the dynamic modulus tests could be used to obtain parameters E_i, τ_i, and E_0 (instantaneous modulus) of the GBM model. Figure 53 presents a sample from the experimental data. Note that the tertiary region was excluded, after identifying the point where the curvature changed from convex to concave.

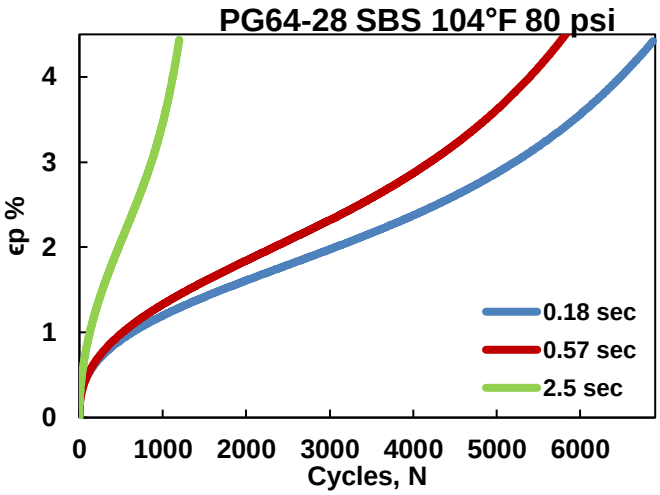

Figure 53. Graph. Permanent strain versus loading cycles from the RLPD test.

Parameter-Determination Procedure

The RLPD test could be simulated in ABAQUS using the same loading conditions (haversine loading with a rest period) and boundary conditions (bottom face pinned), as illustrated in Figure 54. To determine the material parameters, initial values for a and b were selected; and the resulting ϵ_p from the ABAQUS model was compared with the experimental data. Based on the comparison, the values of a and b could be adjusted until the model and test results aligned. However, this process was labor-intensive and time-consuming, as it required several trials and running thousands of cycles in ABAQUS.

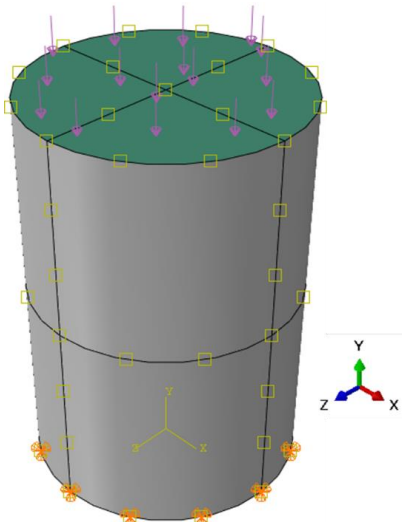

Figure 54. Illustration. RLPD test modeled in ABAQUS.

The test conditions for the dynamic modulus and RLPD were set to achieve a uniaxial stress state in the specimen. Therefore, ϵ_p and ϵ obtained from MATLAB's uniaxial (1D) formulation were deemed to be similar to ones obtained from ABAQUS for the same values of a and b. This hypothesis was

confirmed by running various cases in ABAQUS with different material parameters and comparing the results with those from MATLAB (Figure 55). In the tests, strain gauges were placed vertically in the center of the specimen. Similarly, in the model, strains were measured from the center region. This analysis was highly beneficial because running the 1D formulation in MATLAB took only a few seconds (owing to the formulation's simplicity) and was deemed valid, as the test conditions were conducted to emulate a 1D state. Thus, the 1D formulation could be used to determine the material parameters. Instead of using a trial-and-error method with the cylindrical model, Figure 11 could be fitted (with known σ and ϵ_p) using a least-square curve-fitting technique to obtain the parameters a and b. Figure 56 provides an example of applying fitting to experimental data.

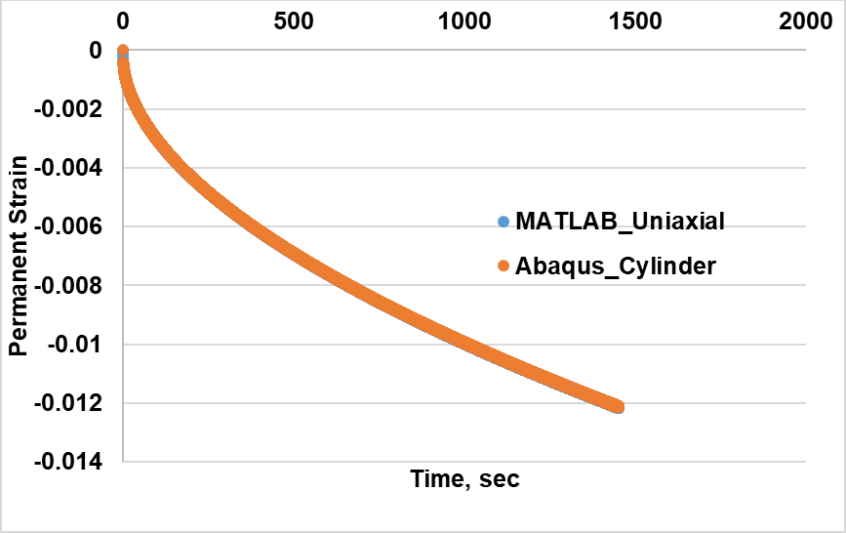

A. Permanent strain (ϵ_p).

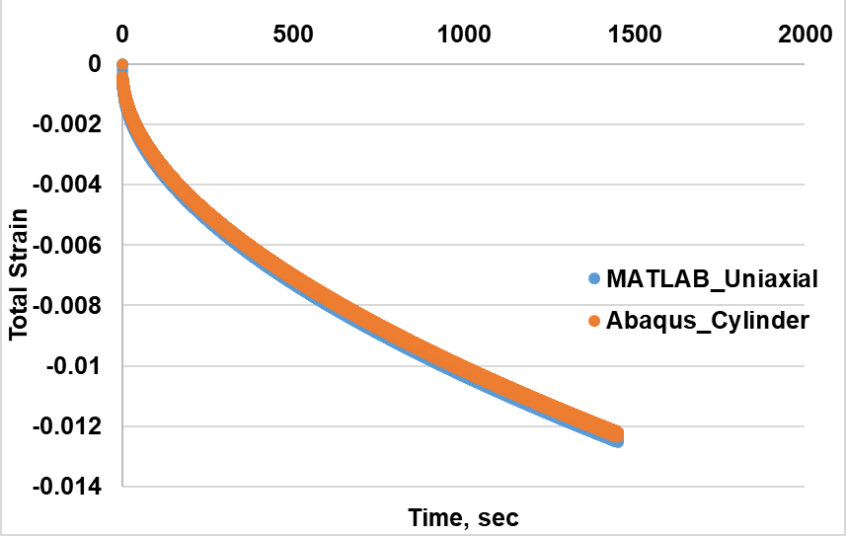

B. Total strain (ϵ).

Figure 55. Graph. Strain comparison between uniaxial formulation and ABAQUS cylinder model.

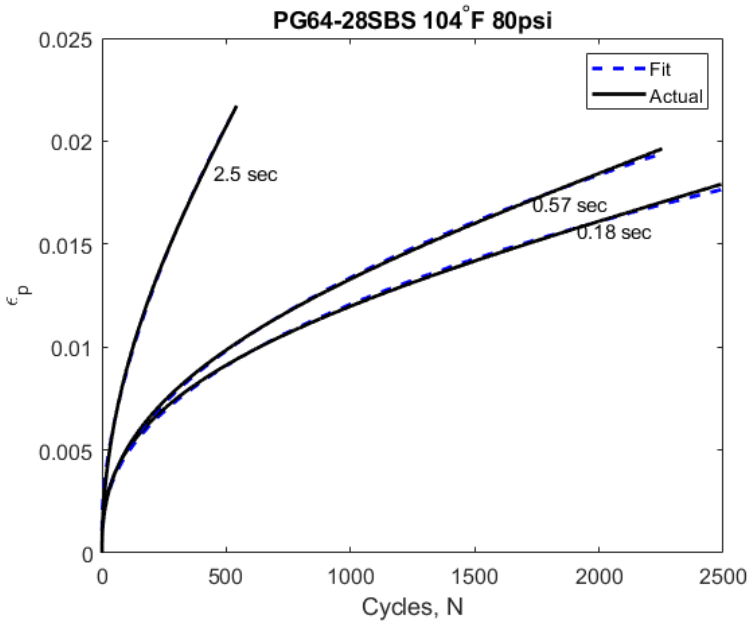

Figure 56. Graph. Experimental data versus fit using 1D formulation for various rest periods.

MODEL PARAMETERS

For the full suite of material parameters, a and b were obtained for all tests conducted at various loading conditions, rest periods, and temperatures, as summarized in Table 1. It is worth noting that *T*, *S*, and *R* represent temperature (°F), stress level (psi), and rest period (sec), respectively.

Table 1. Material Parameters a and b for AC Mixes in the Experimental Program

PG64-28SBS					PG76-22SBS					PG76-22TR+				
T	**S**	**R**	a	b	**T**	**S**	**R**	a	b	**T**	**S**	**R**	a	b
82.5	80	0.18	405.63	0.65	**104**	80	0.18	258.51	0.65	**104**	80	0.18	244.96	0.63
		0.57	232.87	0.64			0.57	138.23	0.61			0.57	152.52	0.58
		2.5	34.12	0.40			2.5	62.42	0.51			2.5	52.09	0.48
	110	0.18	427.73	0.59		110	0.18	241.93	0.62		110	0.18	233.39	0.58
		0.57	238.87	0.57			0.57	122.02	0.58			0.57	139.05	0.54
		2.5	86.99	0.46			2.5	53.94	0.43			2.5	54.22	0.40
	140	0.18	490.01	0.53		140	0.18	234.87	0.55		140	0.18	237.54	0.51
		0.57	230.26	0.53			0.57	127.15	0.52			0.57	134.63	0.48
		2.5	91.30	0.40			2.5	56.11	0.36			2.5	67.10	0.33
104	80	0.18	124.76	0.57	**130**	80	0.18	97.33	0.54	**130**	80	0.18	94.66	0.49
		0.57	82.45	0.52			0.57	56.66	0.49			0.57	52.89	0.43
		2.5	34.12	0.40			2.5	23.59	0.34			2.5	27.42	0.25
	110	0.18	125.05	0.49		110	0.18	85.67	0.42		110	0.18	81.57	0.42
		0.57	79.49	0.46			0.57	53.77	0.39			0.57	50.87	0.35
		2.5	33.53	0.29			2.5	24.30	0.17			2.5	25.41	0.15

PG64-28SBS					PG76-22SBS					PG76-22TR+				
T	S	R	a	b	T	S	R	a	b	T	S	R	a	b
	140	0.18	110.35	0.42		140	0.18	76.14	0.34		140	0.18	65.41	0.29
		0.57	76.54	0.37			0.57	49.90	0.30			0.57	43.91	0.26
		2.5	35.38	0.21			2.5	25.78	0.09			2.5	24.92	0.09

Sensitivity of Model Parameters

A sensitivity analysis was conducted to assess the impact of material parameters on permanent deformation, helping to determine the significance of each parameter on deformation. For all cases listed in Table 1, the parameter a was varied by 10% $(0.9a, 1.1a)$, while keeping b constant, and vice versa for b. The root mean square error (RMSE) was calculated between the permanent deformation for the bounds and the actual values (a, b). At lower temperatures (82.5° and 104°F), parameter b was found to be more sensitive than a across all mixes. However, at 130°F, a became slightly more critical than b at higher stress levels (110 and 140 psi).

Figure 57 illustrates the influence of these parameters on deformation in the experimental case. The dashed lines represent the actual experimental data; and the shaded area indicates the extent of influence due to changes in the parameters, which is also reflected in the RMSE values. In Figure 57, the shaded area for changes in b was considerably greater than for the changes in a; and the RMSE values for a were smaller than those for b. Figure 58 presents a case where a has a greater influence than b. The extent of the parameters' influence on ϵ_p depended on the load level, temperature, and rest period. Overall, a reduction in a and b could lead to increased permanent deformation, and vice versa.

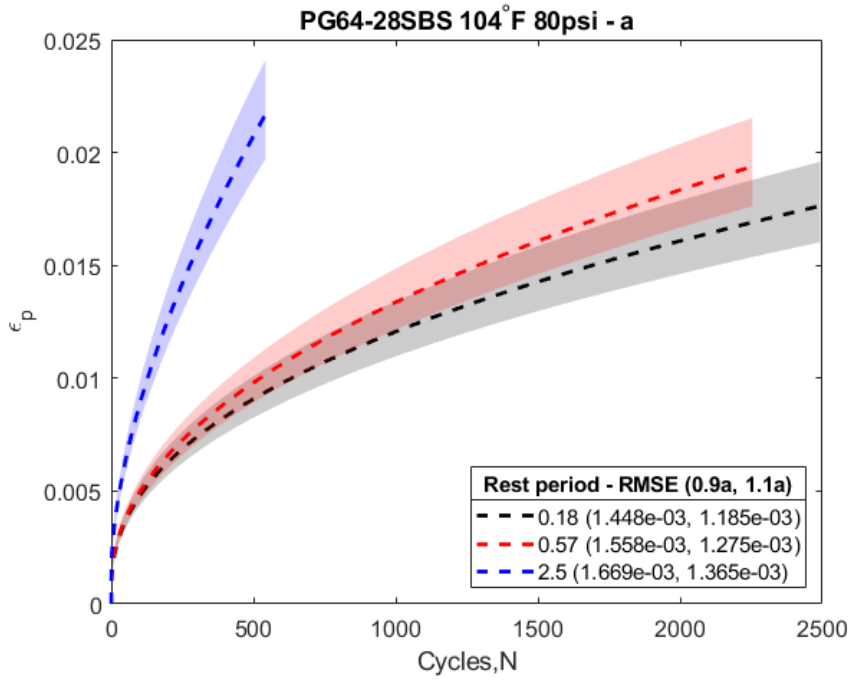

A. Sensitivity of a on ϵ_p.

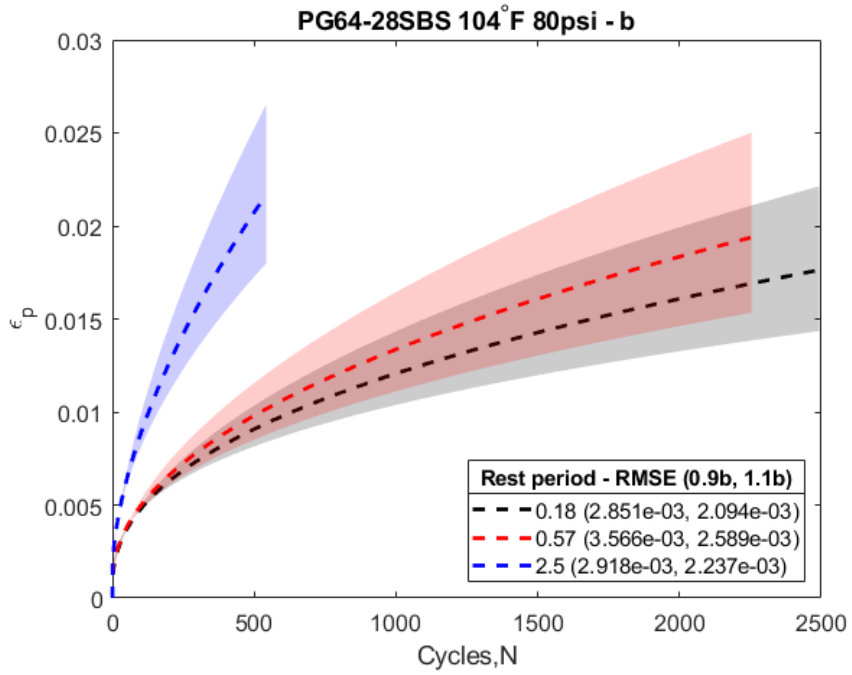

B. Sensitivity of b on ϵ_p.

Figure 57. Graph. Influence of parameters on permanent deformation for PG64-28SBS mix at 104°F and 80 psi.

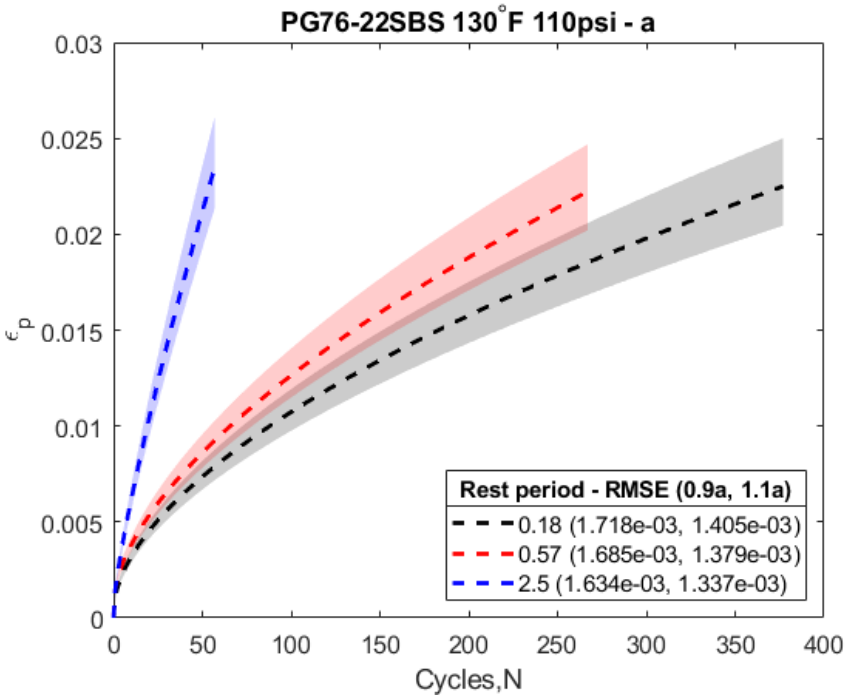

A. Sensitivity of a on ϵ_p.

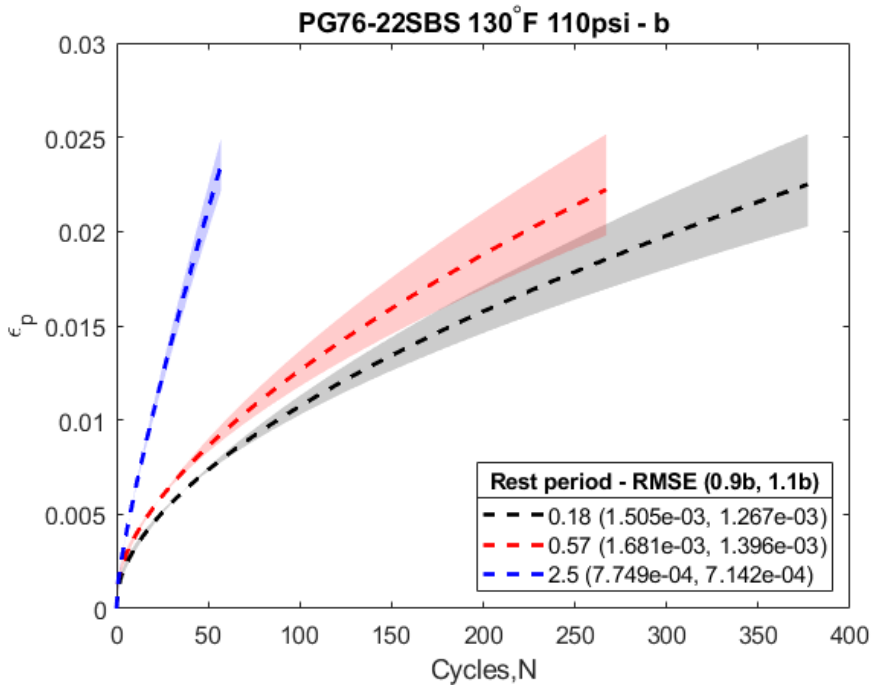

B. Sensitivity of b on ϵ_p.

Figure 58. Graph. Influence of parameters on permanent deformation for PG76-22SBS mix at 130°F and 110 psi.

Effect of Testing Parameters on Permanent Deformation

Based on the sensitivity analysis, parameter a changed exponentially; and b varied linearly with varying rest periods. Meanwhile, a showed minimal variation with stress-level changes, whereas b decreased linearly as stress levels increase. These trends were consistently observed across all cases. However, determining the impact of temperature on material parameters was challenging, given that only two temperatures were considered. Parameters a and b were plotted versus rest periods for a PG76-22SBS mix under various temperature and load conditions in Figure 59.

In Figure 59, the blue and orange curves represent the higher and lower temperatures in the tests, respectively. The resulting parameters for the two temperatures were clearly distinct, particularly for a. It is logical that changes in load levels should not significantly affect the material's viscosity (a), but they could influence the rate of deformation (b). Consequently, unlike b, parameter a remained relatively stable across various stress levels, especially at higher rest periods. The variation of both a and b with stress level was nearly linear. Moreover, the parameters for 110 psi were almost centered between the values at 80 and 140 psi (i.e., coincidental that 110 psi is equidistant from the two stress levels); and the variation in a was less pronounced than that in b across different stress levels.

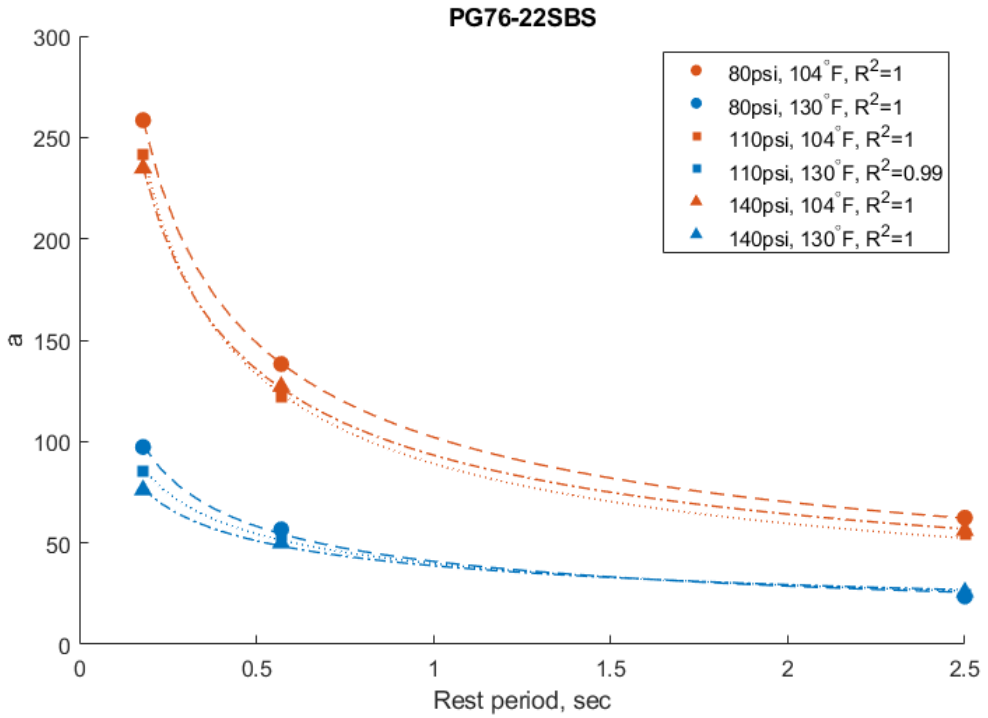

A. a

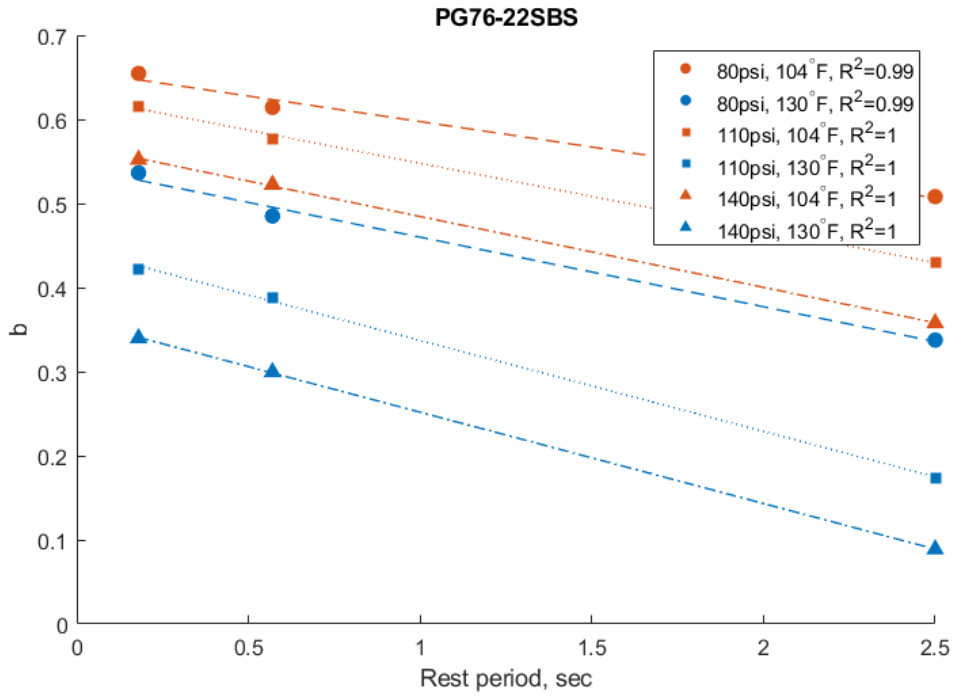

B. b

Figure 59. Graph. Material parameters (a and b) versus rest period for PG76-22SBS mix.

MODEL VALIDATION

Model validation is a process of checking a model's accuracy in representing real behavior. To validate parameters at 80 and 140 psi, ϵ_p was predicted at 110 psi due to the observed linear dependence of material parameters with stress levels (Figure 60 and Figure 61).

$$a_{pred}^{110} = \frac{(a_{act}^{80} + a_{act}^{140})}{2}$$

Figure 60. Equation. a_{pred}^{110}.

$$b_{pred}^{110} = \frac{(b_{act}^{80} + b_{act}^{140})}{2}$$

Figure 61. Equation. b_{pred}^{110}.

where $a_{pred}^{110}, b_{pred}^{110}$ are predicted parameters at 110 psi; and $a_{act}^{80}, a_{act}^{140}, b_{act}^{80}, b_{act}^{140}$ are actual parameters at 80 psi and 140 psi, respectively.

Predicted parameters were used to obtain $\epsilon_{p_{pred}}^{110}$ to compare results with the experimental data obtained at 110 psi for a PG76-22SBS mix (Figure 62). The predictions agreed with the experimental data, and similar predictions were observed for other mixes as well.

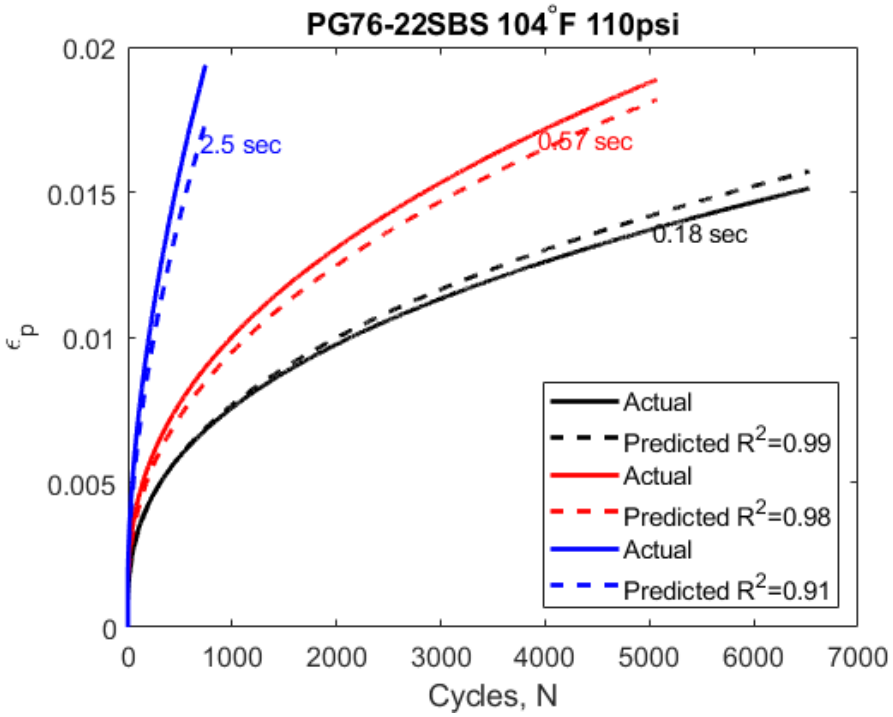

A. 104°F.

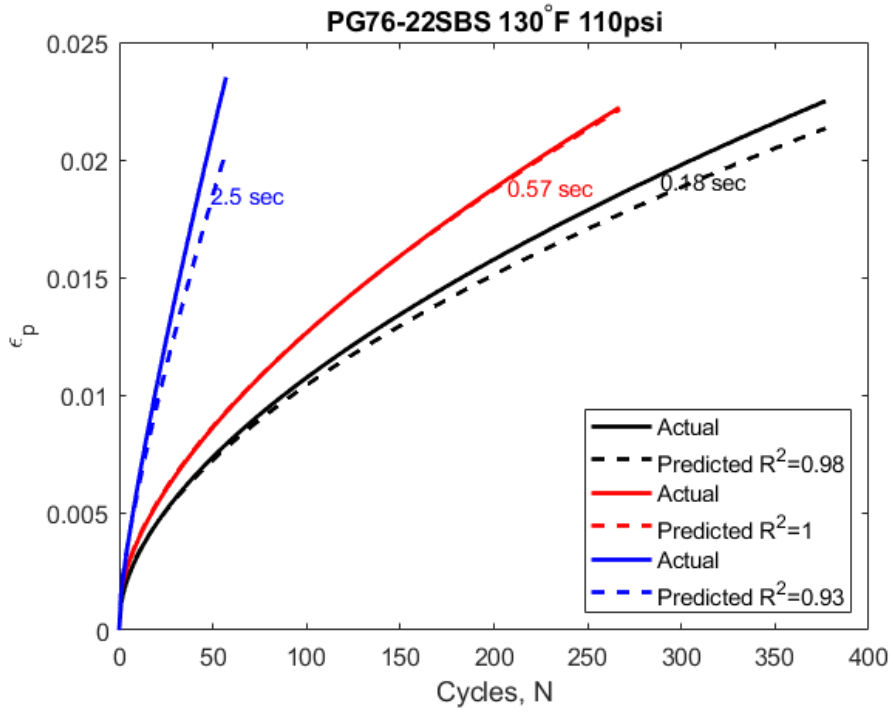

B. 130°F.

Figure 62. Graph. Actual versus predicted for a PG76-22SBS mix at 110 psi.

SUMMARY

In this chapter, a generalized nonlinear Burger's model was introduced to predict AC permanent deformation. This model could be integrated into an existing robust 3D FE pavement model to predict asphalt concrete (AC) rutting. To characterize this behavior accurately, a nonlinear power-law dashpot was utilized. The model was numerically formulated (using an incremental approach) to determine the material response for any arbitrary loading and boundary conditions. The 1D formulation was extended to a 3D formulation by applying the principles of linear elastic theory. As part of the 3D formulation, the stress increment ($\Delta\sigma$) and Jacobian ($\frac{\partial\Delta\sigma}{\partial\Delta\epsilon}$) were derived for implementation in ABAQUS as a UMAT. The numerical formulation could also be applied to implement Burger's model in any FE analysis software. The model was successfully implemented in ABAQUS and verified against an analytical solution (using MATLAB) for a simple creep-loading scenario. The model parameters were derived from the results of the repeated-load permanent deformation (RLPD) experiment and dynamic modulus tests. Validation was achieved by comparing the predicted deformation with actual experimental data. The nonlinear dashpot provided greater accuracy in capturing AC permanent-deformation behavior, as compared to the conventional dashpot (constant viscosity).

The dashpot parameters a and b—representing the deformation rate and viscoelastic material properties—were accurately and efficiently determined by correlating the uniaxiality of the flow-number test with the analytical solution. Sensitivity analysis revealed that ϵ_p was more sensitive to b

than a, particularly at lower temperatures (82.5° and 104°F). However, at a higher temperature (130°F), a became slightly more influential than b. Moreover, parameter a was found to be exponentially dependent on the rest period and unaffected by stress level; and b exhibited a linear dependence on both rest period and stress level. The model was successfully validated by interpolating material parameters across different stress levels, and a linear relationship was found suitable for the considered conditions. In the next chapter, detailed implementation of the 3D Burger's model formulation in a pavement FE model is discussed, along with its combined application with the load-pass approach.

CHAPTER 3: FE PAVEMENT MODEL

Conventionally pavements are modeled with simplified assumptions such as linear elastic pavement layers, uniform static loading over a circular contact area, and layer interactions using distributed springs. In this study, a 3D FE model for pavements was utilized, based on nearly three decades of work by Al-Qadi and colleagues to address the aforementioned shortcomings (Al-Qadi et al. 2008; Al-Qadi and Elseifi 2007; Elseifi et al. 2006; Hernandez et al. 2014, 2016; Yoo et al. 2006). Additionally, the 3D FE model offers the flexibility to include damage models to compute distresses. The 3D FE model developed by Al-Qadi et al. (2021), was used as the baseline model of in this study. Hence, the details of the geometric mesh optimization was already completed. Details of the model inputs and considerations are discussed in the following section.

MODEL OVERVIEW

Implicit Dynamic Analysis

Tire loading may be applied to pavements in several ways, including (i) static, (ii) quasi-static, and (iii) dynamic transient analysis. While static loading assumes time independence, the quasi-static approach incorporates a slowly moving load, wherein each timestep is assumed to represent one loading position. To the contrary, dynamic effects, such as inertia and damping, account for material time-dependent properties. For a dynamic analysis, energy-dissipation mechanisms dictate that a damping factor, friction factor, or viscoelastic material behavior needs to be implemented. In this study, the AC layers were modeled using linear viscoelasticity, which inherently accounted for damping and thus did not necessitate separate damping or friction factors. This modeling approach effectively captured the viscoelastic behavior of AC materials, making it a suitable choice for representing the AC layers' response to dynamic loading. To the contrary, Rayleigh damping was used for the granular and subgrade materials (unbounded layers), where the mass proportional damping and stiffness proportional damping are assumed to be 3.1416 and 7.95×10^{-4}, respectively (Wang and Al-Qadi 2011).

Material Characterization

Asphalt Concrete

AC layers were characterized as linear viscoelastic material and Burger's model (detailed in the previous chapter). The dynamic modulus (E*) is a fundamental mechanistic property that defines the linear viscoelastic behavior of AC as a function of temperature and loading time. To construct the dynamic modulus master curves, test results were shifted relative to a reference temperature, using the Williams–Landel–Ferry (WLF) time–temperature superposition principle. Williams et al. (1955) proposed an empirical equation to correlate the relaxation time of polymers at a temperature to their values at a reference temperature. The WLF equation could be written as presented in Figure 63:

$$log(a_T) = -\frac{C_1(T - T_g)}{C_2 + (T - T_g)}$$

Figure 63. Equation. Time–temperature shift factor.

where a_T is AC time–temperature shift factor, T is temperature of interest, T_g is reference temperature, and C_1, C_2 are fitting parameters.

Moreover, the dynamic modulus master curve could be obtained by fitting the experimental data to a Prony series. The Prony series is a mathematical representation of the viscoelastic behavior derived from the generalized Maxwell model, where the mechanical behavior of a material is represented through a combination of elastic (springs) and viscous (dashpots) elements (Soussou et al. 1970). Its general expression for the relaxation modulus could be written as follows:

$$G(t) = G_0 - \sum_{i=1}^{n} G_i\left(1 - e^{-t/\tau_i}\right)$$

Figure 64. Equation. Prony Series for a generalized Maxwell model.

where G_0 is long-term modulus, G_i is modulus of the i-th Maxwell term, τ_i is relaxation time of the i-th Maxwell term, and n is number of Maxwell term. Finally, the obtained Prony series was normalized to the instantaneous modulus to obtain a dimensionless expression for the relaxation modulus. This input is required for linear viscoelastic characterization in the commercial FE software ABAQUS. The normalized Prony series (Figure 65) could be written as follows:

$$g_R(t) = 1 - \sum_{i=1}^{n} g_i\left(1 - e^{-t/\tau_i}\right)$$

Figure 65. Equation. Normalized Prony Series.

where g_i is normalized modulus of the i[th] Maxwell term, and $g_i = {}^{G_i}/_{G_0}$.

Granular and Subgrade Materials

The stress dependency of granular layers is greatly influenced by the loading condition and AC-layer thickness—inherently, the stress applied on the granular material. Research by Wang and Al-Qadi 2013 underscored the importance of considering the nonlinearity of unbounded layers, particularly as loading and/or temperature conditions become more severe, and as loading speed decreases. The equations for the vertical, horizontal, and shear moduli could be written as follow, respectively, in Figure 66.

$$M_r^v = k_1 p_a \left(\frac{\theta}{p_a}\right)^{k_2} \left(\frac{\tau_{oct}}{p_a} + 1\right)^{k_3}$$

A. Vertical-resilient moduli

$$M_r^h = k_4 p_a \left(\frac{\theta}{p_a}\right)^{k_5} \left(\frac{\tau_{oct}}{p_a} + 1\right)^{k_6}$$

B. Horizontal-resilient moduli

$$G_r = k_7 p_a \left(\frac{\theta}{p_a}\right)^{k_8} \left(\frac{\tau_{oct}}{p_a} + 1\right)^{k_9}$$

C. Shear-resilient moduli

Figure 66. Equations. Resilient moduli of granular materials.

where M_r^v is resilient modulus in vertical direction; M_r^h is resilient modulus in horizontal direction; G_r is resilient modulus in shear direction; k_1, k_2, k_3, k_4, k_5, k_6, k_7, k_8, k_9 are regression coefficients, $\theta = \sigma_1 + \sigma_2 + \sigma_3$ = bulk stress expressed as the sum of principal stresses, p_a is unit reference pressure (atmospheric pressure), and $\tau_{oct} = \frac{1}{3}\sqrt{(\sigma_1 - \sigma_2)^2 + (\sigma_2 - \sigma_3)^2 + (\sigma_1 - \sigma_3)^2}$ = octahedral shear stress. For isotropic characterization, the vertical, horizontal, and shear-resilient moduli are estimated based on the same k-values so that $M_r^v = M_r^h = G_r$.

Layer Interaction

The Coulomb friction model provided a simplified way to represent the interaction between two surfaces in contact. The frictional force is assumed area-independent, velocity-independent, and linearly related to the normal force. Moreover, it was assumed that the surfaces in contact were characterized to be homogeneous and isotropic materials, so that frictional properties remain constant across the surfaces. This model delineated two frictional states: static (where there is no relative motion) and kinetic (characterized by sliding behavior). Sliding would be initiated once the shear force has exceeded the shear limit, established by the product of the coefficient of friction and the normal force. However, the frictional force did not increase beyond the shear-stress limit. Based on this assumption, the Coulomb friction model was implemented on all interfaces with granular and unbound layers, using the following expression in Figure 67.

$$\mu = \frac{\tau_{max}}{\sigma}$$

Figure 67. Equation. Coulomb friction model.

Where τ_{crit} is maximum shear stress prior to relative sliding of layers, μ is friction coefficient, and σ is normal stress at the interface.

In contrast, the elastic-stick model was implanted for the interaction between AC layers. In past research, the shear-stress distribution was found to be influenced by temperature and loading rate. Romanoschi and Metcalf (2001) conducted direct-shear testing and determined the values of τ_{max} = 205.2 psi and d_{max} = 0.062 in for AC interfaces, which were utilized in this study.

Temperature Profile Along the AC Layer

AC behavior not only depends on loading rate but also on temperature. At low temperatures, the AC modulus increases, whereas it decreases as the temperature rises, leading to substantial differences in the stress/strain fields. In this study, a temperature profile was assumed along the AC depth. For a two-layer system, consisting of an AC layer and a granular base, a temperature profile was derived based on the solution proposed by Wang et al. (2009). In this model, an initial temperature was defined on the AC surface as the reference temperature; and then a temperature distribution was estimated as a function of the AC-layer thickness, initial temperature, thermal conductivity, and diffusivity of the AC and granular material, alongside discrete pavement depths. In addition, it was assumed that the thermal conductivity of AC and the granular material were $\alpha_{ac} = 0.0226$ and $\alpha_g = 0.0323$ ft^2/h, whereas the thermal diffusivity was assumed to be $\lambda_{ac} = 1.67$ and $\lambda_g = 1.21$ BTU/h ft °F. The assumed maximum, minimum, and initial temperatures are summarized in Table 2.

Table 2. Parameters for Temperature Distribution

Condition	Tmax	Tmin	c
T1	54.00	45.00	31.00
T2	40.00	30.00	25.00
T3	28.06	20.00	20.00
T4	20.00	8.94	15.61

Load-Pass Approach

In past research efforts (Ramakrishnan et al. 2021), only a single axle was typically simulated, as influence from multiple truck axles on the single-point critical responses was deemed minimal (Ramakrishnan et al. 2021). Conventionally, simulating the moving load requires the presence of all tire load imprints at the beginning of the simulation, which is moved across the wheel path length. However, as one can imagine, the computational time exponentially increases when considering multiple axles (i.e., tandem, tridem, or full truck), compounded in the lateral direction if extended for a full axle. Additionally, capturing the permanent-deformation progression of the material requires repetitive loading on the pavement model. In fact, in this project, following the conventional scheme led to infeasible run time—mainly due to the extensive discretization along the longitudinal and transverse directions. To remediate this issue and the inability of the current model to model cyclic loading, the load-pass approach (LPA) was established. It enables the use of a smaller geometric domain under multi-axle or cyclic loading, while maintaining model accuracy.

Figure 68 presents the conventional approach of traversing three FE per load step. A previous study details that the identification of three elements per load was appropriate (Al-Qadi et al. 2021). At the initial time step, Tire 0, the full imprint is simulated for the conventional moving-load approach, followed by the beginning of the first moving-load step, Tire 1, wherein three moving-load transition elements are introduced. This procedure is typically followed until the last moving-load step, Tire n. The end of the simulation includes the full-load imprint, in line with the start of the simulation. This approach does not feasibly allow multi-axle or cyclic loading without requiring an extensively large geometrical FE domain.

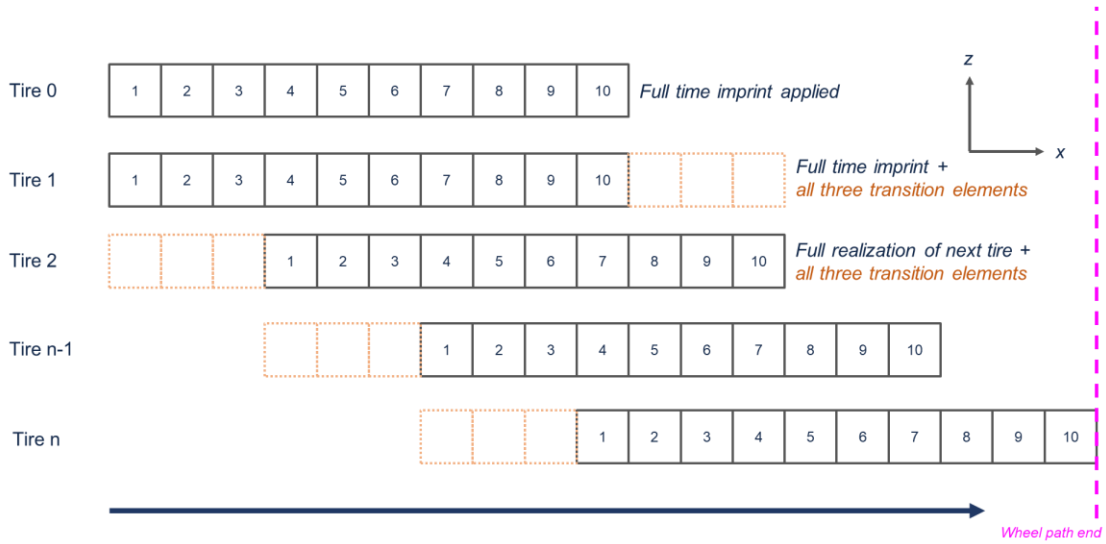

Figure 68. Illustration. Detailed element loading of the conventional moving load.

Instead of the conventional moving approach, the LPA was developed to incrementally introduce the load imprint via a partial entrance scheme. At the beginning of the LPA time step, only the three elements at the front leading edge of the wheel path were initiated for the partial entrance, following the three-element-per-step moving scheme (Figure 69). Depending on the contact length of the tire imprint, the moving scheme continued until the full-load imprint manifested or was present in the wheel path length.

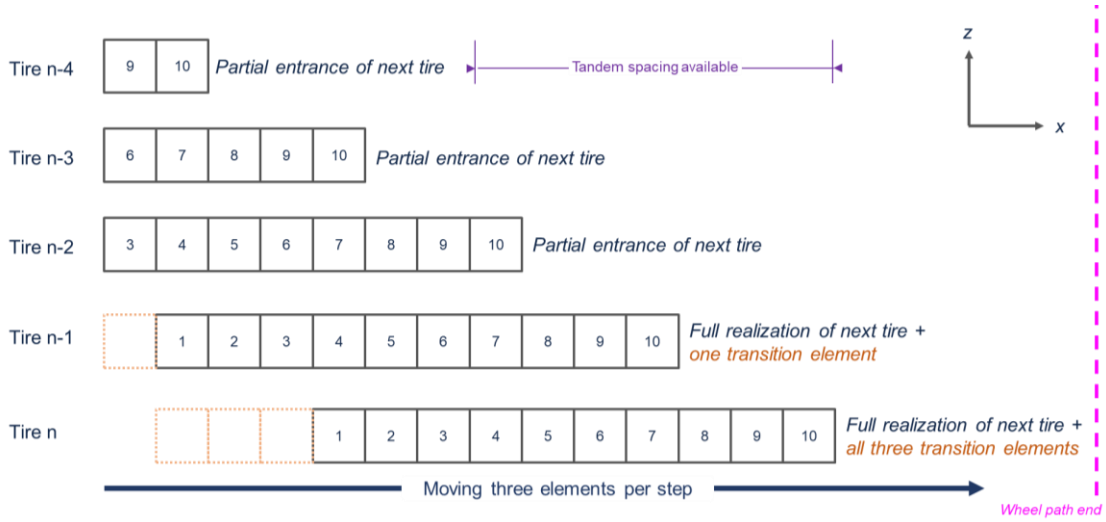

Figure 69. Illustration. Detailed element loading of the load-pass approach entrance.

As the front edge of the load imprint reached the end of the wheel, a partial exit scheme was implemented, similarly to the partial entrance scheme. In this stage of the load application, the load imprint exited the model three elements per load step, as illustrated in Figure 70. The LPA aimed to emulate a “viewing window” effect, reminiscent of observing truck axles’ passing by from left to right.

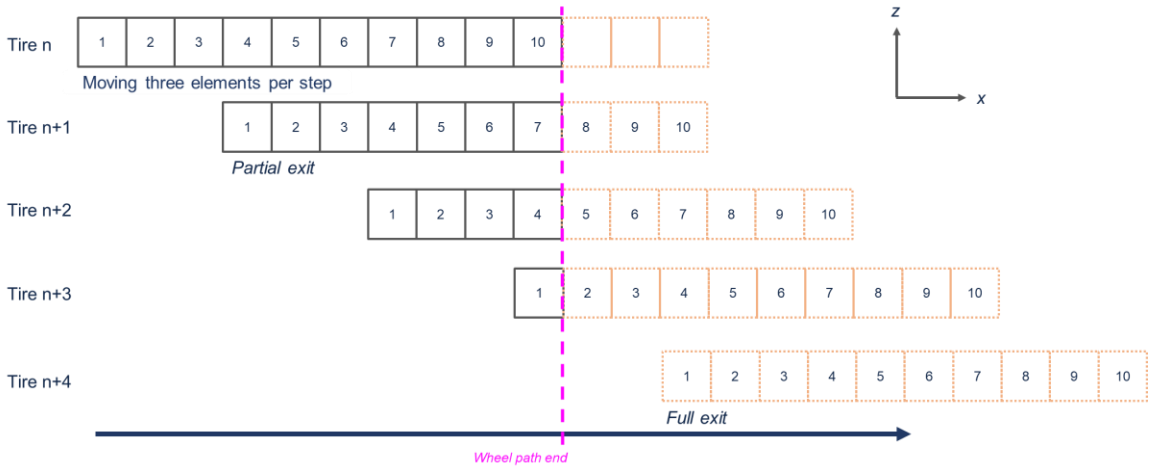

Figure 70. Illustration. Detailed element loading of the load-pass approach exit.

Another key component in the proposed LPA is proper implementation of the rest period. In the conventional moving-load approach, a relatively long wheel path would have been required to account for the rest period under one cycle of loading (recall that the conventional approach cannot impose loading cycles). Considering the transient loading nature at the beginning and end of the wheel path, due to the partial entrance and exit schemes, respectively, the assumed start location of the rest period was at mid-length of the model (with steady-state loading). Given an assumed traveling speed, the required distance for a specific rest period was calculated. However, as the LPA's motivation was to narrow the wheel path length, there would be a residual distance to complete the full duration of the rest period. As the rest period entails the unloaded state, the residual time to complete the full rest-period duration was implemented through "unloaded" load steps in ABAQUS. A time-step increment was selected to be 0.05 sec to discretize the residual time. Immediately after the full rest period was completed, the next partial-entrance scheme would begin and be followed by the steps described above until the desired number of cycles was reached. An illustrative example of the rest-period implementation is presented in Figure 71, where X is the assumed wheel path length.

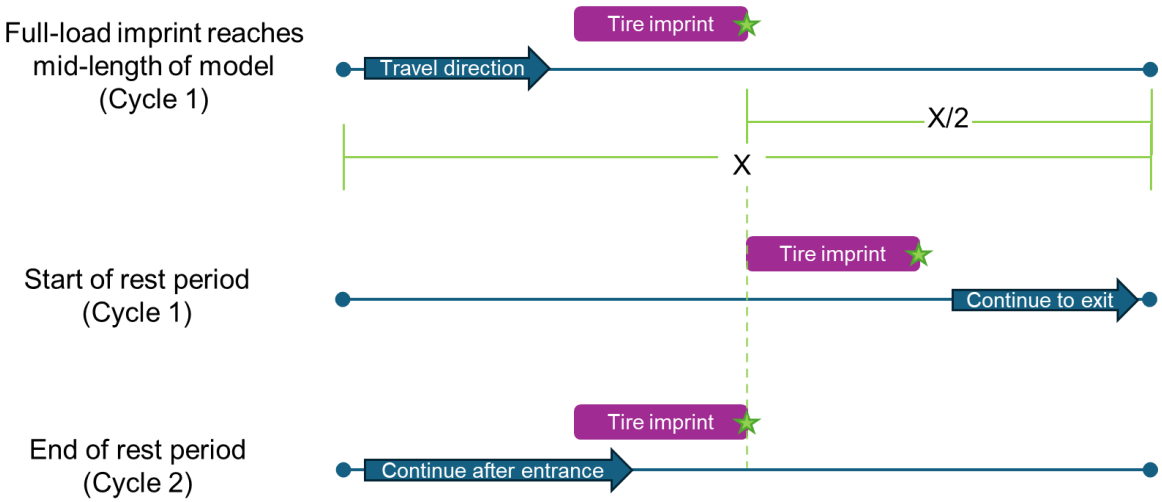

Figure 71. Illustration. Rest-period assumption from one cycle to another.

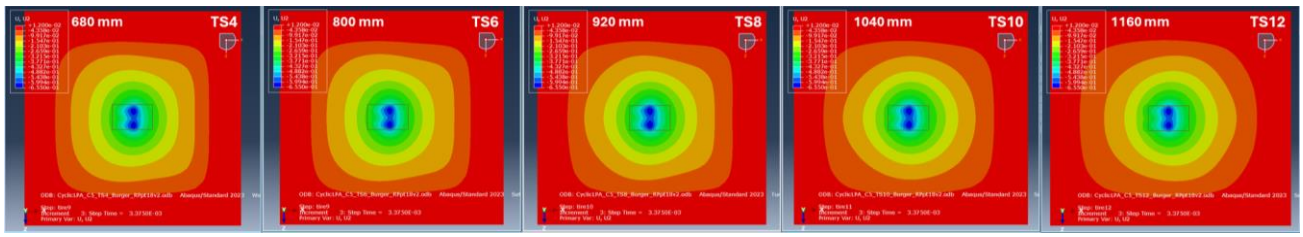

Figure 72. Illustration. Sensitivity analysis of LPA wheel path length.

Given the motivation to narrow the wheel path length to reduce computational time, several wheel path lengths were evaluated to determine the appropriate wheel path length for the proposed LPA. Figure 72 illustrates the five tested scenarios, with increasing wheel path length from 680 to 1,160 mm. It can be observed that the shortest wheel path length of 680 mm led to a boundary-reflection issue, given that the outer contours that surrounded the load imprint no longer radiated with a circular shape; instead, they assumed the shape of the model geometry. In contrast, the longest wheel path of 1,160 mm did not result in boundary issues.

Moreover, the total compressive strain throughout the five-cycle application was compared for all the wheel path length scenarios. As illustrated in Figure 73, the extracted max responses did not vary significantly after five loading cycles for the sensitivity analysis of the wheel path length, given that the strains were extracted within the wheel path. However, as the GNN relies on the surrounding 3D domain as input data, the selected wheel path length was 920 mm to abate boundary-impact issues. This selection allowed eight loading steps to move the full imprint prior to reaching the wheel path length limit, then exiting soon after.

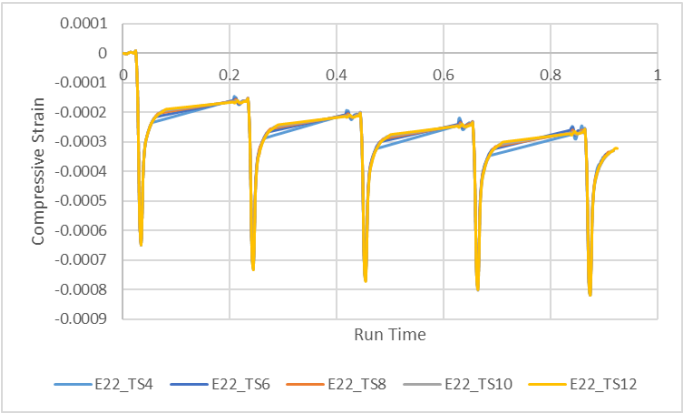

Figure 73. Graph. Total compressive strain, E22, results from varying LPA wheel path lengths.

Furthermore, three cases were compared: elastic, viscoelastic, and the Burger's model to evaluate the impact of characterizing the AC layers with Burger's model. As illustrated in Figure 74, the vertical compressive strain was highest for the Burger's model, followed by the one from assuming viscoelasticity. In addition, only the Burger's model resulted in an accumulation, as evidenced by the total compressive strain (which included the plastic strain), while the elastic and viscoelastic cases rebounded to nearly zero, as neither material characterization could capture the rutting behavior.

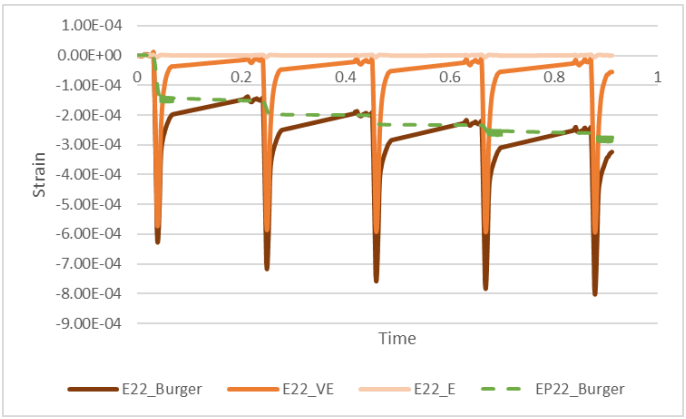

Figure 74. Graph. Comparison of elastic, viscoelastic, and Burger's model assumptions for the AC layer.

The corresponding total vertical compressive strain and stress outputs are presented in Figure 73. The accumulation presented in the total vertical compressive strain, comprised of elastic, viscoelastic, and plastic strains, was driven by the implementation of the Burger's model. In contrast, the loading pulses, as would be expected, returned to zero after unloading. It was also evident that each loading cycle increased the rut depth, as expected. Hence, the combined implementation of the load-pass approach and the Burger's model for AC-material characterization enabled quantifying rut-depth accumulation under a number of loading cycles.

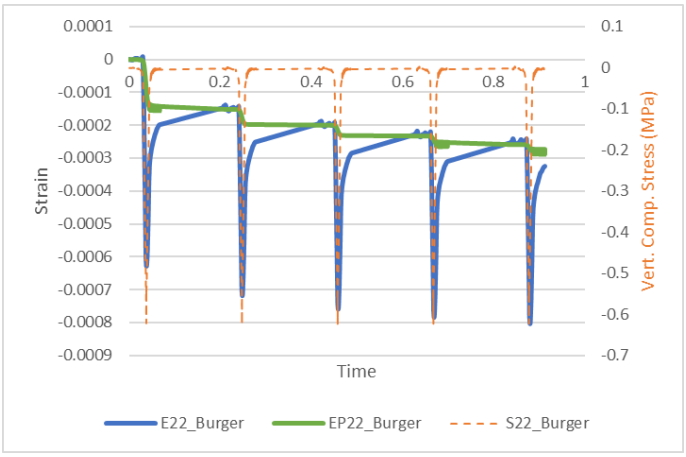

Figure 75. Graph. Total vertical compressive strain (E22), vertical compressive plastic strain (EP22), and vertical compressive stress (S22) outputs after five cycles, using Burger's model assumptions for the AC layer.

NUMERICAL MATRIX

A total of 36 simulations for the single-axle cases was completed, as detailed in Table 3. The parametric analysis constrained the cyclic loading to the same-single axle, DTA with 34 kips, under uniform rest periods to identify the baseline pavement behavior when the Burger's model was applied. Appropriate speeds were assumed for the thick and thin pavements, representative of

interstate and low-volume roadways, respectively (Figure 76). Two rest periods for unloading were assumed, following the laboratory testing matrix for rutting. In addition, reference linear viscoelastic cases were simulated for relative comparisons of the pavement responses. The researchers acknowledge that in reality a nonuniform rest period would be more suitable to emulate a full truck, given the varying axle distances. However, in this study, the same rest period was maintained between each loading cycle.

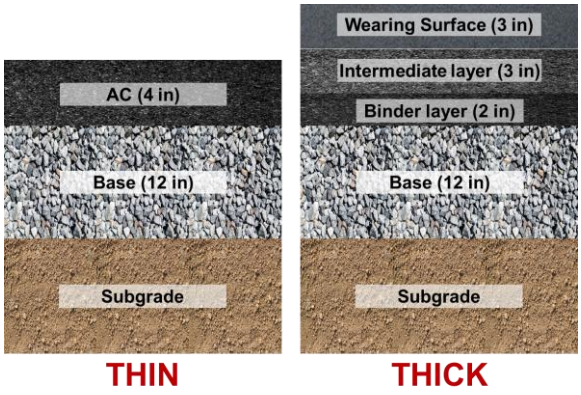

Figure 76. Illustration. Thin and thick sections.

Table 3. Pavement FE Simulation Parameters

Structure	Thick (11-in. AC) (only one section)	Thin (4-in. AC) (strong and weak)
Speed	70 and 40 mph	40 and 10 mph
Tire Type	DTA (34 kips)	
Rest Period	0.57 and 2.50 sec	
Temperature	130°F (82°F for thin, weak section), 104°F, and 68°F (reference LVE) profiles	
Total Number of Cases	*1 × 2 × 1 × 2 × 3 = 12 cases*	*2 × 2 × 1 × 2 × 3 = 24 cases*

The WLF and Prony series coefficients for the AC layers are presented in Table 4 and

Table 5, respectively.

Table 4. Williams–Landel–Ferry Coefficients of Asphalt Mixtures

Component	**Thin PG64-28 SBS (Weak)**	**Thin PG76-22 SBS (Strong)**	**Thick PG 76-22 SBS Wearing Surface**	**Thick PG 76-22 TR+ Intermediate Layer**	**Thick PG 64-28 SBS Binder Layer**
C_1	39.498	61.810	61.810	23.169	39.498
C_2	335.307	506.514	506.514	180.329	335.307
Reference Temperature (°F) = 70					

Table 5. Prony Series Coefficients of Asphalt Mixtures

Thin PG64-28 SBS (Weak)		Thin PG76-22 SBS (Strong)		Thick PG 76-22 SBS (Wearing Surface)		Thick PG 76-22 TR+ (Intermediate Layer)		Thick PG 64-28 SBS (Binder Layer)	
τ_i	$\bar{g}_i, \bar{k}_i$	τ_i	$\bar{g}_i, \bar{k}_i$	τ_i	$\bar{g}_i, \bar{k}_i$	τ_i	$\bar{g}_i, \bar{k}_i$	τ_i	$\bar{g}_i, \bar{k}_i$
1.00E-05	0.0433907	1.00E-05	0.0820033	1.00E-05	0.0820033	1.00E-05	0.153288	1.00E-05	0.043391
0.0001	0.262994	1.00E-04	0.208093	1.00E-04	0.208093	1.00E-04	0.179055	0.0001	0.262994
0.001	0.169979	0.001	0.154912	0.001	0.154912	0.001	0.134329	0.001	0.169979
0.01	0.249581	0.01	0.237054	0.01	0.237054	0.01	0.198675	0.01	0.249581
0.1	0.136212	0.1	0.132357	0.1	0.132357	0.1	0.141561	0.1	0.136212
1	0.091877	1	0.121209	1	0.121209	1	0.108029	1	0.091878
10	0.0176686	10	0.0171039	10	0.0171039	10	0.03617	10	0.017669
100	0.0167445	100	0.0329051	100	0.0329051	100	0.033227	100	0.016745
1000	0.0027767	1000	1.24E-12	1000	1.24E-12	1000	0.002464	1000	0.002777
10000	0.0022501	10000	0.0070173	10000	0.00701731	10000	0.00604	10000	0.00225
100000	0.0005953	100000	4.54E-14	100000	4.54E-14	100000	9.43E-11	100000	0.000595

It is worth noting that the granular base for the thin-pavement section was assumed to be stress-dependent, while the subgrade and the supporting layers of the thick-pavement section were assumed to be elastic materials, given that the influence of stress-dependency reduced with pavement depth.

RESULTS AND FINDINGS

The results of all thin- and thick-pavement simulations are presented in this section. For cases that implemented a 68°F-temperature profile, the AC-material characterization was assumed to be linear viscoelastic; the cases under high temperature profiles (104° and 130 °F) considered the Burger's model to quantify permanent deformation.

Tensile Strains

In general, tensile strains at the top and the bottom of the AC associates with the near-surface and bottom-up fatigue cracking, respectively. The critical/maximum tensile strains at the top and bottom of the AC layer for thick and thin cases are presented in Table 6 and Table 7, respectively, under varying materials (for thin section only), speeds, rest periods, and temperatures. ϵ_{11} ($E11$) corresponds to longitudinal strain, and ϵ_{33} ($E33$) corresponds to transverse strain.

Table 6. Critical Tensile Strain for Thick (TK) Pavement–Section Cases

Speed (mph)	Rest Period (sec)	Temperature (℉)	E11_top_AC ($\mu\epsilon$)	E33_top_AC ($\mu\epsilon$)	E11_bot_AC ($\mu\epsilon$)	E33_bot_AC ($\mu\epsilon$)
40	0.57 (RP2)	68	0.41	2.81	39.67	32.55
		104	29.84	59.41	213.90	180.76
		130	100.05	107.45	333.29	275.32
	2.50 (RP3)	68	0.41	2.62	39.14	31.69
		104	42.67	78.40	245.47	209.50
		130	125.04	147.76	325.19	340.71
70	0.57 (RP2)	68	0.67	4.02	38.63	32.47
		104	35.09	46.96	199.53	168.18
		130	89.31	71.97	300.14	238.13
	2.50 (RP3)	68	0.67	3.85	38.41	31.89
		104	41.64	59.63	223.13	180.03
		130	100.47	86.68	290.96	253.92

Table 7. Critical Tensile Strains for Thin (TN) Pavement–Section Cases

Material	Speed (mph)	Rest Period (sec)	Temperature (℉)	E11_top_AC ($\mu\epsilon$)	E33_top_AC ($\mu\epsilon$)	E11_bot_AC ($\mu\epsilon$)	E33_bot_AC ($\mu\epsilon$)
Strong	10	0.57 (RP2)	68	0.83	25.87	129.63	105.68
			104	234.60	283.32	631.13	752.49
			130	272.37	521.51	1172.64	1460.95
		2.50 (RP3)	68	0.83	22.88	126.41	99.35
			104	255.91	475.71	793.67	912.66
			130	274.41	524.09	1219.72	1523.08
	40	0.57 (RP2)	68	3.48	16.55	106.38	82.61
			104	212.78	212.60	496.06	578.24
			130	370.11	494.47	1131.50	1223.08
		2.50 (RP3)	68	3.48	15.61	104.81	80.88
			104	222.35	292.90	553.28	651.64
			130	364.45	479.02	1087.15	1210.31
Weak	10	0.57 (RP2)	68	1.21	34.38	146.79	123.32
			82	169.06	205.31	450.96	541.91
			104	246.32	354.19	828.13	885.05
		2.50 (RP3)	68	1.21	29.72	142.30	114.16
			82	227.93	436.44	643.38	793.45
			104	264.57	601.89	967.78	1021.98
	40	0.57 (RP2)	68	4.53	21.17	119.60	93.54
			82	198.77	211.02	503.51	529.34
			104	225.44	224.78	562.50	626.60
		2.50 (RP3)	68	4.53	19.77	116.79	91.02
			82	160.82	239.35	461.56	545.48
			104	231.58	367.48	614.95	696.12

In Table 6 and Table 7, the tensile-strain magnitudes followed expected trends and were consistent with respect to the inputs of the model such as temperature, speed, rest period, and material property (Figure 77). As temperature increased, the responses increased in magnitude because the AC became softer. Similarly, as the speed increased, the responses decreased as loading frequency increased, resulting in a stiffer AC. In contrast, the longitudinal tensile-strain magnitude could be either higher or lower, as compared to the transverse tensile (Al-Qadi et al. 2004; Garcia and Thompson 2008). However, the recovery time of the transverse tensile was always shown to be higher than that of the longitudinal strain, especially under higher temperatures wherein the viscous component induced a higher lag. Longitudinal strains recovered faster due to the movement of the load. As the load approached or left an element in the pavement model, the element was under compression in the longitudinal direction that resulted in a faster recovery. The element was in tension only when the load was exactly/nearly above the element. However, the element was constantly stretched in the transverse direction, which led to a slower recovery.

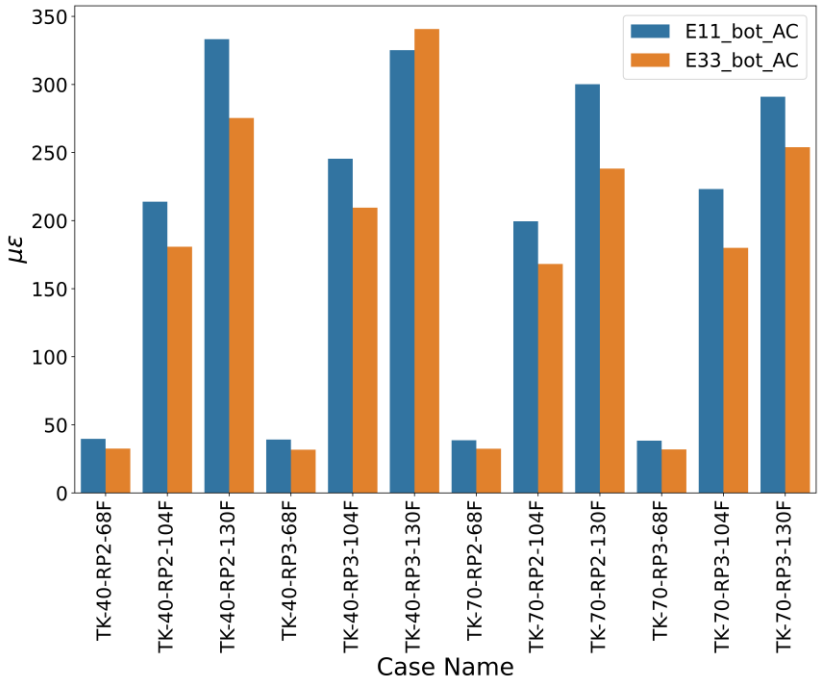

Figure 77. Graph. Maximum tensile strains for all the thick cases.

In addition, the tensile strains, extracted at the AC bottom, were plotted as a function of time for the thick section in Figure 78. At 68°F, ϵ_{11} were consistently higher than ϵ_{33} for all the load cycles, while the recovery is similar (Figure 78a). Under high temperature, the magnitude of transverse strains were smaller than that of the longitudinal strains for the first few cycles (Figure 78b and c).

Due to slower recovery, transverse strains accumulated; and the magnitude eventually surpassed the longitudinal strain, thus making it critical for fatigue-cracking analysis. For the Burger's model cases, the tensile strains will have permanent strain due to the Poisson's effect; hence, it increased with each load cycle. The element was stretched and compressed in the transverse and vertical direction, respectively. Therefore, the longitudinal strain could be observed to reduce with the load application.

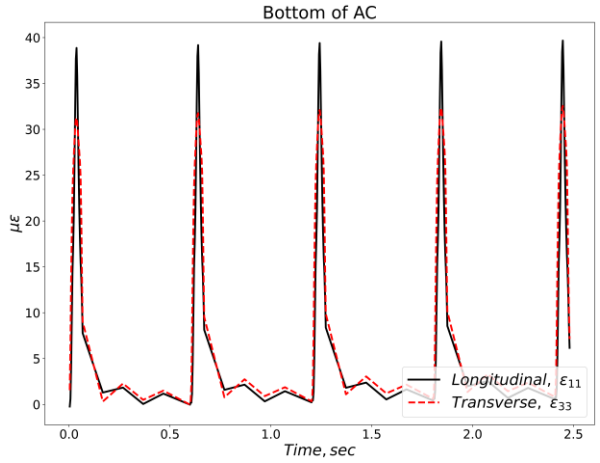

A. 68°F (reference case, linear viscoelastic AC).

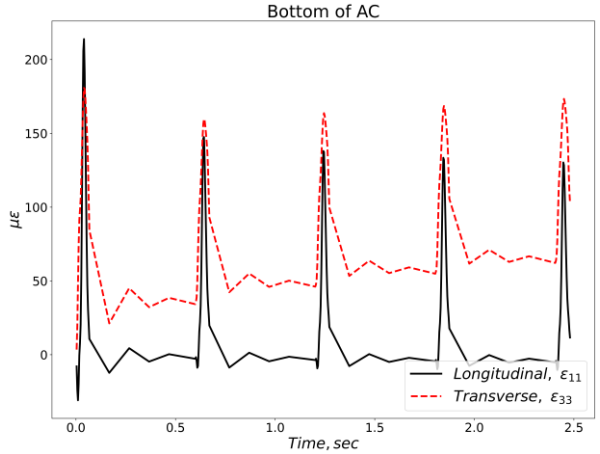

B. 104°F (Burger's model AC).

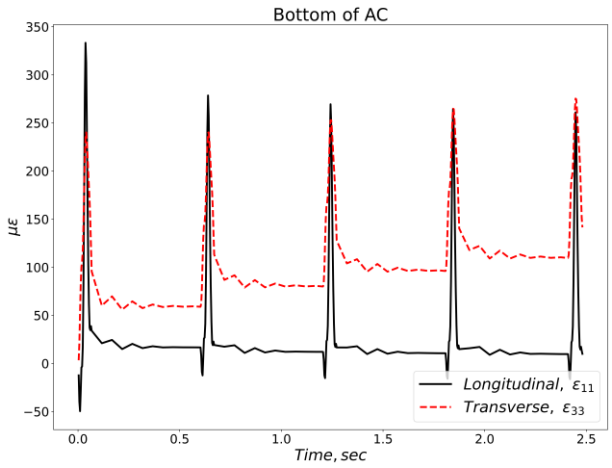

C. 130°F (Burger's model AC).

Figure 78. Graph. Tensile strains per load cycle for the thick-pavement section at 40 mph with 0.57-sec rest period.

Compressive and Permanent Strains

In the literature, rutting is associated with compressive strains within the pavement structure. Usually, MEPDG transfer functions are used to compute rutting, based on the vertical compressive strains within the layers. For the Burger's model cases, the permanent strain (ϵ_{22}^{p}) was directly obtained from the model for the AC layer; and for reference cases, only the viscoelastic compressive strain was calculated. In either case, elastic compressive strain was obtained for unbound materials, as they were only characterized as nonlinear, anisotropic stress-dependent, or linear elastic. The maximum compressive/permanent strain for the thick and thin cases are presented in Table 8 and Table 9, respectively.

Table 8. Critical Permanent Strains for Thick-Section Cases

Speed (mph)	Rest Period (sec)	Temperature (℉)	E22_AC ($\mu\epsilon$)	E22_Base ($\mu\epsilon$)	E22_Subgrade ($\mu\epsilon$)
40	0.57 (RP2)	68	31.95	19.14	65.84
		104	363.25	310.10	244.96
		130	879.73	828.85	275.75
	2.50 (RP3)	68	31.24	18.78	64.99
		104	482.59	373.29	256.57
		130	949.56	942.51	273.54
70	0.57 (RP2)	68	31.15	17.66	63.23
		104	265.62	242.87	245.05
		130	559.88	664.96	270.21
	2.50 (RP3)	68	30.78	17.45	62.71
		104	333.44	277.27	254.56
		130	578.36	721.01	267.71

Table 9. Critical Permanent Strains for the Thin-Section Cases

Material	Speed (mph)	Rest Period (sec)	Temperature (℉)	E22_AC ($\mu\epsilon$)	E22_Base ($\mu\epsilon$)	E22_Subgrade ($\mu\epsilon$)
Strong	10	0.57 (RP2)	68	106.15	35.87	1417.90
			104	777.42	675.90	3736.36
			130	1564.64	1650.82	5082.51
		2.50 (RP3)	68	101.68	34.05	1355.58
			104	1296.32	760.73	4427.70
			130	2805.10	2065.66	5030.18
	40	0.57 (RP2)	68	84.66	26.74	1208.76
			104	365.55	362.33	3034.50
			130	621.60	1131.96	5664.02
		2.50 (RP3)	68	83.09	26.28	1198.57
			104	553.71	381.15	3261.30
			130	774.13	1223.12	5498.32

Material	Speed (mph)	Rest Period (sec)	Temperature (℉)	E22_AC ($\mu\epsilon$)	E22_Base ($\mu\epsilon$)	E22_Subgrade ($\mu\epsilon$)
Weak	10	0.57 (RP2)	68	122.66	43.67	1560.27
			82	432.17	327.90	2755.91
			104	1161.24	923.34	4414.71
		2.50 (RP3)	68	116.16	40.87	1480.83
			82	1075.77	446.94	3616.76
			104	2090.26	1154.08	5113.58
	40	0.57 (RP2)	68	95.66	31.35	1243.12
			82	206.08	386.32	3202.53
			104	463.16	459.64	3506.14
		2.50 (RP3)	68	93.16	30.59	1271.14
			82	444.32	245.04	2776.30
			104	728.98	465.02	3737.13

Similar to the tensile strains, the trends of the compressive and permanent strain responses were logical with respect to the inputs (Figure 79). Higher strains resulted under a longer rest period, aligned with the the experimental data. The viscoelastic compressive strain (ϵ_{22}) for the reference cases (68°F) was not affected by the rest period, which demonstrated the inability of the linear viscoelastic material model to capture the effect of the rest period. The compressive/permanent strains for the thick section are plotted in Figure 80 as a function of time at the location of the maximum response.

At 68°F, the magnitude of compressive strains did not change with load application; and the responses were nearly fully recovered within the rest period. When the AC temperatures increased to 104° and 130°F, permanent deformation increased per load cycle but at a decreasing rate with load application. Also, the permanent strain did not increase during the rest period due to the absence of load (Figure 75). Similar trends were observed for other cases in the matrix.

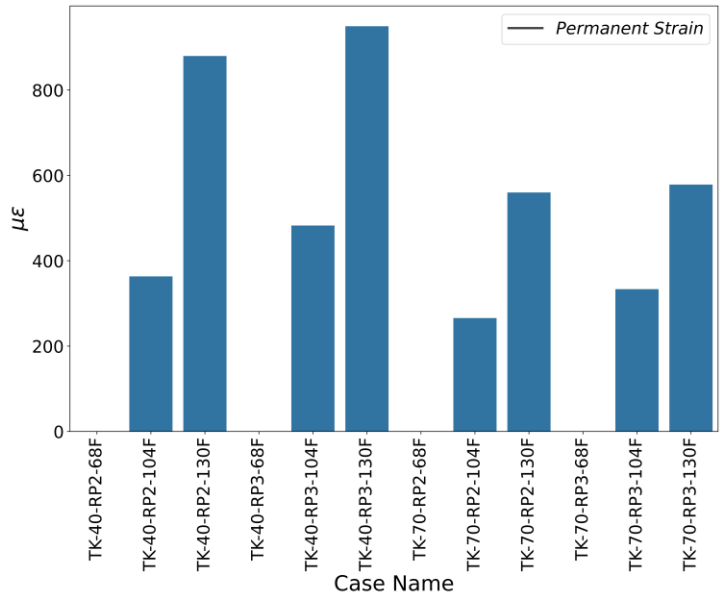

Figure 79. Plot. Maximum vertical strains in AC for all the thick cases.

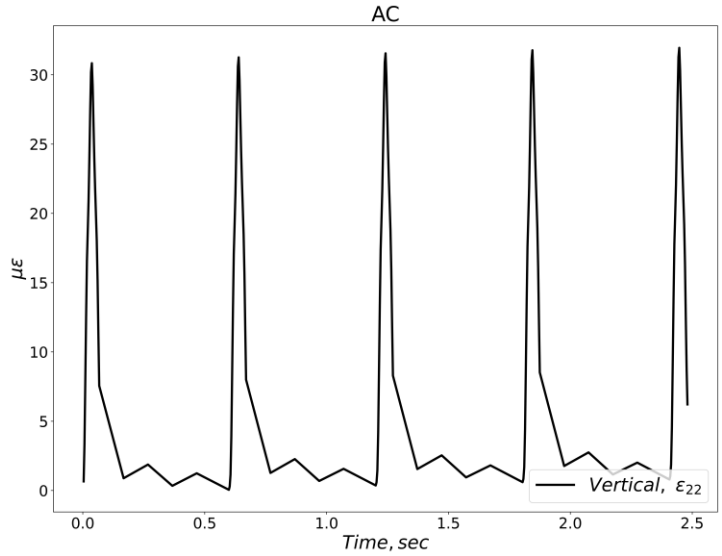

A. 68°F (reference case, linear viscoelastic AC).

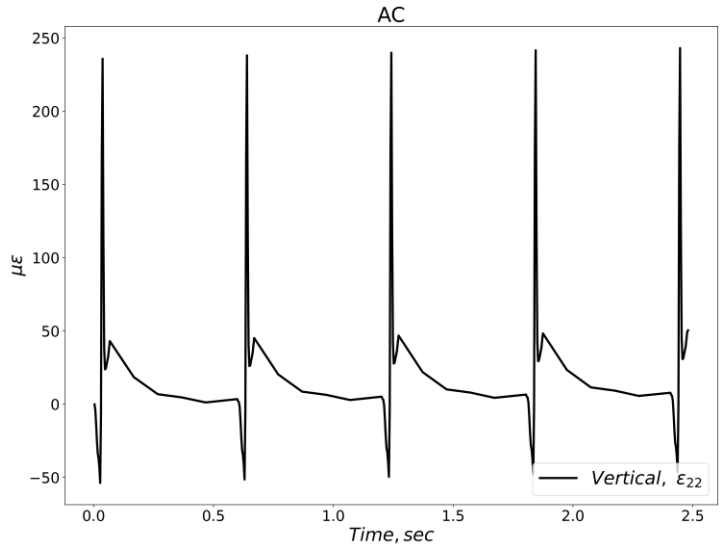

B. 104°F (Burger's model AC).

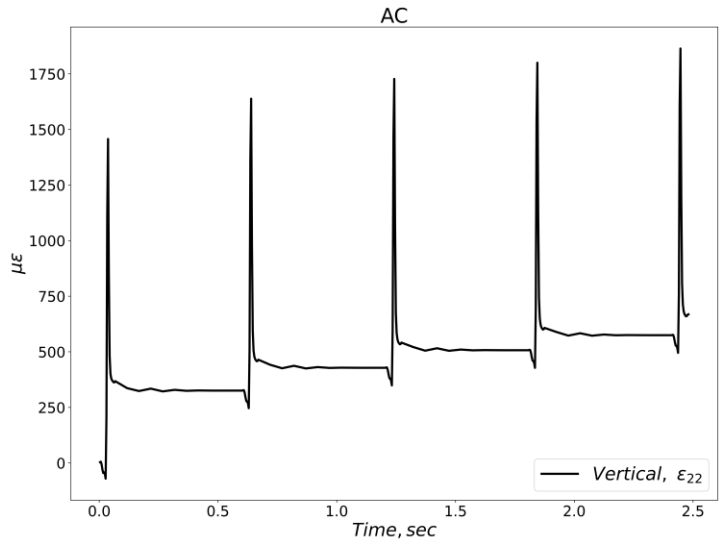

C. 130°F (Burger's model AC).

Figure 80. Plots. Compressive/permanent strains per load cycle for the thick-pavement section at 40 mph with 0.57-sec rest period.

AC Rutting

Rutting can be approximated by multiplying the permanent strain with the thickness of the sublayer (in line the MEPDG approach) or, in this case, per a finite element. The rut across the AC depth during the last cycle for a thick section is illustrated in Figure 81 via contour plots for varying rest periods, speeds, and temperatures. For brevity, the contour images for other sections are not presented, as they exhibited similar trends. The pattern was mainly dependent on the pavement configuration (thin versus thick) for a given loading and pavement temperature (Figure 82). As would be expected, rutting was found to be relatively high within regions directly underneath the loading (encased by the

two vertical dashed lines), as compared to the neighboring regions. The results were similar to rutting observed in the roadways, where severe rut is observed underneath traffic wheel path.

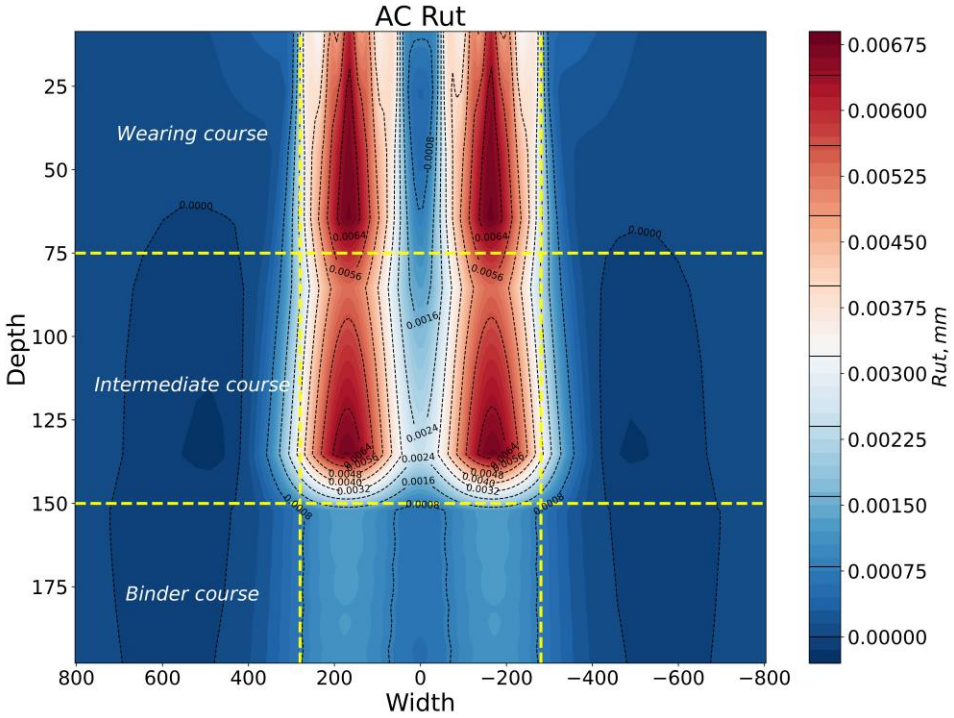

A. Thick section under 40 mph, 0.57-sec rest period, and 104°F.

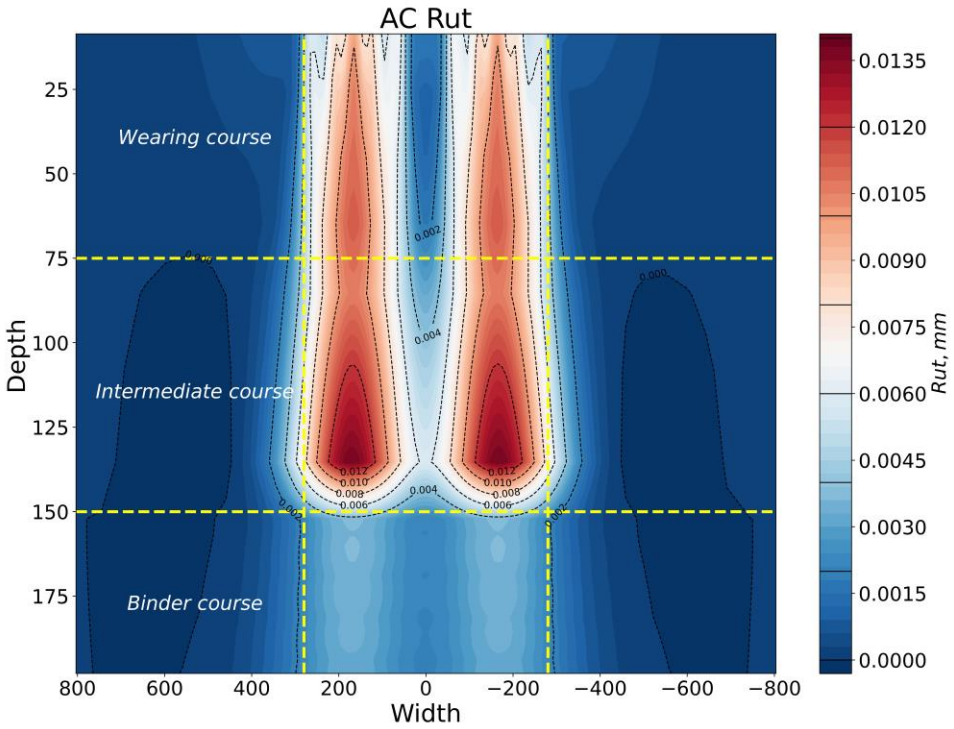

B. Thick section under 40 mph, 0.57-sec rest period, and 130°F.

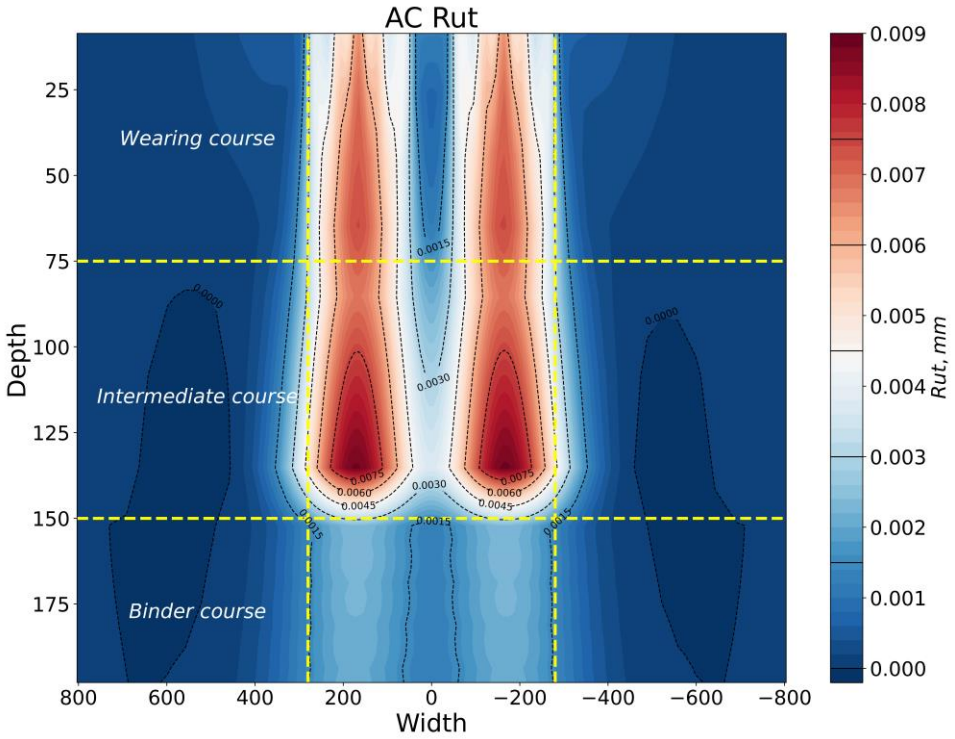

C. Thick section under 70 mph, 0.57-sec rest period, and 130°F.

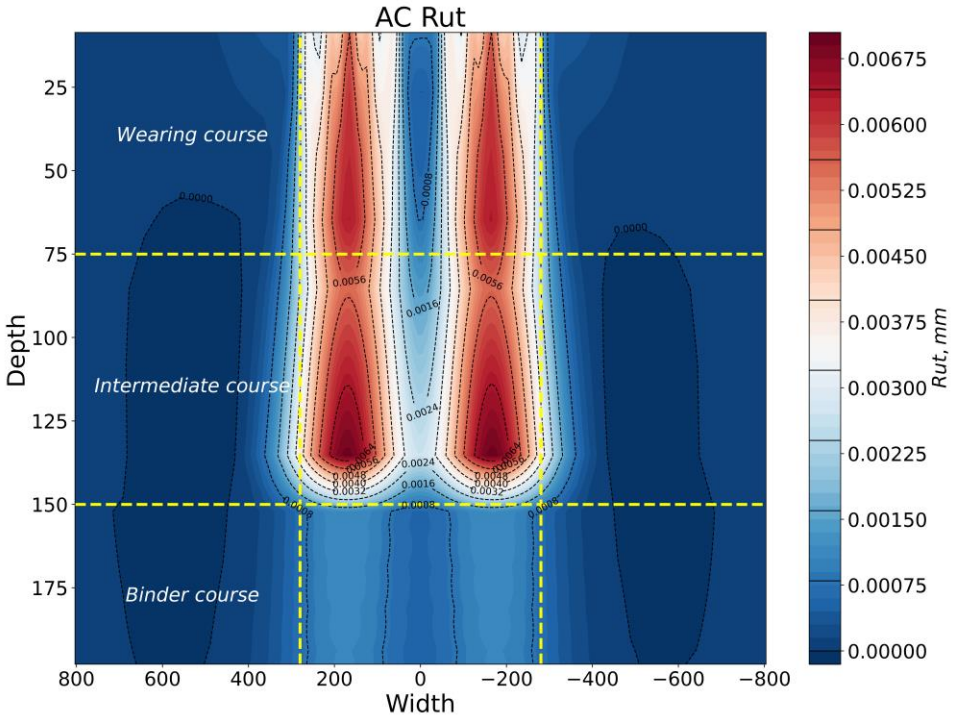

D. Thick section under 70 mph, 2.50-sec rest period, and 104°F.

Figure 81. Graph. Rut contour across the cross section of AC layer (1 mm = 0.039 in.).

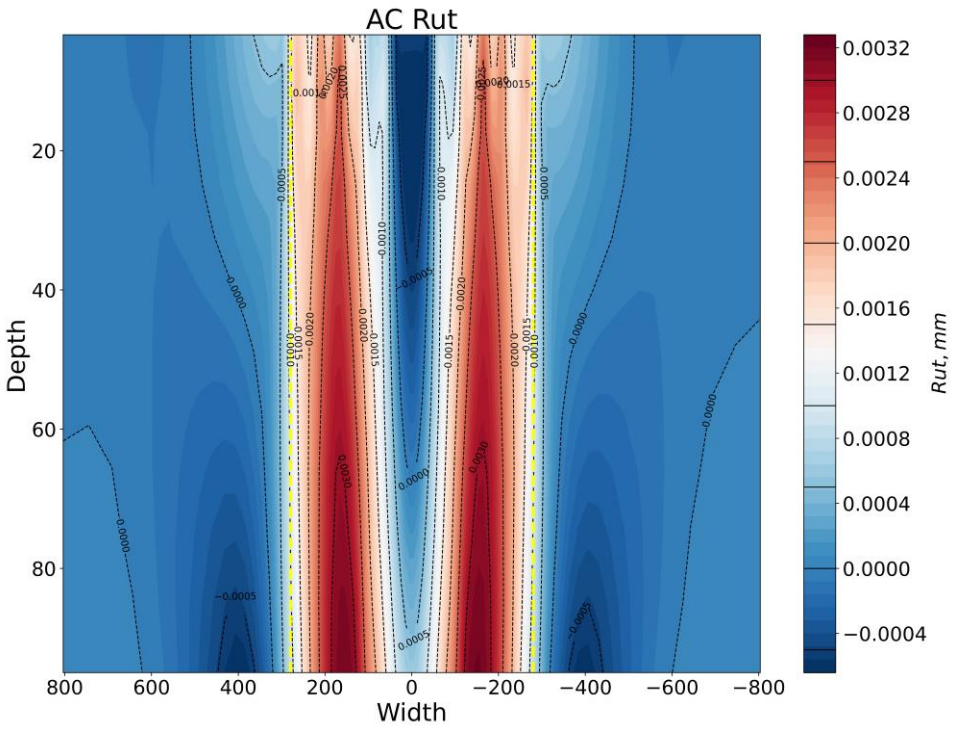

Figure 82. Plots. Rut contour for the thin-pavement section under 40 mph, 0.57-sec rest period, and 104°F.

SUMMARY

The pavement FE model, developed by Al-Qadi and colleagues over the past three decades, has the capability to emulate realistic loaded-pavement conditions, tire-loading complexity, accurate material property, temperature profile, and layer interaction. However, the conventional model has mainly focused on a single-tire-load pass, which typically required a wheel path length that appropriately captures the history of a full moving load. Moreover, the assumed tire-contact stresses have been loaded in steady state.

To implement cyclic loading, the load-pass approach (LPA) was developed. It accounted for a transient moving load as the load entered and exited the analysis domain—emulating having a viewing window as a truck-tire load would pass. Motivated by reducing the 3D domain and the corresponding computational cost, the proposed LPA included partial entrance and exit schemes that applied transient loading. Additionally, an appropriate wheel path length was selected to allow moving the full-load imprint for a given length, prior to the exit scheme. Considering the reduced wheel path length (in contrast to the conventional moving-load approach), the required distance associated with the full duration of the rest period became much longer. Instead, the numerical implementation included time/distance after the load has "unloaded" the area of interest to simulate the rest period. A residual time from the total rest period was then managed by including load steps with no tire loading (allowing the AC layer(s) to recover). After the total rest period was completed, the next axle load was immediately introduced via partial entrance, moving the full tire load after manifesting, and then partial exit. The same load/unload cycle was continued until the selected

number of load cycles was reached. By adopting the LPA, the FE pavement model's ability to simulate full-axle tandem/tridem configurations was enhanced, enabling reasonable runtime without compromising model accuracy. Accuracy was verified by comparing responses with the conventional moving load for one cycle, along with the sensitivity analysis of wheel path length and comparison with AC material consideration.

The Burger's model, validated in Chapter 2, was implemented in place of a linear viscoelastic model for the AC to obtain permanent deformation. A set of 24 cases was run using a combined LPA and Burger's model. An additional 12 cases, using the conventional linear viscoelastic model, were appended. Critical strains in the pavement model were obtained, and the values were logical and consistent with the inputs. The transverse tensile strain was found to be more critical than the longitudinal tensile strain, due to the accumulation of responses. The combined model (using Burger's and LPA) demonstrated the ability to capture accumulated rutting in AC layers. The rut distribution across the AC layer depends mainly on pavement configuration and temperature. The magnitude of rut depth was greater when the rest period is higher, reflecting the experimental data. During the rest period, compressive strain stabilizes to permanent deformation after recovering elastic and viscoelastic strains. The progression of deformation was found to be similar to that of conventional pavement-rut progression.

CHAPTER 4: GRAPH NEURAL NETWORK

INTRODUCTION

On average, the pavement FE model simulation using the LPA and Burger's model is completed within 50 hr via a supercomputer with 40 cores. In lieu of running the FE model for an extensive factorial of parameters, the simulation matrix was strategically selected as training/testing data for a machine learning (ML) model—used in tandem with FE simulations. ML, with its nonlinear, highly parallel, and fault-tolerant learning and generalization capabilities, has been a promising and widely applied solution in engineering. The requirements of ML are twofold: a good dataset to train and test, and an appropriate model for the needs of the problem. In the past decade, over 900 FE pavement models comprising different pavement configurations, speed, temperature, tire type, and load were simulated, postprocessed, and analyzed by the Illinois Center for Transporation (ICT). This database serves as a robust dataset to train the ML model. Different ML models such as nonlinear regression, multi-layer perceptron (MLP), and Bayesian neural network were trained and implemented to predict maximum-point responses (stresses, strains, and deflections) for a loaded-pavement problem. However, those models were unable to recognize the spatiotemporal complexity of the actual 3D pavement model.

Recently, graph neural network (GNN) has been proposed to predict time-series data while considering spatiotemporal interactions. GNN has been shown to achieve satisfactory performance in spatiotemporal modeling and prediction. For example, Sanchez-Gonzalez et al. (2020) developed a GNN-based framework to model the state of a physical system, using particles as nodes in a graph and calculate dynamics (displacement, velocity, and acceleration), while including thousands of particles and time steps. Similarly, Pfaff et al. (2021) proposed a GNN-based framework to learn mesh-based simulations, including aerodynamics, structural mechanics, and cloth, as their proposed GNN models could learn to pass messages on a mesh graph and adjust the mesh discretization during forward simulation. In addition, Li et al. (2019, 2020) developed a deep-graph convolutional network (GCN), namely DeepGCN, by borrowing concepts from the convolutional neural network (CNN) for the large-scale graph-learning tasks of node-property prediction (e.g., predicting the presence of protein functions) and graph-property prediction (e.g., predicting the target molecular properties). Besides, Li and Zhu (Li and Zhu 2021) proposed a spatiotemporal fusion graph neural network (STFGNN) for spatiotemporal data forecasting of traffic flow, while taking into account various spatial and temporal graphs. The aforementioned examples illustrate that GNN could be used as an accurate and robust alternative for pavement-response modeling.

METHODOLOGY

Graph

For GNN, a graph shows relationships between several representations, defined as a 3-tuple $G = (\mathbf{u}, V, E)$ (Battaglia et al. 2018; Sanchez-Lengeling et al. 2021). The $\mathbf{u}$ is a global feature. The $V = \{\mathbf{v}_i\}_{i=1:N^v}$ is the sets of node (or vertexes) features where there is a total of N^v nodes, and each $\mathbf{v}_i$ is

a node's feature. The $E = \{(\mathbf{e}_k, r_k, s_k)\}_{k=1:N^e}$ is set of edge features, where there is a total of N^e edges, each $\mathbf{e}_k$ is an edge's feature, r_k is index of receiver nodes, and s_k is index of sending nodes.

Before training and evaluating GNN models, the 3D pavement FE data were reconstructed into a graph. The nodes of 3D pavement FE models were constructed as the nodes of a graph. The node connections of 3D pavement FE models would be constructed as the edges of a graph. Correspondingly, the 3D pavement FE data would be considered as the node and edge features, which are summarized in Table 10.

Input node features

i. X, Y, and Z coordinates (3 features): The X, Y, and Z coordinates of nodes, namely nodes of 3D pavement FE models.
ii. Pavement-layer type (1 feature): The layer type of pavement structure, namely, AC layer (0), base layer (1), subbase layer (2), and subgrade layer (3). All AC sublayers would be represented as the AC layer for the layer type.
iii. Temperature (1 feature): The temperature of 3D pavement FE models.
iv. Material (11 features): The material property of 3D pavement FE models. It includes AC instantaneous modulus, AC sigmoidal function parameters (α, β, γ, and γ), base modulus, base-material type (0 is linear and 1 is stress-dependent), subbase modulus, subbase material type (0 is linear and 1 is stress-dependent), subgrade modulus, and subgrade material type (0 is linear and 1 is stress-dependent).
v. Loading profiles (3 features): The 3D contact-stress force of 3D pavement FE models and is applied only to the model surface.
vi. Loading time (1 feature): The accumulated loading time.
vii. Previous pavement responses (displacement, stress, strain) (15 features): The pavement responses (displacement, stress, strain) at one previous time step. They include the displacement U_1, U_2, U_3; stress S_{11}, S_{22}, S_{33}, S_{12}, S_{13}, S_{23}; and strain E_{11}, E_{22}, E_{33}, E_{12}, E_{13}, and E_{23}.

Input edge features

i. Relative distance (1 feature). This is the relative distance of each edge, namely the FE edge of 3D pavement FE models.
ii. Relative pavement responses (displacement, stress, strain) (3 features). They are the relative pavement responses of two connected nodes of each edge. $Disp_{rel}$ is the relative displacement, $Stress_{rel}$ is the relative stress, and $Strain_{rel}$ is the relative strain.

Output node features

i. Target pavement responses (displacement, stress, strain) (11 features). The pavement responses at the target time step or the next time step would be the final model output.

Table 10. Summary of Node and Edge Features

Graph		Features
Input	Node	• X, Y, and Z coordinates (3 features) • Pavement-layer type (1 feature) • Temperature (1 feature) • Material (13 features) • Loading profiles (3 features) • Loading time (1 feature) • Previous pavement responses (displacement, stress, strain) (15 features)
	Edge	• Relative distance (1 feature) • Relative pavement responses (displacement, stress, strain) (3 features)
Output	Node	• Target pavement responses (displacement, stress, strain) (15 features)

Graph Neural Network

The GNN is a transformation that optimizes all attributes of a graph (nodes, edges, and global context) while maintaining graph symmetries (permutation invariances) (Sanchez-Lengeling et al. 2021). GNNs utilize a "graph-in, graph-out" architecture, which means they take a graph as input—complete with data embedded in its nodes, edges, and global context—and progressively refine these embeddings without altering the original graph's connectivity (Sanchez-Lengeling et al. 2021). To model 3D pavement responses, a GNN-based pavement simulator (GPS) is proposed, as shown in Figure 83. It is based on the work by (Pfaff et al. 2021; Sanchez-Gonzalez et al. 2020). GPS includes three main components: encoder, processor, and decoder.

The encoder embeds the 3D pavement FE model as a latent graph. The node embeddings are learned functions of the node features of 3D pavement FE model (Table 10). The edge embedding is learned functions of the edge features 3D pavement FE model (Table 10). In this work, the encoder employs the multilayer perceptrons (MLP) to encode node features and edge features into latent vectors with the size of 128.

The processor calculates interactions among nodes and edges through a sequence of learned layers to produce a series of updated latent graphs. It would pass, aggregate, and update messages between nodes and their connected nodes and edges. It outputs the final graph, which would be used as the input of the decoder. It uses a graph network (GN) as the processor. GN consists of a sequence of GN layers. Each GN layer includes three separate "update" functions (ϕ) and three associated "aggregation" functions (ρ).

Edge updates are performed using the ϕ^e function across all edges, and node updates utilize the ϕ^v function across all nodes. In contrast, the ϕ^u function provides a global update and is applied once. The ϕ function may be implemented as a neural network, such as an MLP. As for the ρ function, it processes sets of inputs, effectively consolidating them into a single output that reflects aggregated information. Importantly, these ρ functions are invariant to permutations of their inputs and can adapt to varying input sizes. Possible implementations of the ρ function include operations like elementwise summation, averaging, or taking the maximum. In this study, the global block was not

used, as there were no global features (Table 10). Ten GN layers were used, and each GN layer had both the input and output size of 128. The ϕ^e and ϕ^v functions were a two-layer MLP with an input and output size of 128. The $\rho^{e\to v}$ function was the elementwise summation.

The decoder retrieves dynamic information (i.e., pavement responses in this study) from the nodes of the final latent graph. In this study, the decoder employed the multilayer perceptrons (MLP) to decode latent vectors with the size of 128 into the pavement responses of the 3D pavement FE model.

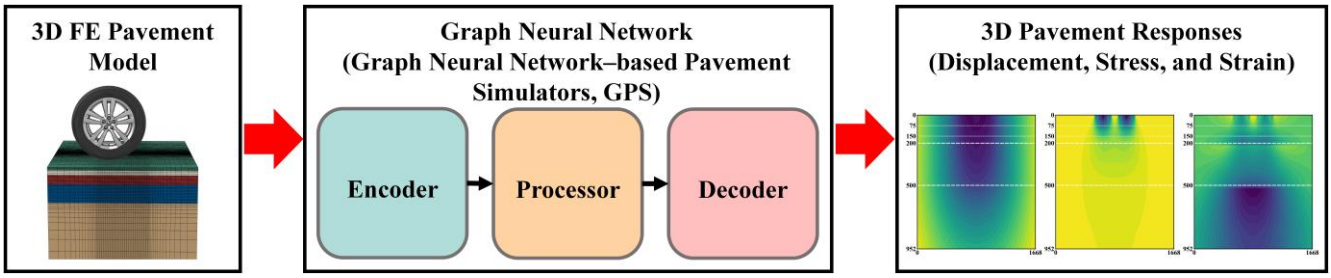

Figure 83. Plot. The framework of graph neural network–based pavement simulator (GPS), including encoder, processor, and decoder.

3D FEM PAVEMENT-DATABASE DEVELOPMENT

Based on the FE model developed, this study built a pavement 3D FE model database. The data have 36 FE cases, including 12 cases with thick pavements and 24 cases with thin pavements (Table 3). Table 11 summarizes the statistical metrics of the pavement responses of the 3D FE pavement database. These responses varied significantly in different ranges. The displacement and stress varied in a similar range, which was much larger than the strain. Among all strain values, E and EP also showed differences. In addition, FE model cases had different time steps because different speeds and rest periods were used in the FE models. As shown in Figure 69-Figure 71, the LPA approach has 6 loading-entrance time steps, 9 full-loading time steps, and 6 loading-exit time steps, while there are varied time steps for the rest period. For consistency, each FE model case selected 10 time steps from the first loading cycle to build the database. It means each FE model case selected 9 full-loading time steps and 1 time step from the rest period (i.e., the last time step of the rest period). Therefore, this database had a total of 360 data points.

The database was divided into three subsets to train and evaluate the GNN models: training (70%), validation (10%), and test sets (20%). The training set was used to develop the model, while the validation set helped select the optimal version during training. The final test set served to evaluate the model's performance. Both thin- and thick-pavement cases were distributed proportionally across these subsets. The training set contained 26 FEM cases (17 thin pavement and 9 thick pavement) with 260 data points. The validation set included 3 FEM cases (2 thin pavement and 1 thick pavement) with 30 data points. The test set comprised 7 FE model cases (5 thin pavement and 2 thick pavement) with 70 data points.

To reduce the effect of different ranges of pavement responses on training GNN models, all pavement responses were normalized with their corresponding mean values and standard deviations.

Table 11. Summary of the Pavement Responses of 3D FEM Pavement Database

	Displacement (mm)			Stress (MPa)						Strain (με)					
	U1	U2	U3	S11	S22	S33	S12	S13	S23	E11	E22	E33	E12	E13	E23
Min	0.701	-0.016	0.182	3.401	0.060	2.686	0.378	0.455	0.421	2314	697	1308	5001	3073	2989
Max	-0.454	-2.016	-0.208	-3.362	-0.858	-2.759	-0.418	-0.457	-0.426	-2562	-4531	-1579	-1885	-3071	-3035
Mean	-0.001	-0.512	-0.002	-0.002	-0.028	-0.002	-0.002	-2e-6	-7e-5	47	-350	39	120	1	-1
Std	0.071	0.311	0.033	0.234	0.057	0.204	0.039	0.040	0.025	195	565	139	446	154	323

Note: The subscripts “1”, “2”, and “3” refer to the longitudinal (X), vertical (Y), and transverse directions (Z), correspondingly. Max is the maximal value, Min is the minimal value, Mean is the mean value, and Std is the standard deviation value.

RESULTS AND DISCUSSION

Two case studies— OneStep and Rollout—were used to evaluate the performance of the proposed GPS model. In the OneStep case, the proposed GPS model used the ground-truth data as input. This means the input would include all node features and edge features from the ground-truth data, and the output would be the pavement responses of the target time step (i.e., the next time step). This is also the training procedure. In comparison, in the Rollout case study, the proposed GPS model would predict the pavement responses at the target time step based on its own predicted pavement responses at the previous time step, except for the first time step. As presented in Table 10, the input would use the predicted pavement responses at the previous time step as the previous pavement responses. The Rollout case is similar to the FE model simulation, which predicts the pavement responses of all time steps after given loading profiles. Because error could accumulate over time in the Rollout case, the prediction error in the Rollout case would be higher than in the One-Step case.

As presented in Figure 84, the MSE of the GPS model for all pavement responses was greater in the Rollout case than in the OneStep case. The MSE of stress and strain was over 10 times higher in the Rollout case than in the OneStep case, while the MSE of displacement was over 6 times greater. This is because the GPS model would use its own predicted pavement responses as inputs across all time steps except for the first time step in the Rollout case, while the GPS model would use ground-truth pavement responses as inputs in the OneStep case.

Compared to the OneStep case, the prediction error would accumulate as the time step increases, as presented in Figure 85. In the first few time steps, the GPS models had similar MSE in the OneStep and Rollout cases. However, as the time step increased, the MSE for the Rollout case significantly and rapidly increased; but it remained at a low value for the OneStep case. This resulted in the GPS model having a much higher MSE in the Rollout case study than in the OneStep case study.

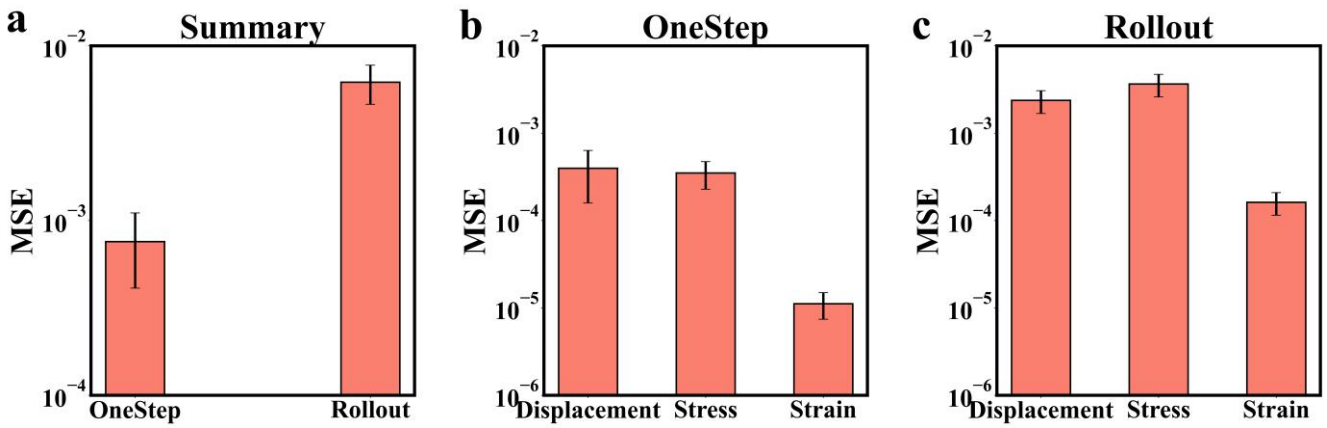

Figure 84. Plots. MSE of GPS model: (a) the summary, (b) the MSE of the OneStep case study, and (c) the MSE of the Rollout case study.

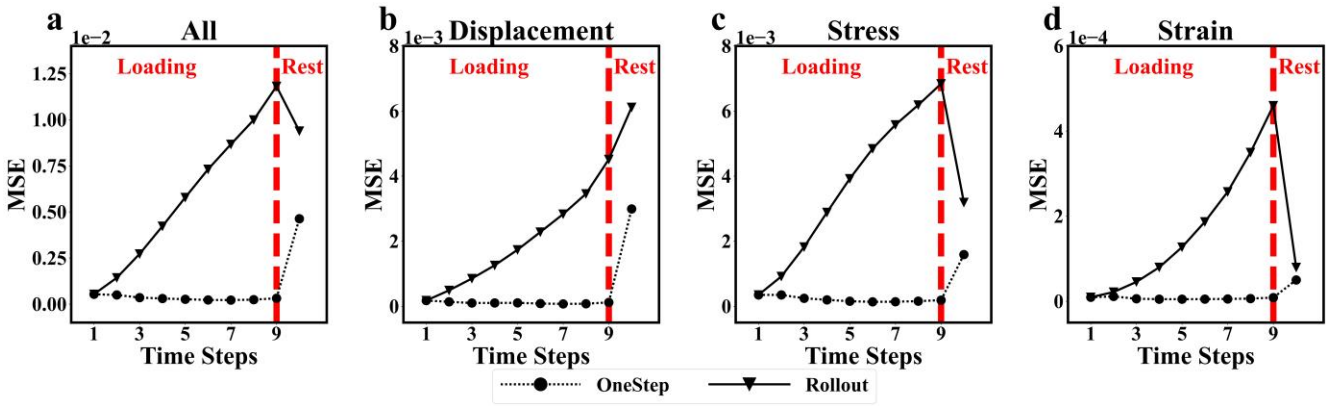

Figure 85. Plots. MSE of the GPS model across all time steps of FEM cases: (a) the summary, (b) displacement, (c) stress, and (d) strain.

In addition to MSE, the pavement-response prediction was used to evaluate model performance. As presented in Figure 86, the GPS model demonstrated excellent prediction accuracy across all time steps in the OneStep case study, with results closely matching the ground-truth data (i.e., FE model results). Although predictions for the Rollout case study showed slightly lower accuracy, they remained satisfactory. The GPS model successfully captured trends across all pavement responses. For strains E11 and E33, prediction error increased during the loading period but decreased during the rest period (TimeStep 10). A similar pattern emerged in displacement U2. Strain E22 showed increasing prediction error over time before stabilizing below peak levels in the final time steps. Strain E23 predictions matched the reference data closely for the first seven time steps before showing significant deviation. Notably, stress S22 predictions maintained high accuracy throughout all periods.

Pavement-response predictions were also presented through figures in different planes. Figure 87–Figure 92 show pavement-response predictions in the YZ plane, including E11, E22, E33, E23, U2, and S22, respectively. The results reveal distinct performance patterns between the OneStep and Rollout

case studies. In the OneStep study, the GPS model achieved high accuracy with minimal prediction errors across all pavement responses. The Rollout study, however, showed variable performance across different response types. Strain predictions (E11, E22, E33, and E23) maintained high accuracy in both cases. However, stress (S22) and displacement (U2) predictions showed reduced accuracy in the Rollout case, while maintaining high precision in the OneStep case. Additional analysis of strain E22 in the XY and XZ planes (Figure 93 and Figure 94, respectively) revealed similar patterns. The model maintained accurate predictions in the XY plane for both cases but showed decreased accuracy in the XZ plane for the Rollout study, while maintaining precision in the OneStep case.

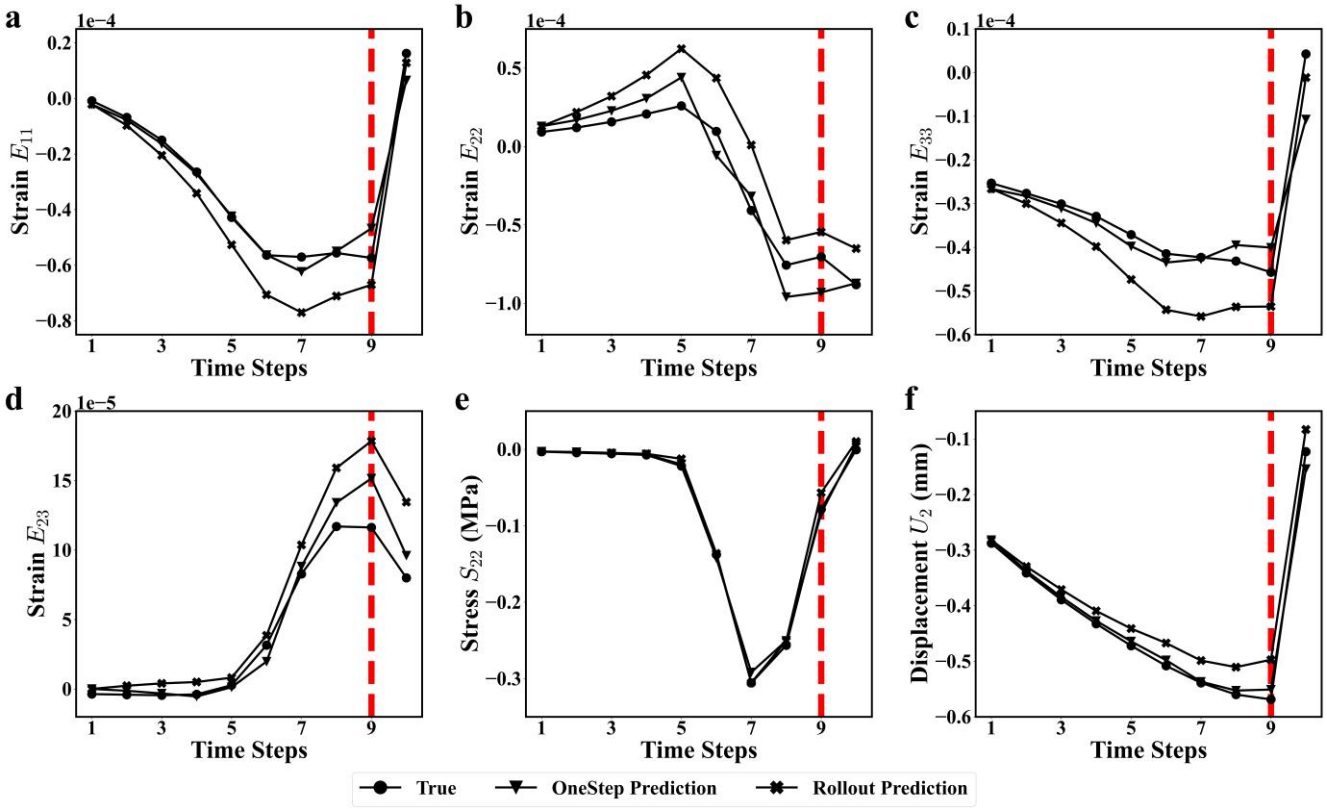

Figure 86. Plots. Pavement-response predictions across all time steps: (a) E11, (b) E22, (c) E33, (d) E23, (e) S22, and (f) U2. The position was obtained based on the maximal absolute value E22 of the middle section of the wheel path.

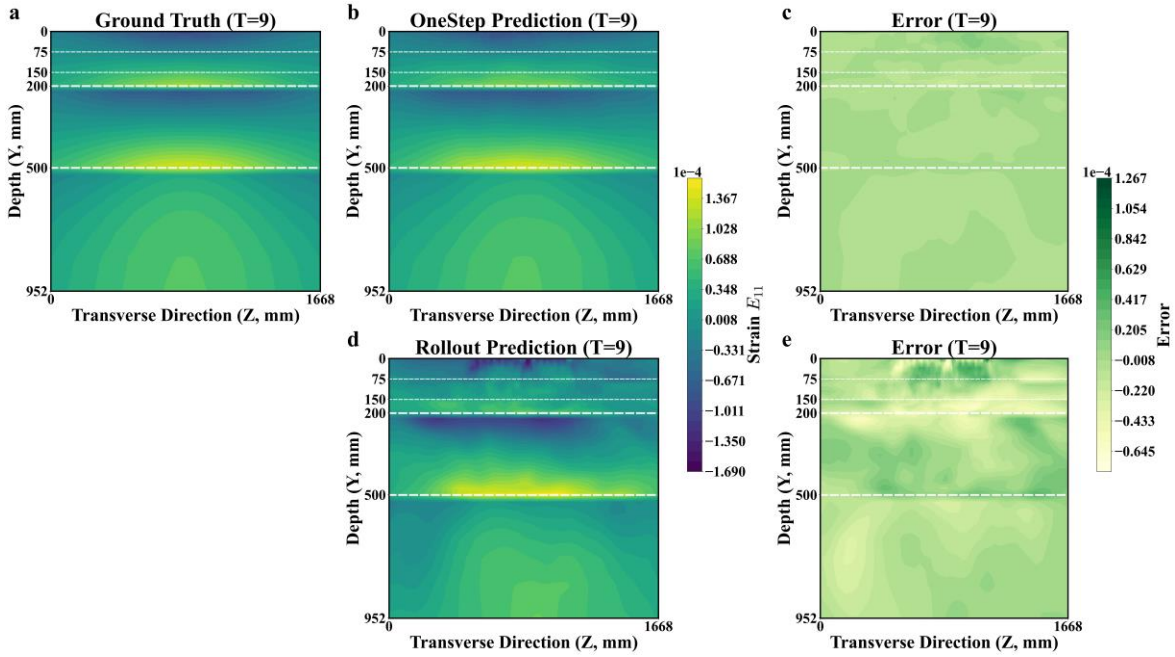

Figure 87. Plots. Pavement-response (E11) prediction in the YZ plane for TimeStep 9: (a) for ground truth; (b) and (c) for model predictions and prediction errors in the OneStep case study, respectively; (d) and (e) for model predictions and prediction errors in the Rollout case study, respectively.

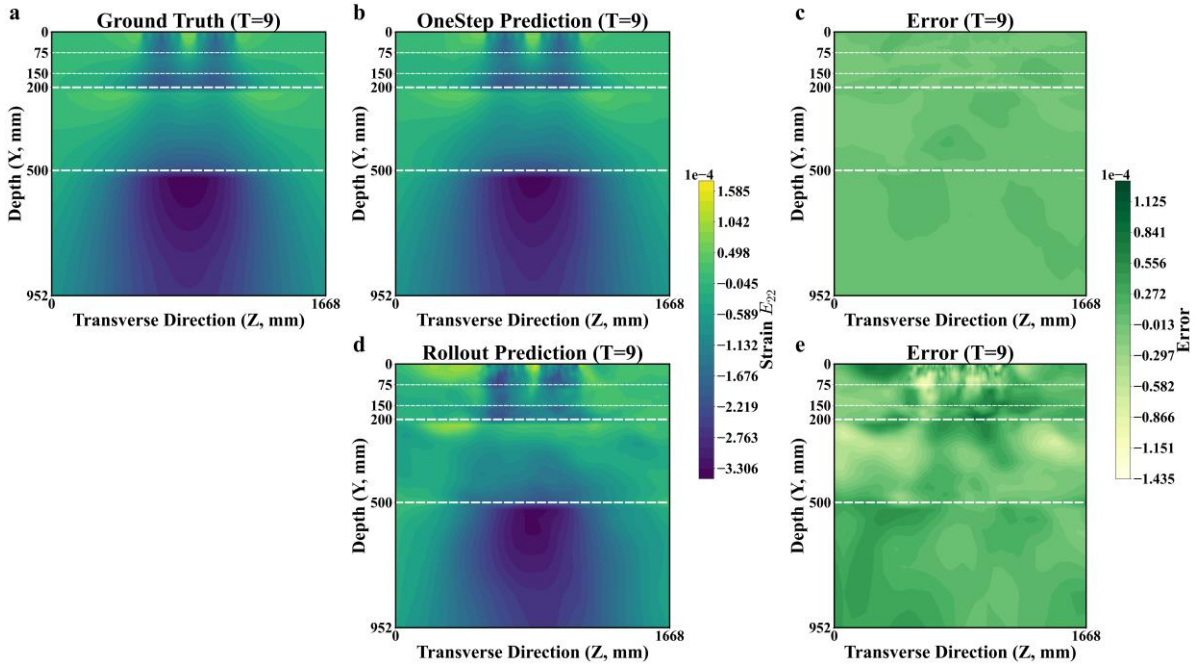

Figure 88. Plots. Pavement-response (E22) prediction in the YZ plane for TimeStep 9: (a) for ground truth; (b) and (c) for model predictions and prediction errors in the OneStep case study, respectively; (d) and (e) for model predictions and prediction errors in the Rollout case study, respectively.

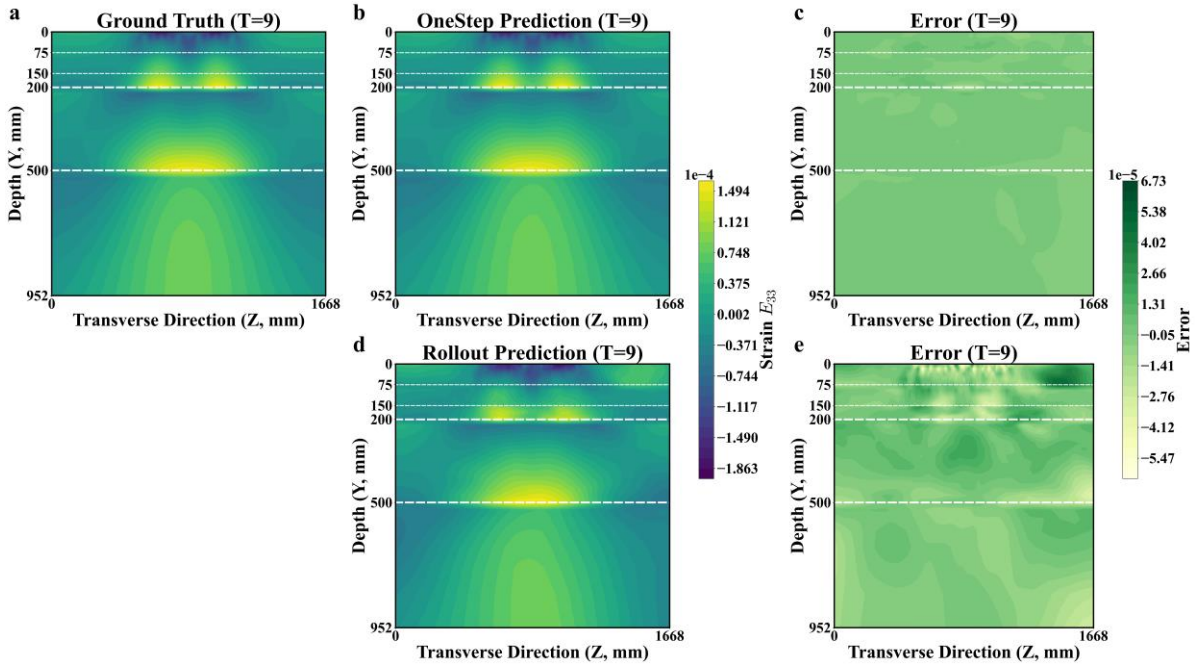

Figure 89. Plots. Pavement-response (E33) prediction in the YZ plane for TimeStep 9: (a) for ground truth; (b) and (c) for model predictions and prediction errors in the OneStep case study, respectively; (d) and (e) for model predictions and prediction errors in the Rollout case study, respectively.

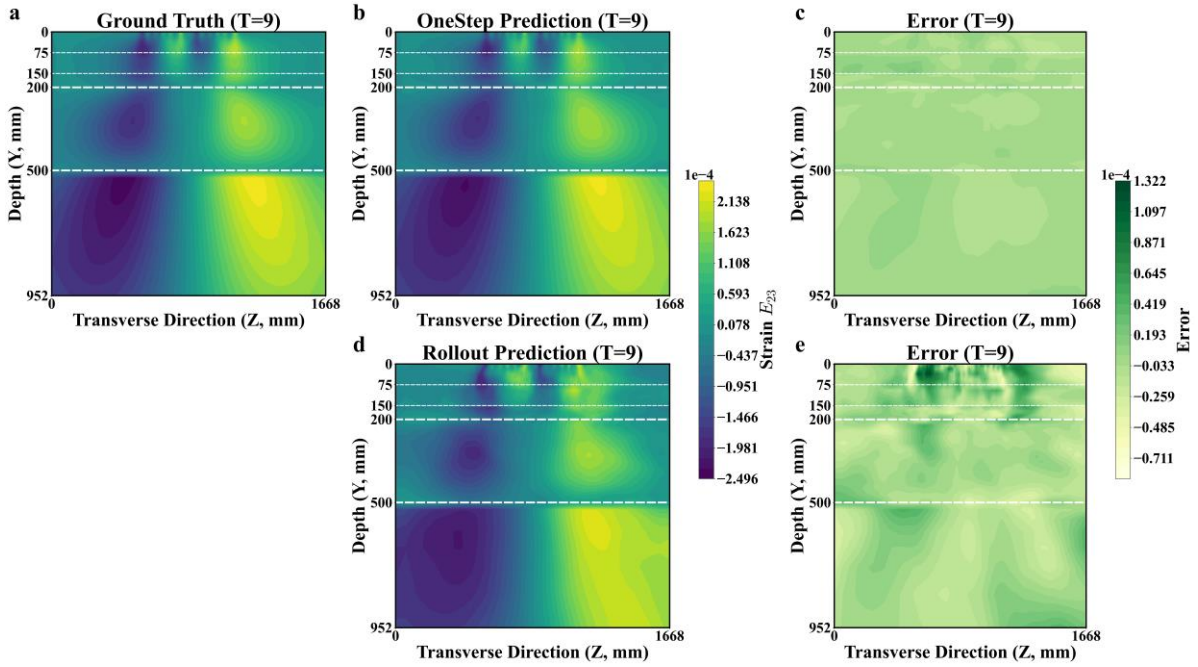

Figure 90. Plots. Pavement-response (E23) prediction in the YZ plane for TimeStep 9: (a) for ground truth; (b) and (c) for model predictions and prediction errors in the OneStep case study, respectively; (d) and (e) for model predictions and prediction errors in the Rollout case study, respectively.

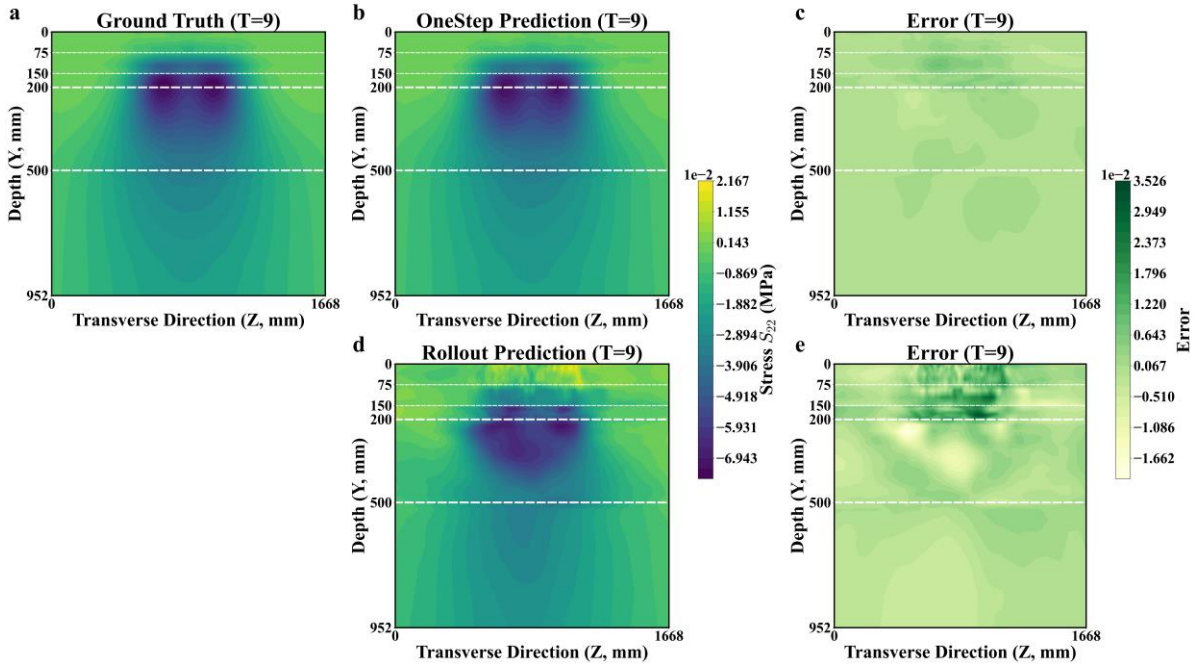

Figure 91. Plots. Pavement-response (S22) prediction in the YZ plane for TimeStep 9: (a) for ground truth; (b) and (c) for model predictions and prediction errors in the OneStep case study, respectively; (d) and (e) for model predictions and prediction errors in the Rollout case study, respectively.

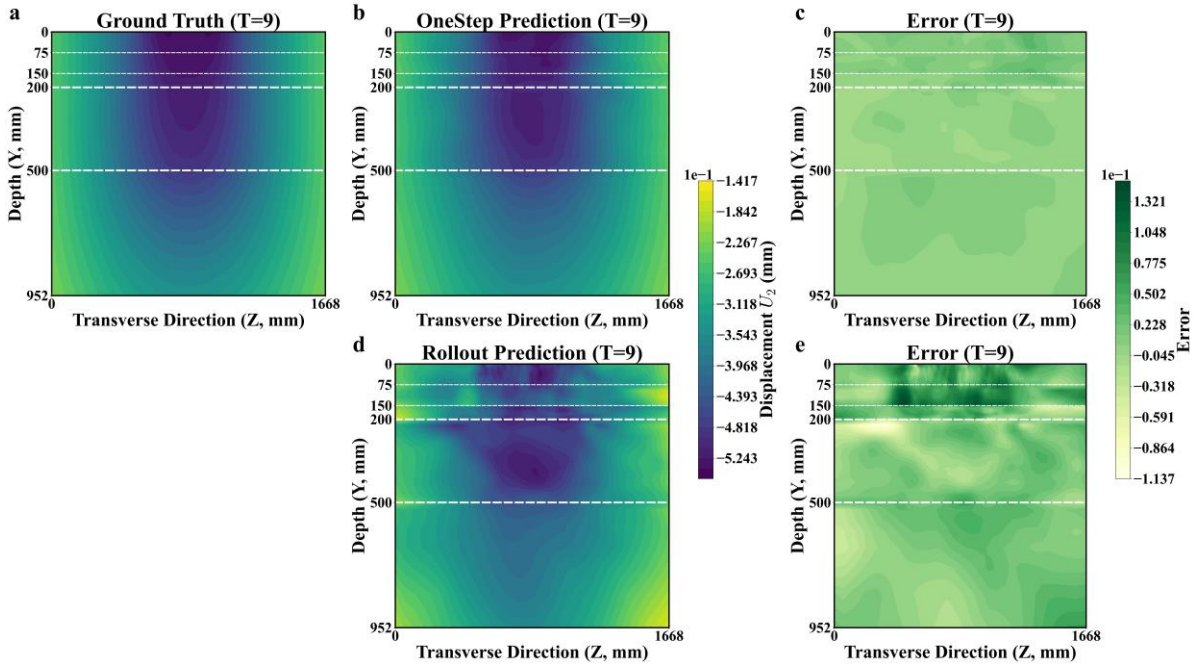

Figure 92. Plots. Pavement-response (U2) prediction in the YZ plane for TimeStep 9: (a) for ground truth; (b) and (c) for model predictions and prediction errors in the OneStep case study, respectively; (d) and (e) for model predictions and prediction errors in the Rollout case study, respectively.

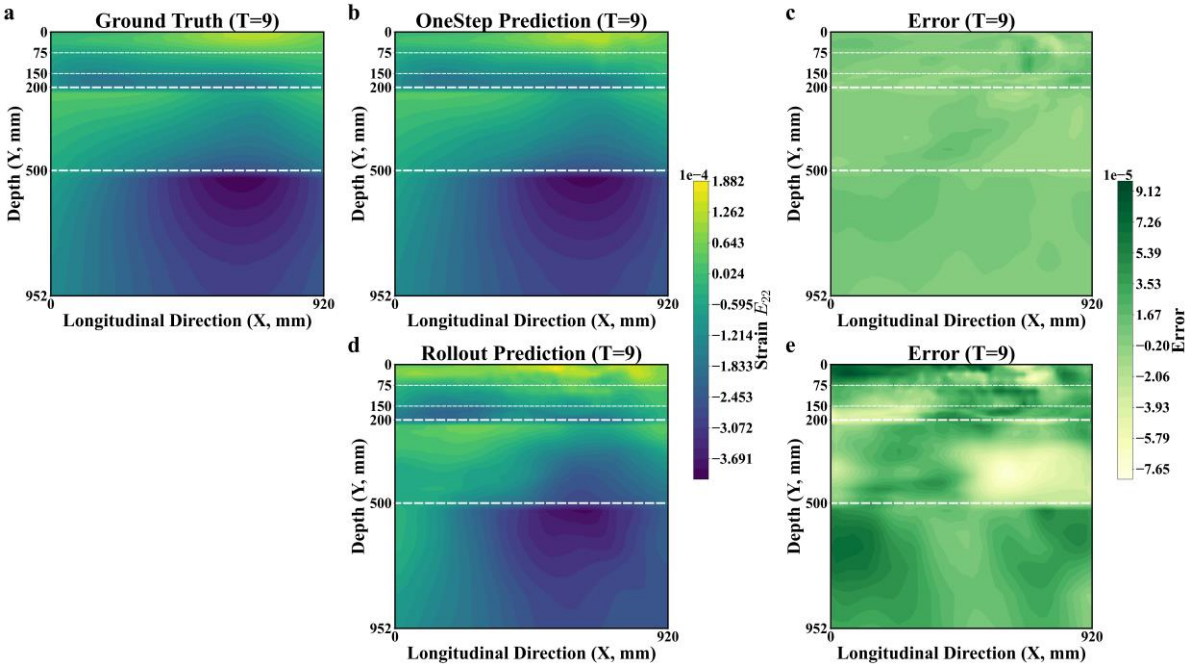

Figure 93. Plots. Pavement-response (E22) prediction in the XY plane for TimeStep 9: (a) for ground truth; (b) and (c) for model predictions and prediction errors in the OneStep case study, respectively; (d) and (e) for model predictions and prediction errors in the Rollout case study, respectively.

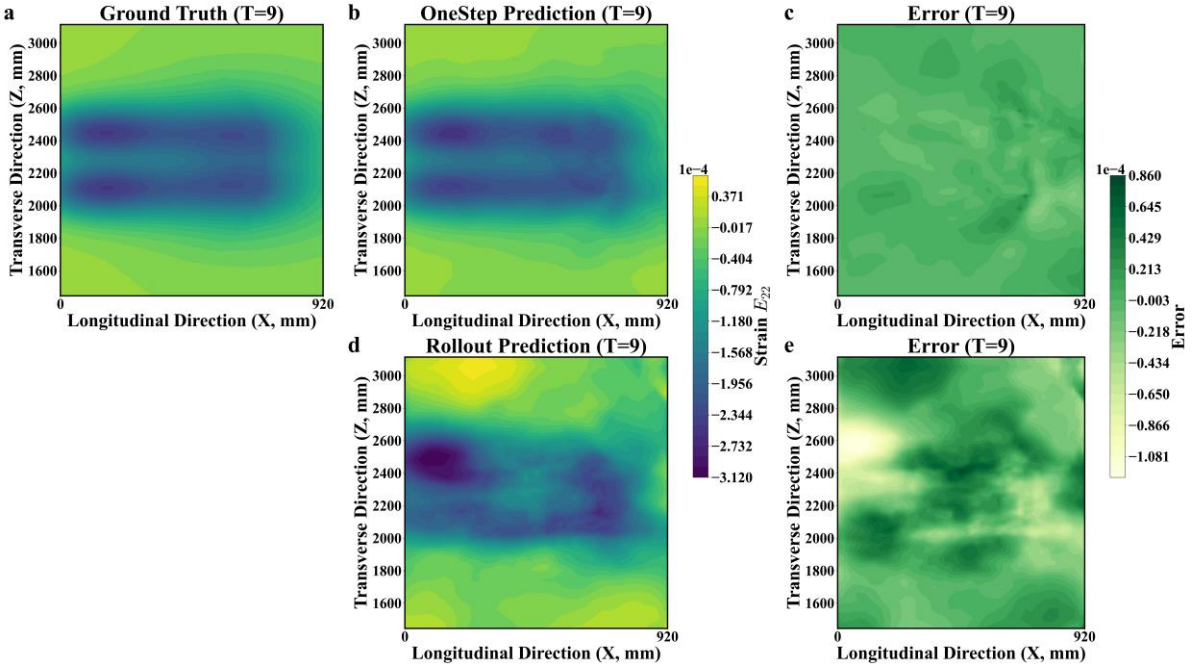

Figure 94. Plots. Pavement-response (E22) prediction in the XZ plane for TimeStep 9: (a) for ground truth; (b) and (c) for model predictions and prediction errors in the OneStep case study, respectively; (d) and (e) for model predictions and prediction errors in the Rollout case study, respectively.

SUMMARY

This chapter proposed a genetic neural network (GNN)–based framework for 3D asphalt concrete (AC) pavement-response modeling. Based on the 3D pavement finite element (FE) model developed in this study, the 3D FEM pavement database was built with 36 FE model-simulation cases, including different pavement structures, material properties, temperatures, speeds, and rest periods. The 3D pavement FE model data was reconstructed into a graph by constructing the nodes and node connections of 3D pavement FE models as the nodes and edges of a graph, respectively. To better represent 3D pavement FE model data, input node features included node coordinates, pavement layer type, temperature, material properties, 3D loading profiles, loading time, and previous pavement responses (displacement, stress, strain). The input edge features included relative distance and relative pavement responses. The output node features were target pavement responses. To model 3D pavement responses, a GNN-based pavement simulator (GPS) was developed, including three main components: encoder, processor, and decoder. The encoder and decoder employed the two-layer multilayer perceptrons (MLP), and the processor used the graph network (GN). In addition, two case studies were developed to evaluate the performances of the proposed GPS model in predicting 3D pavement responses, including OneStep and Rollout. These two case studies were used to represent different test conditions, with the Rollout case being similar to the FE model simulation. The results showed that the proposed GPS model achieved satisfying accuracy in both case studies, with higher errors in the Rollout case study than in the OneStep case study. Therefore, the proposed GPS model could be an accurate and computationally efficient alternative to predict 3D pavement responses. In the future, the proposed GPS model will be trained with the 3D FE model pavement dataset with more loading cycles.

CHAPTER 5: SUMMARY AND CONCLUSIONS

This study details the combined use of finite element (FE) simulations and genetic neural network (GNN) to capture and quantify asphalt concrete (AC) pavement permanent deformation. Particularly, a generalized nonlinear Burger's model was proposed to simulate the permanent-deformation behavior of AC. The model utilizes a nonlinear power-law dashpot, which provides improved accuracy, as compared to the conventional dashpot with constant viscosity. The model is numerically formulated through an incremental approach to obtain the material response. The 1D formulation was extended to a 3D formulation. The model was then implemented in ABAQUS as a custom subroutine and verified through comparison with an analytical solution for creep loading using MATLAB. Model parameters were computed from the repeated-load permanent deformation and dynamic modulus tests. The model was successfully validated against experimental data and can predict permanent deformation up to the secondary region, demonstrating its effectiveness in simulating pavement rutting behavior. Moreover, a sensitivity analysis showed that the viscoelastic parameter $'b'$ in the Burger's model had a more significant impact on permanent strain at lower temperatures; and the deformation-rate parameter $'a'$ became more influential at higher temperatures. Additionally, $'a'$ was found to be exponentially dependent on rest periods; and $'b'$ had a linear dependence on both rest periods and stress levels.

In lieu of the conventional moving load, the study incorporated the new load-pass approach (LPA) to capture the transient effects of repetitive tire loading in a pavement FE model. One of the advantages of the LPA over the conventional moving-load method is the significant reduction in the required wheel path length in the longitudinal direction, directly leading to computational time savings—without adversely affecting the resulting responses. The proposed LPA-enabled cyclic loading is to be combined with the Burger's model constitutive relation in the AC layers to enable rut accumulation for a given number of passes. The approach also extends the capabilities of the research group's FE model to handle repetitive load-induced damage.

A GNN-based framework is proposed for 3D AC pavement-response modeling. The framework builds on a database of 36 FE model-simulation cases, which were transformed into a graph structure by converting the FE model's nodes and connections into corresponding graph nodes and edges. Node features included node coordinates, pavement-layer type, temperature, material properties, 3D loading profiles, loading time, and previous pavement responses (displacement, stress, strain). Edge features utilized relative distance and relative pavement responses, while output features represented the target pavement responses. To model 3D pavement responses, the GNN-based pavement simulator (GPS) was proposed, including three main components: encoder, processor, and decoder. The GPS model employed two-layer multilayer perceptrons (MLP) for the encoder and decoder, while utilizing graph network (GN) for the processor. Validation of the framework occurred through two case studies—OneStep and Rollout—with the latter closely replicating FE model–simulation conditions. Results demonstrated strong predictive accuracy across both scenarios, though the Rollout case exhibited higher errors, as compared to OneStep. These findings establish the GPS model as an accurate and computationally efficient alternative for predicting 3D pavement responses, given that an appropriate database is used.

PROJECT OUTPUTS, OUTCOMES, AND IMPACTS

The outputs, outcomes, and impacts of this study are summarized as follows:

OUTPUTS

- Presentation: Al-Qadi, I. L., and Liu, F. (2024). AI-driven Smart Asphalt Concrete Pavements. 2024 Data Science for Pavements Symposium, McLean, VA.

- Poster: Al-Qadi, I. L., Ramakrishnan., A., Jayme, A., and Fangyu Liu. (2024). Combined Mechanistic and Physics-Informed Modeling to Predict Pavement Damage due to Truck Platoons. 2024 CCAT Global Symposium, Ann Arbor, MI. 2024

OUTCOMES

- A generalized nonlinear Burger model was proposed to simulate the permanent deformation behavior of AC, which was implemented in Abaqus as a UMAT and verified against the analytical solution (using MATLAB) for a simple creep loading scenario.

- The “load pass approach” is introduced to impose cyclic loading on the FE pavement model.

- A graph neural network-based framework was proposed to model the 3D pavement responses and the permanent deformation of flexible pavements.

IMPACTS

- Rutting is a critical distress in flexible pavement. It is predicted using transfer functions. Transfer functions are empirical; hence, resulting in high variability. The proposed framework includes a mechanistic model combined with an artificial intelligence model to compute rutting without using transfer functions resulting in higher accuracy. It will significantly save computational time for investigating pavement damage induced by truck platoons. It helps simulate repetitive loading and predict accumulating pavement responses, including rut depth prediction.

REFERENCES

Ahmed, A., and S. Erlingsson. 2013. “Evaluation of permanent deformation models for unbound granular materials using accelerated pavement tests.” *Road Materials and Pavement Design*, 14 (1): 178–195. https://doi.org/10.1080/14680629.2012.755936.

Airey, G. D., B. Rahimzadeh, and A. C. Collop. 2003a. “Viscoelastic linearity limits for bituminous materials.” *Mat. Struct.*, 36 (10): 643–647. https://doi.org/10.1007/BF02479495.

Airey, G., B. Rahimzadeh, and A. Collop. 2003b. “Linear Viscoelastic Performance of Asphaltic Materials.” *Road Materials and Pavement Design*, 4 (3): 269–292. https://doi.org/10.1080/14680629.2003.9689949.

Alamnie, M. M., E. Taddesse, and I. Hoff. 2022. “Advances in Permanent Deformation Modeling of Asphalt Concrete—A Review.” *Materials*, 15 (10): 3480. https://doi.org/10.3390/ma15103480.

Al-Qadi, I., J. Hernandez, A. Jayme, M. Ziyadi, E. Gungor, S. Kang, J. Harvey, R. Wu, J. Greene, B. Choubane, M. De Beer, and T. Scarpas. 2021. *The Impact of Wide-Base Tires on Pavement—A National Study*. Illinois Center for Transportation.

Al-Qadi, I. L., and M. A. Elseifi. 2007. “New Generation of Wide-Base Tires: Impact on Trucking Operations, Environment, and Pavements.” *Transportation Research Record: Journal of the Transportation Research Board*, 2008 (1): 100–109. https://doi.org/10.3141/2008-13.

Al-Qadi, I. L., A. Loulizi, M. Elseifi, and S. Lahouar. 2004. “The Virginia smart road: The impact of pavement instrumentation on understanding pavement performance.” *Asphalt Paving Technology, AAPT*, 427–465. Association of Asphalt Paving Technologist.

Al-Qadi, I. L., H. Wang, P. J. Yoo, and S. H. Dessouky. 2008. “Dynamic Analysis and in Situ Validation of Perpetual Pavement Response to Vehicular Loading.” *Transportation Research Record: Journal of the Transportation Research Board*, 2087 (1): 29–39. https://doi.org/10.3141/2087-04.

Alrajhi, A., H. Ozer, and I. L. Al-Qadi. 2022. “Impact of rest period on asphalt concrete permanent deformation.” *Construction and Building Materials*, 332: 127329. https://doi.org/10.1016/j.conbuildmat.2022.127329.

Angah, O., and A. Y. Chen. 2020. “Tracking multiple construction workers through deep learning and the gradient based method with re-matching based on multi-object tracking accuracy.” *Automation in Construction*, 119: 103308. https://doi.org/10.1016/j.autcon.2020.103308.

Battaglia, P. W., J. B. Hamrick, V. Bapst, A. Sanchez-Gonzalez, V. Zambaldi, M. Malinowski, A. Tacchetti, D. Raposo, A. Santoro, R. Faulkner, C. Gulcehre, F. Song, A. Ballard, J. Gilmer, G. Dahl, A. Vaswani, K. Allen, C. Nash, V. Langston, C. Dyer, N. Heess, D. Wierstra, P. Kohli, M. Botvinick, O. Vinyals, Y. Li, and R. Pascanu. 2018. “Relational inductive biases, deep learning, and graph networks.” arXiv.

Benedetto, H. D., B. Delaporte, and C. Sauzéat. 2007. “Three-Dimensional Linear Behavior of Bituminous Materials: Experiments and Modeling.” *Int. J. Geomech.*, 7 (2): 149–157. https://doi.org/10.1061/(ASCE)1532-3641(2007)7:2(149).

Cao, W., and Y. R. Kim. 2016. “A viscoplastic model for the confined permanent deformation of

asphalt concrete in compression." *Mechanics of Materials*, 92: 235–247. https://doi.org/10.1016/j.mechmat.2015.10.001.

Chen, L., Y. Wang, and M.-F. F. Siu. 2020. "Detecting semantic regions of construction site images by transfer learning and saliency computation." *Automation in Construction*, 114: 103185. https://doi.org/10.1016/j.autcon.2020.103185.

Collop, A. C., A. (Tom) Scarpas, C. Kasbergen, and A. De Bondt. 2003. "Development and Finite Element Implementation of Stress-Dependent Elastoviscoplastic Constitutive Model with Damage for Asphalt." *Transportation Research Record*, 1832 (1): 96–104. https://doi.org/10.3141/1832-12.

Deacon, J. A., J. T. Harvey, I. Guada, L. Popescu, and C. L. Monismith. 2002. "Analytically Based Approach to Rutting Prediction." *Transportation Research Record*, 1806 (1): 9–18. https://doi.org/10.3141/1806-02.

Elseifi, M. A., I. L. Al-Qadi, and P. J. Yoo. 2006. "Viscoelastic Modeling and Field Validation of Flexible Pavements." *J. Eng. Mech.*, 132 (2): 172–178. https://doi.org/10.1061/(ASCE)0733-9399(2006)132:2(172).

Garcia, G., and M. R. Thompson. 2008. "Strain and Pulse Duration Considerations for Extended-Life Hot-Mix Asphalt Pavement Design." *Transportation Research Record*, 2087 (1): 3–11. https://doi.org/10.3141/2087-01.

Grzesikiewicz, W., A. Wakulicz, and A. Zbiciak. 2013. "Non-linear problems of fractional calculus in modeling of mechanical systems." *International Journal of Mechanical Sciences*, 70: 90–98. https://doi.org/10.1016/j.ijmecsci.2013.02.007.

Gungor, O. E., and I. L. Al-Qadi. 2022. "Wander 2D: a flexible pavement design framework for autonomous and connected trucks." *International Journal of Pavement Engineering*, 23 (1): 121–136. Taylor & Francis.

Hernandez, J. A., A. Gamez, and I. L. Al-Qadi. 2016. "Effect of Wide-Base Tires on Nationwide Flexible Pavement Systems: Numerical Modeling." *Transportation Research Record: Journal of the Transportation Research Board*, 2590 (1): 104–112. https://doi.org/10.3141/2590-12.

Hernandez, J. A., A. Gamez, I. L. Al-Qadi, and M. De Beer. 2014. "Analytical Approach for Predicting Three-Dimensional Tire–Pavement Contact Load." *Transportation Research Record: Journal of the Transportation Research Board*, 2456 (1): 75–84. https://doi.org/10.3141/2456-08.

Huang, Y. H. 2004. *Pavement analysis and design*. Upper Saddle River, NJ: Pearson/Prentice Hall.

Khan, A. S., O. Lopez-Pamies, and R. Kazmi. 2006. "Thermo-mechanical large deformation response and constitutive modeling of viscoelastic polymers over a wide range of strain rates and temperatures." *International Journal of Plasticity*, 22 (4): 581–601. https://doi.org/10.1016/j.ijplas.2005.08.001.

Kucuk, Y., C. Mollamahmutoglu, Y. Wang, and H. Lu. 2013. "Nonlinearly Viscoelastic Nanoindentation of PMMA Under a Spherical Tip." *Exp Mech*, 53 (5): 731–742. https://doi.org/10.1007/s11340-012-9695-0.

Li, G., M. Müller, A. Thabet, and B. Ghanem. 2019. “DeepGCNs: Can GCNs Go as Deep as CNNs?” arXiv.

Li, G., C. Xiong, A. Thabet, and B. Ghanem. 2020. “DeeperGCN: All You Need to Train Deeper GCNs.” arXiv.

Li, M., and Z. Zhu. 2021. “Spatial-Temporal Fusion Graph Neural Networks for Traffic Flow Forecasting.” *Proceedings of the AAAI Conference on Artificial Intelligence*, 35 (5): 4189–4196. https://doi.org/10.1609/aaai.v35i5.16542.

Liang, Y., and P. Guan. 2022. “Improved Maxwell model with structural dashpot for characterization of ultraslow creep in concrete.” *Construction and Building Materials*, 329: 127181. https://doi.org/10.1016/j.conbuildmat.2022.127181.

Liu, F., W. Ding, Y. Qiao, and L. Wang. 2020. “An artificial neural network model on tensile behavior of hybrid steel-PVA fiber reinforced concrete containing fly ash and slag power.” *Front. Struct. Civ. Eng.*, 14 (6): 1299–1315. https://doi.org/10.1007/s11709-020-0712-6.

Liu, F., W. Ding, Y. Qiao, and L. Wang. 2024a. “Transfer learning-based encoder-decoder model with visual explanations for infrastructure crack segmentation: New open database and comprehensive evaluation.” *Underground Space*, 17: 60–81. https://doi.org/10.1016/j.undsp.2023.09.012.

Liu, F., J. Li, and L. Wang. 2023. “PI-LSTM: Physics-informed long short-term memory network for structural response modeling.” *Engineering Structures*, 292: 116500. https://doi.org/10.1016/j.engstruct.2023.116500.

Liu, F., J. Liu, and L. Wang. 2022a. “Deep learning and infrared thermography for asphalt pavement crack severity classification.” *Automation in Construction*, 140: 104383. https://doi.org/10.1016/j.autcon.2022.104383.

Liu, F., J. Liu, L. Wang, and I. L. Al-Qadi. 2024b. “Multiple-type distress detection in asphalt concrete pavement using infrared thermography and deep learning.” *Automation in Construction*, 161: 105355. https://doi.org/10.1016/j.autcon.2024.105355.

Liu, F., K. Xu, W. Ding, Y. Qiao, and L. Wang. 2021. “Microstructural characteristics and their impact on mechanical properties of steel-PVA fiber reinforced concrete.” *Cement and Concrete Composites*, 123: 104196. https://doi.org/10.1016/j.cemconcomp.2021.104196.

Liu, J., F. Liu, C. Zheng, D. Zhou, and L. Wang. 2022b. “Optimizing asphalt mix design through predicting the rut depth of asphalt pavement using machine learning.” *Construction and Building Materials*, 356: 129211. https://doi.org/10.1016/j.conbuildmat.2022.129211.

Lundberg, J., S. Janhäll, M. Gustafsson, and S. Erlingsson. 2021. “Calibration of the Swedish studded tyre abrasion wear prediction model with implication for the NORTRIP road dust emission model.” *International Journal of Pavement Engineering*, 22 (4): 432–446. https://doi.org/10.1080/10298436.2019.1614585.

Majidifard, H., Y. Adu-Gyamfi, and W. G. Buttlar. 2020. “Deep machine learning approach to develop a new asphalt pavement condition index.” *Construction and Building Materials*, 247: 118513. https://doi.org/10.1016/j.conbuildmat.2020.118513.

Mallick, R. B., and T. El-Korchi. 2022. *Pavement Engineering: Principles and Practice*. Boca Raton: CRC Press.

Mitchell, T. M. 1997. “Machine learning.”

Okte, E., and I. L. Al-Qadi. 2022a. “Impact of Autonomous and Human-Driven Trucks on Flexible Pavement Design.” *Transportation Research Record*, 2676 (7): 144–160. SAGE Publications Inc. https://doi.org/10.1177/03611981221077083.

Okte, E., and I. L. Al-Qadi. 2022b. “Prediction of flexible pavement 3-D finite element responses using Bayesian neural networks.” *International Journal of Pavement Engineering*, 23 (14): 5066–5076. Taylor & Francis. https://doi.org/10.1080/10298436.2021.1993219.

Olard, F., and H. Di Benedetto. 2003. “General 2S2P1D Model and Relation Between the Linear Viscoelastic Behaviours of Bituminous Binders and Mixes.” *Road Materials and Pavement Design*, 4: 185–224. https://doi.org/10.1080/14680629.2003.9689946.

Park, S. W., and Y. R. Kim. 1999. “Interconversion between Relaxation Modulus and Creep Compliance for Viscoelastic Solids.” *J. Mater. Civ. Eng.*, 11 (1): 76–82. https://doi.org/10.1061/(ASCE)0899-1561(1999)11:1(76).

Park, S. W., and R. A. Schapery. 1999. “Methods of interconversion between linear viscoelastic material functions. Part I—a numerical method based on Prony series.” *International Journal of Solids and Structures*, 36 (11): 1653–1675. https://doi.org/10.1016/S0020-7683(98)00055-9.

Pei, J., Z. Fan, H. Liu, J. Zhang, R. Li, and Y. Li. 2016. “Nonlinear viscoelastic model for asphalt mixture subjected to repeated loading.” *Road Materials and Pavement Design*, 17 (4): 892–905. https://doi.org/10.1080/14680629.2015.1137781.

Pfaff, T., M. Fortunato, A. Sanchez-Gonzalez, and P. W. Battaglia. 2021. “Learning Mesh-Based Simulation with Graph Networks.” arXiv.

Ramakrishnan, A., A. Alrajhi, E. Okte, H. Ozer, I. L. Al-Qadi, Illinois Center for Transportation, and Center for Connected and Automated Transportation (CCAT). 2021. *Truck-Platooning Impacts on Flexible Pavements: Experimental and Mechanistic Approaches*.

Rivera-Pérez, J., and I. L. Al-Qadi. 2024. “Asphalt Concrete Mix Design Optimization Using Autoencoder Deep Neural Networks.” *Transportation Research Record*, 2678 (1): 426–438. SAGE Publications Inc. https://doi.org/10.1177/03611981231171153.

Romanoschi, S. A., and J. B. Metcalf. 2001. “Characterization of Asphalt Concrete Layer Interfaces.” *Transportation Research Record: Journal of the Transportation Research Board*, 1778 (1): 132–139. https://doi.org/10.3141/1778-16.

Sanchez-Gonzalez, A., J. Godwin, T. Pfaff, R. Ying, J. Leskovec, and P. W. Battaglia. 2020. “Learning to Simulate Complex Physics with Graph Networks.” arXiv.

Sanchez-Lengeling, B., E. Reif, A. Pearce, and A. B. Wiltschko. 2021. “A Gentle Introduction to Graph Neural Networks.” *Distill*, 6 (9): e33. https://doi.org/10.23915/distill.00033.

Soussou, J. E., F. Moavenzadeh, and M. H. Gradowczyk. 1970. “Application of Prony Series to Linear Viscoelasticity.” *Transactions of the Society of Rheology*, 14 (4): 573–584.

https://doi.org/10.1122/1.549179.

Subramanian, V., M. N. Guddati, and Y. Richard Kim. 2013. “A viscoplastic model for rate-dependent hardening for asphalt concrete in compression.” *Mechanics of Materials*, 59: 142–159. https://doi.org/10.1016/j.mechmat.2012.10.003.

Taghipour Anvari, A., S. Babanajad, and A. H. Gandomi. 2023. “Data-Driven Prediction Models For Total Shear Strength of Reinforced Concrete Beams With Fiber Reinforced Polymers Using An Evolutionary Machine Learning Approach.” *Engineering Structures*, 276: 115292. https://doi.org/10.1016/j.engstruct.2022.115292.

Wang, D., J. R. Roesler, and D.-Z. Guo. 2009. “Analytical Approach to Predicting Temperature Fields in Multilayered Pavement Systems.” *J. Eng. Mech.*, 135 (4): 334–344. https://doi.org/10.1061/(ASCE)0733-9399(2009)135:4(334).

Wang, H., and I. L. Al-Qadi. 2011. “Impact Quantification of Wide-Base Tire Loading on Secondary Road Flexible Pavements.” *J. Transp. Eng.*, 137 (9): 630–639. https://doi.org/10.1061/(ASCE)TE.1943-5436.0000245.

Wang, H., and I. L. Al-Qadi. 2013. “Importance of Nonlinear Anisotropic Modeling of Granular Base for Predicting Maximum Viscoelastic Pavement Responses under Moving Vehicular Loading.” *J. Eng. Mech.*, 139 (1): 29–38. https://doi.org/10.1061/(ASCE)EM.1943-7889.0000465.

Williams, M. L., R. F. Landel, and J. D. Ferry. 1955. “The Temperature Dependence of Relaxation Mechanisms in Amorphous Polymers and Other Glass-forming Liquids.” *J. Am. Chem. Soc.*, 77 (14): 3701–3707. https://doi.org/10.1021/ja01619a008.

Ye, Z., S.-C. Hsu, and H.-H. Wei. 2022. “Real-time prediction of structural fire responses: A finite element-based machine-learning approach.” *Automation in Construction*, 136: 104165. https://doi.org/10.1016/j.autcon.2022.104165.

Yoo, P. J., I. L. Al-Qadi, M. A. Elseifi, and I. Janajreh. 2006. “Flexible pavement responses to different loading amplitudes considering layer interface condition and lateral shear forces.” *International Journal of Pavement Engineering*, 7 (1): 73–86. https://doi.org/10.1080/10298430500516074.

Zbiciak, A. 2013. “Mathematical Description of Rheological Properties of Asphalt-Aggregate Mixes.” *Bulletin of the Polish Academy of Sciences: Technical Sciences*, 61 (1): 65–72. https://doi.org/10.2478/bpasts-2013-0005.

Zhai, G., Y. Xu, and B. F. Spencer. 2024. “Bidirectional graphics-based digital twin framework for quantifying seismic damage of structures using deep learning networks.” *Structural Health Monitoring*, 14759217241231299. SAGE Publications. https://doi.org/10.1177/14759217241231299.

Zhang, J., Z. Fan, K. Fang, J. Pei, and L. Xu. 2016. “Development and validation of nonlinear viscoelastic damage (NLVED) model for three-stage permanent deformation of asphalt concrete.” *Construction and Building Materials*, 102: 384–392. https://doi.org/10.1016/j.conbuildmat.2015.10.201.

Zhao, P., Y. Fei, Y. Huang, Y. Feng, W. Liao, and X. Lu. 2023a. “Design-condition-informed shear wall layout design based on graph neural networks.” *Advanced Engineering Informatics*, 58: 102190.

https://doi.org/10.1016/j.aei.2023.102190.

Zhao, P., W. Liao, Y. Huang, and X. Lu. 2023b. “Intelligent design of shear wall layout based on attention-enhanced generative adversarial network.” *Engineering Structures*, 274: 115170. https://doi.org/10.1016/j.engstruct.2022.115170.

Zhou, F., and T. Scullion. 2002. “Discussion: Three Stages of Permanent Deformation Curve and Rutting Model.” *International Journal of Pavement Engineering*, 3 (4): 251–260. https://doi.org/10.1080/1029843021000083676.

Zhou, F., T. Scullion, and L. Sun. 2004. “Verification and Modeling of Three-Stage Permanent Deformation Behavior of Asphalt Mixes.” *Journal of Transportation Engineering*, 130 (4): 486–494. American Society of Civil Engineers. https://doi.org/10.1061/(ASCE)0733-947X(2004)130:4(486).

Zhou, Q., and I. L. Al-Qadi. 2024. “Graph Neural Networks to Simulate Flexible Pavement Responses Using Three-Dimensional Finite Element Analysis Data.” *Transportation Research Record: Journal of the Transportation Research Board*, 03611981241242783. https://doi.org/10.1177/03611981241242783.

Zhou, Q., F. Zhu, X. Yang, F. Wang, B. Chi, and Z. Zhang. 2017. “Shear capacity estimation of fully grouted reinforced concrete masonry walls using neural network and adaptive neuro-fuzzy inference system models.” *Construction and Building Materials*, 153: 937–947. https://doi.org/10.1016/j.conbuildmat.2017.07.171.

Zhu, M., H. Zhu, F. Guo, X. Chen, and J. W. Ju. 2021. “Tunnel condition assessment via cloud model-based random forests and self-training approach.” *Computer-Aided Civil and Infrastructure Engineering*, 36 (2): 164–179. https://doi.org/10.1111/mice.12601.